HU ISSN 1586–2070

JOURNAL OF COMPUTATIONAL AND APPLIED MECHANICS

A Publication of the University of Miskolc

VOLUME 8, NUMBER 1 (2007)

MISKOLC UNIVERSITY PRESS

HU ISSN 1586–2070

JOURNAL OF COMPUTATIONAL AND APPLIED MECHANICS

A Publication of the University of Miskolc

VOLUME 8, NUMBER 1 (2007)

MISKOLC UNIVERSITY PRESS

EDITORIAL BOARD

LOCAL EDITORIAL COUNCIL

T. CZIBERE, I. KOZÁK, I. PÁCZELT, G. PATKÓ, G. SZEIDL

Journal of Computational and Applied Mechanics, Vol. 8., No. 1., (2007), pp. 3–4

PREFACE

Special Issue
Selected papers from
the Conference on Modelling Fluid Flow (CMFF'06)

In this special issue of JCAM we have the pleasure to feature articles based upon papers presented at the Conference on Modeling Fluid Flow (CMFF'06), held at Budapest University of Technology and Economics in September 2006. This conference was the 13th event in the International Conference Series on Fluid Flow Technologies held in Budapest, and attracted authors from more than 40 nations.

From among the 139 conference presentations, several regarded as being of particular interest to a wider audience were selected, and their authors were invited to extend the topic of their presentations into expanded articles for journal publication. We are therefore able to offer our readers a taste of the variety of CMFF'06, in the form of articles by authors from a number of nations dealing with various aspects of flow.

For the conference itself, papers were divided into two workshop sessions and nine parallel sessions. In this special issue we bring you papers representing a majority of the sessions: External Fluid Dynamics, Turbomachinery, Internal Flows, Flow and Acoustics, Multiple Phase Flows and Components, Turbulence Modeling and Numerical Methods, and the workshop session on the Modelling of Turbomachinery Aerodynamics. The authors represented in this volume are carrying out their research in universities across Europe, and we are pleased to present papers from Far-East Asian researchers as well.

The articles in this volume cover topics ranging from low Reynolds number flow around a cylinder to subsonic flow around an aircraft, and from computation of the acoustic field in a combustion chamber to an analysis of spray evolution in internal combustion engines. Flow is studied in turbomachines - a centrifugal fan, axial-flow fan, cross-flow fan, an axial compressor - in nozzles, and in channels, around cylinders - circular, square, orbiting, oscillating, installed in a cruciform arrangement - and even around an athlete's body. Studies feature both commercial and in-house codes, and include both two-dimensional and three-dimensional simulations.

In this issue readers can find many computational studies: Abboudi et al., Didier and Borges, Hős and Kullmann, Jia et al., Kadocsa et al., Karabelos and Markatos, Lewis, Punčochářová et al., Szász et al., and Younsi et al. Several of these compare their computational results with previously published measurements. Corsini and

Sheard present both computational and experimental results in his article, as do Klemm et al., while Koide et al. and Oggiano et al. present experimental studies.

With such a variety of topics and studies represented, we are sure that every reader will find something of interest in this issue, which is being published as Volume 8, Numbers 1 and 2.

Miskolc, 15 November 2007

László Baranyi
Editor of the special issue
János Vad
Guest editor

Journal of Computational and Applied Mechanics, Vol. 8., No. 1., (2007), pp. 5–19

THERMAL WALL INFLUENCE ON THE BEHAVIOR OF AXISYMMETRIC LAMINAR COMPRESSIBLE FLOW IN NOZZLE

Said Abboudi, Jing Deng, Michel Imbert
FEMTO-ST, UMR 6174 CNRS, Dpt CREST
UFC-UTBM, Site de Sévenans, 90010, Belfort Cedex, France
said.abboudi@utbm.fr

[Received: January 12, 2007]

Abstract. The present work concerns a numerical study of an axisymmetric laminar flow of a compressible gas in a small size convergent-divergent nozzle. The geometry and the reservoir conditions are like that they make important dissipative effects. The numerical study is performed with Mac-Cormack explicit scheme and the splitting of the operator in the two spatial directions is adopted. Comparisons between different thermal wall conditions (adiabatic, cooling, and heating) are realized and show the influence of these conditions on the structure of the flow, in particular in predominant viscous effects region.

Mathematical Subject Classification: 76M25
Keywords: Compressible, Mac-Cormack scheme, nozzle, numerical study, viscous flow, wall thermal conditions

1. Introduction

Although the most obvious applications of compressible gas flow are in aerospace, the knowledge of the effects of compressibility in a flow is absolutely necessary for many others engineering applications: gas turbines, combustion chambers for examples.

Compressible gas flows at moderate Reynolds number in channels of constant or variable cross section are also frequently met in several branches of contemporary technicals as for examples: micro-channels, chemical reactive flow and gasodynamic lasers [1-5], shock waves interactions [6,7] , spray process [8,9], production of micro metallic particles [10,11], conception and design of micro valveless pumps, micro joining, micro combustion and vaporizing water micro-thruster [12-15].

The calculation of viscous nozzle flows can be accomplished by either solving the inviscid core and viscous boundary layer equations separately or by solving the complete Navier-Stokes equations for the entire flow field. In this study, the very small size convergent-divergent nozzle and the reservoir conditions lead to a Reynolds number on the order of 103 based on the throat radius. In these conditions the thickness of

the boundary layer cannot be regarded as thin when compared to the nozzle diameter and the splitting of the flow in two parts is a questionable assumption.

The conservative form of the complete Navier-Stokes equations for axisymmetric, compressible, viscous time dependent flow of a perfect gas is solved. The numerical study is performed with Mac-Cormack explicit finite difference scheme and the splitting of the two-dimensional operator in two one-dimensional operators is adopted [6] and [16-25].

Other investigations based on the finite volume method are proposed in [26-27] and a new formulation using characteristic wave relations through boundaries is derived for the Euler equations and generalized to the Naviers-Stokes equations [**??**].

The obtained numerical results are shown in figures for the cases (a) of an adiabatic wall, (b) of cooling of the wall, and (c) of heating of the wall. Comparisons between these different wall thermal conditions are realized and show their influence on the structure of the flow, in particular in the region where the viscous effects are predominant.

2. **Governing equations**

2.1. **Formulation of the problem.** The governing equations for a compressible, viscous fluid in the absence of body forces consist of the unsteady Navier-Stokes equations. In the cylindrical coordinates (r, θ, x), these equations for axisymmetric flows can be written in conservative form as follows:

$$\frac{\partial \tilde{U}}{\partial t} + \frac{\partial \tilde{F}}{\partial x} + \frac{\partial \tilde{G}}{\partial r} + \frac{1}{r}\tilde{H} = 0 \tag{2.1}$$

where $\tilde{U}$, $\tilde{F}$, $\tilde{G}$, $\tilde{H}$ are 4-component vectors defined as :

$$\tilde{U} = \left[\rho,\ \rho u,\ \rho v,\ \rho E\right]^t, \tag{2.2}$$

$$\tilde{F} = \left[\rho u, \rho u^2 + P - \tau_{xx}, \rho uv - \tau_{xr}, (\rho E + P)\, u - u\tau_{xx} - v\tau_{xr} - q_x\right]^t, \tag{2.3}$$

$$\tilde{G} = \left[\rho v, \rho uv - \tau_{xr}, \rho v^2 + P - \tau_{rr}, (\rho E + P)\, v - u\tau_{xr} - v\tau_{rr} - q_r\right]^t, \tag{2.4}$$

$$\tilde{H} = \left[\rho v, \rho uv - \tau_{xr}, \rho v^2 - (\tau_{rr} - \tau_{\theta\theta}), (\rho E + P)\, v - u\tau_{xr} - v\tau_{rr} - q_r\right]^t. \tag{2.5}$$

The stress and heat transfer components are given as:

$$\tau_{xx} = (\lambda + 2\mu)\frac{\partial u}{\partial x} + \lambda \frac{1}{r}\frac{\partial}{\partial r}(rv), \tag{2.6}$$

$$\tau_{rr} = (\lambda + 2\mu)\frac{\partial v}{\partial r} + \lambda\left(\frac{\partial u}{\partial r} + \frac{v}{r}\right), \tag{2.7}$$

$$\tau_{xr} = \mu\left(\frac{\partial u}{\partial r} + \frac{\partial v}{\partial x}\right), \tag{2.8}$$

$$\tau_{\theta\theta} = (\lambda + 2\mu)\frac{v}{r} + \lambda\left(\frac{\partial u}{\partial x} + \frac{\partial v}{\partial r}\right), \tag{2.9}$$

$$q_x = k\frac{\partial T}{\partial x},\ q_r = k\frac{\partial T}{\partial r}. \tag{2.10}$$

The total energy is given as:

$$E = e + \frac{1}{2}\left(u^2 + v^2\right). \tag{2.11}$$

The state equation of perfect gas is used to close the system (2.12):

$$P = \rho \Re T. \tag{2.12}$$

The coefficient of viscosity is assumed to vary according to the temperature and the second coefficient of viscosity is assumed to follow Stokes' hypothesis: $3\lambda + 2\mu = 0$.

As it is usual in nozzle flow calculations, the physical domain $D(x, r)$ is transformed into a rectangular one by means of the transformation T:

$$D(x, r) \longrightarrow D(\xi, \eta),$$

with:

$$\xi(x) = \frac{x}{r_p^*} \text{ and } \eta(x, r) = 1 - \frac{r}{r_p(x)},$$

where r_p^* and $r_p(x)$ are respectively the radius of the throat and the wall.

This transformation applied to equation (2.12) leads to the following weakly conservative form:

$$\frac{\partial U}{\partial t} + \frac{\partial F}{\partial \xi} + \frac{\partial G}{\partial \eta} + \frac{1}{r}H = 0, \tag{2.13}$$

with:

$$U = \frac{\tilde{U}}{J},\ F = \frac{\tilde{F}}{J}\frac{\partial \xi}{\partial x}, \tag{2.14}$$

$$G = \frac{1}{J}\left(\tilde{F}\frac{\partial \eta}{\partial x} + \tilde{G}\frac{\partial \eta}{\partial r}\right),\ H = \frac{\tilde{H}}{J}, \tag{2.15}$$

where $J = \frac{\partial(\xi,\eta)}{\partial(x,r)}$ is the Jacobian of the transformation T.

2.2. **Computational domain.** The domain of integration is limited by the wall at $\eta = 0$, the nozzle axis at $\eta = 1$ and the two boundaries, upstream $\xi = 0$ and $\xi = \xi_{\max}$ downstream normal to the axis. The line ($\eta = 0$) gives the position of the wall, while the symmetry axis of the nozzle is situated midway between the two last lines of the grid. In the longitudinal direction ξ, the step is chosen constant. In the transverse direction η, in order to take into account the viscous effects, the step is taken to be variable from the wall to η_f, and then it is constant up to the nozzle axis.

2.3. **Boundary conditions.** The values on the symmetry axis ($\eta = 1$) are taken to be $\partial\varphi/\partial\eta = 0$ for $\varphi = u, T, P$, and $v = 0$.

At the exit of the nozzle, the boundary conditions values of the flow are obtained by a linear extrapolation.

At the wall ($\eta = 0$) the no-slip condition gives $u = v = 0$.

The pressure P is obtained from the second momentum equation.

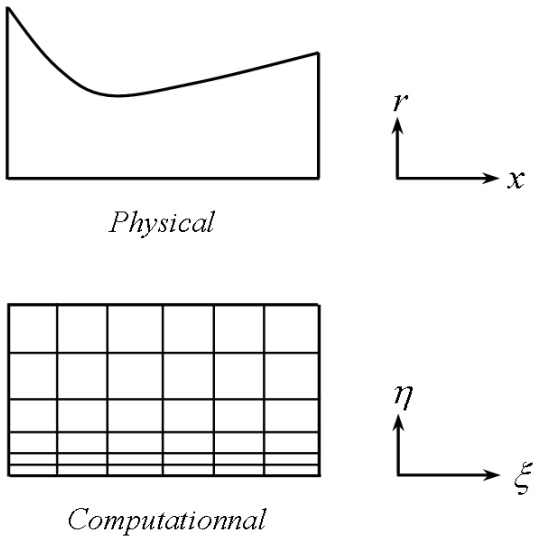

Figure 1. Definition of the integration domain

The wall of the nozzle is submitted to an adiabatic or variable temperature conditions. At the inlet boundary, the value of the velocity is obtained by an extrapolation from the adjacent interior grid points. The temperature is deduced by using the conservation of the total enthalpy between the reservoir and the inlet grid boundary.

An isentropic evolution between the reservoir and the inlet is adopted to obtain the pressure.

3. **Numerical method**

The Navier-Stokes equations system is solved by an explicit predictor-corrector scheme as given by Mac-Cormack [6]. The accuracy of this numerical method is second order in space and time. The solution at the time $(n+1)\,\Delta t$ is calculated from knowledge of the solution at $n\Delta t$ by:

$$U_{i,j}^{n+1} = L\,(\Delta t)\,U_{i,j}^{n}. \tag{3.1}$$

The two dimensional operator $L\,(\Delta t)$ is split into two one-dimensional operators $L_\xi\,(\Delta t_\xi)$ and $L_\eta\,(\Delta t_\eta)$ according to the sequence which favors the transverse effects and preserves the second order accuracy of the numerical scheme:

$$U_{i,j}^{n+1} = L_\eta\,(\Delta t_\eta)\,L_\xi\,(\Delta t_\xi)\,L_\eta\,(\Delta t_\eta)\,U_{i,j}^{n}. \tag{3.2}$$

The operators L_ξ and L_η are respectively applied to the following one-dimensional system of equations:

$$\frac{\partial U}{\partial t} + \frac{\partial F}{\partial \xi} = 0, \tag{3.3}$$

$$\frac{\partial U}{\partial t} + \frac{\partial G}{\partial \eta} + \frac{H}{r} = 0. \tag{3.4}$$

L_ξ being defined as predictor under the form:

$$\bar{U}^{**}_{i,,j} = U^{*}_{i,,j} - \frac{\Delta t_\xi}{\Delta \xi}\left(F^{*}_{i+1} - F^{*}_{i,j}\right), \tag{3.5}$$

and as corrector:

$$\bar{U}^{**}_{i,,j} = \frac{1}{2}\left[U^{*}_{i,,j} + \bar{U}^{**}_{i,,j} - \frac{\Delta t_\xi}{\Delta \xi}\left(\bar{F}^{**}_{i,1} - \bar{F}^{**}_{i-1,,j}\right)\right]. \tag{3.6}$$

L_η is defined as predictor:

$$\bar{U}^{**}_{i,,j} = U^{*}_{i,,j} - \frac{\Delta t_\eta}{\Delta \eta}\left(G^{*}_{i,j+1} - G^{*}_{i,j}\right) - \Delta t_\eta H^{*}_{i,j}, \tag{3.7}$$

and as corrector:

$$\bar{U}^{**}_{i,,j} = \left[\frac{1}{2}U^{*}_{i,,j} + \bar{U}^{**}_{i,,j} - \frac{\Delta t_\eta}{\Delta \xi}\left(\bar{G}^{**}_{i,j} - \bar{G}^{**}_{i,,j-1}\right) - \Delta t_\eta \bar{H}^{**}_{i,j}\right]. \tag{3.8}$$

Notice that the spatial derivates of F and G are discretized with opposite one-sided finite differences in the predictor and corrector stages.

The difference equations are stable if:

$$\Delta t_\eta \text{ and } \Delta t_\xi \leq \frac{\Delta \eta \Delta \xi}{\left(-\lambda\mu\right)^{1/2}/\rho}. \tag{3.9}$$

For the difference equations applied to the full set of Naviers-Stokes equations, the estimated stability criteria are:

$$\Delta t_\xi \leq \frac{\Delta \xi}{|u| + c + \frac{1}{\rho}\left[\frac{2\gamma\mu}{\mathrm{Pr}\,\Delta\xi} + \frac{(-\lambda\mu)^{1/2}}{\Delta\eta}\right]}, \tag{3.10}$$

$$\Delta t_\eta \leq \frac{\Delta \eta}{|v| + c + \frac{1}{\rho}\left[\frac{2\gamma\mu}{\mathrm{Pr}\,\Delta\eta} + \frac{(-\lambda\mu)^{1/2}}{\Delta\xi}\right]}, \tag{3.11}$$

where Pr is the Prandlt number, $\lambda = \frac{2}{3}\mu$ and is calculated by Sutherland's formula.

The details of this numerical scheme are given in the reference [6].

4. **Numerical results and discussion**

The numerical results are obtained in the following conditions:

The half angle of the conical convergent is 45°.

The half angle of the conical divergent is 10°.

The convergent and the divergent are connected by an arc of circle.

The radius of the throat is $R_{\mathrm{col}} = 0.03cm$.

The reservoir conditions are: $P_0 = 1.2 \cdot 10^5\ Pa$ and $T_0 = 1500\ K$.

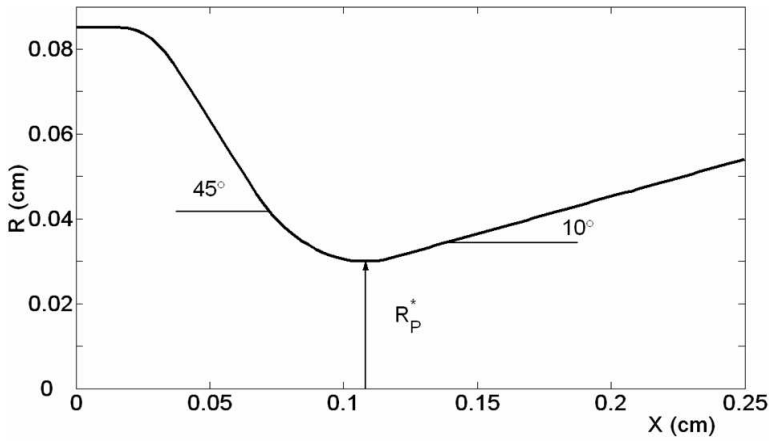

Figure 2. Geometry of the nozzle

The results are presented for three different wall thermal conditions:

Case a: Insulated (or adiabatic) wall.

Case b: Variable temperature profile, cooling wall $T_w(x) = Ax^2 + Bx + C$ for $0 < x < 0.25$, with $A = 7.2 \cdot 10^{-3}$, $B = -0.12$, and $C = 1$. The minimum of $T_w(x)$ is equal to $0.5T_0$ at $x = 0.25\ cm$.

Case c: Variable temperature profile, heating wall $T_w(x) = Ax^2 + Bx + C$ for $0 < x < 0.25$, with $A = -7.2 \cdot 10^{-3}$, $B = 0.12$, and $C = 1$. The maximum of $T_w(x)$ is equal to $1.5T_0$ at $x = 0.25\ cm$.

In the computational field, we have used 90 grid points in the ξ direction and 32 grid points in the η direction. The time step is chosen according to the stability criterion of the numerical scheme described above.

Under these conditions, the isotherm curves in the physical plane are presented in the figures 3 a, b, c for the three studied cases.

The figure 3a shows that the dissipative effects are significant on about a third of the exit radius. With regard to the cases (b) and (c), the cooling of the wall involves a decrease of the thickness of the thermal boundary layer and an increase in the heating case. In this last case, this thickness reaches 40% of the exit radius, figure 3 c and figure 4 for $x = 0.25\ cm$.

In the inviscid core of the flow, the effects of the parietal thermal conditions are obviously less important but nevertheless visible as it can be seen on figure 4 for $x = 0.18\ cm$ and $x = 0.25\ cm$.

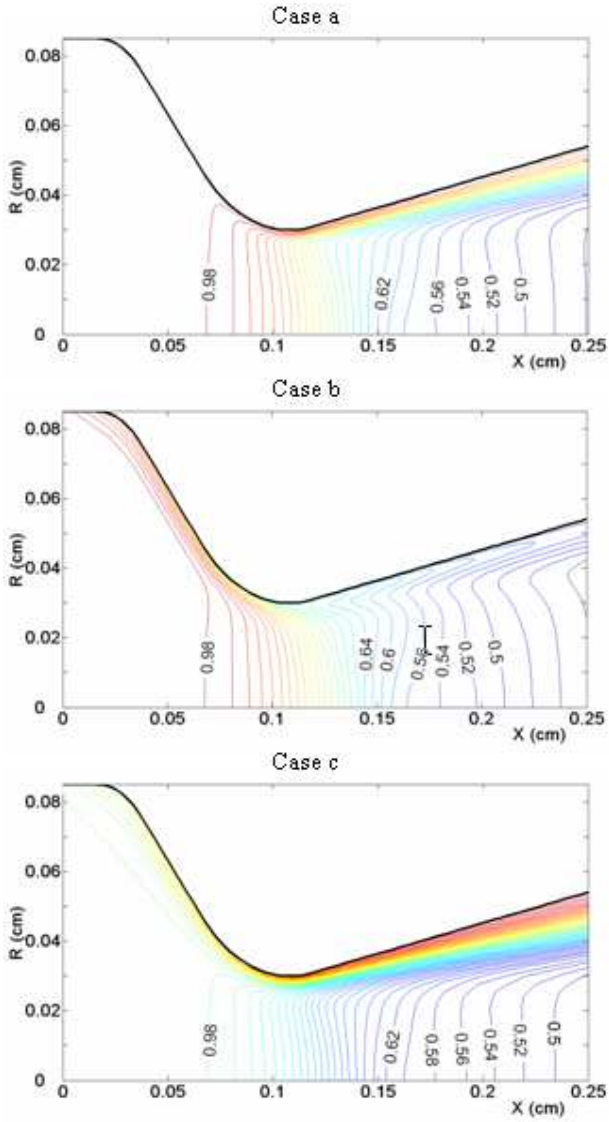

Figure 3. a, b, c. Contours of constant dimensionless temperature in the physical plane ($\Delta T = 0.02$) for the three cases

In the supersonic expansion, the dynamic effects play a prominent role compared to the parietal heating effects. The thicknesses of the dynamic boundary layer are almost of the same order for the three cases, figures 5, 6 and 7.

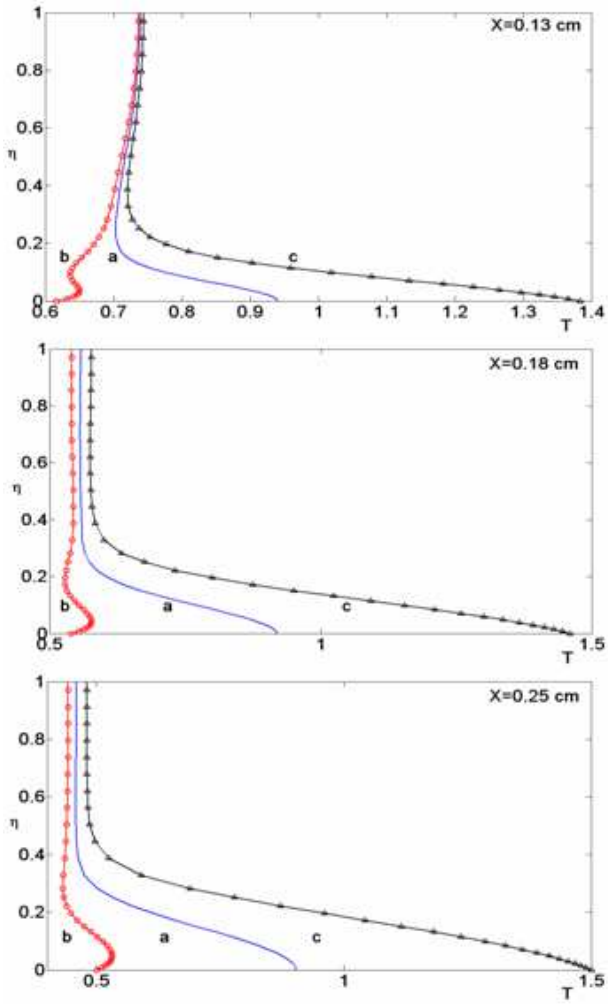

Figure 4. Non-dimensional temperature profiles in different cross sections for the three cases

However, a certain number of expected results are found. In the divergent of the nozzle, the supersonic velocities, for the adiabatic case, are lower than that corresponding to the cooling case and higher than that corresponding to the heating case, figures 5, for $x = 0.18\ cm$ and $x = 0.25\ cm$.

These results can also be seen on the Mach profiles, figures 6 a, b c where the values of the exit mach numbers are respectively $M = 2.5$ for the case (b), $M = 2.4$ for the case (a) and $M = 2.3$ for the case (c). The velocity profiles, figures 7 plotted at the same axial position show the same dynamic behavior.

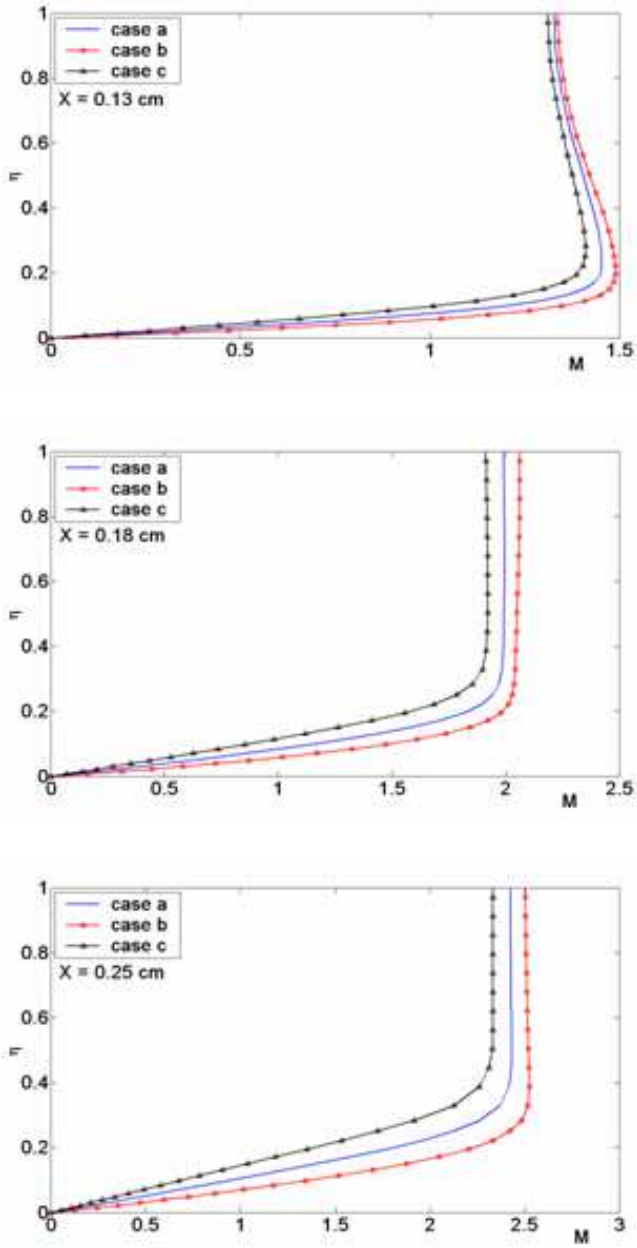

Figure 5. Non-dimensional Mach profiles in different cross section for the three cases

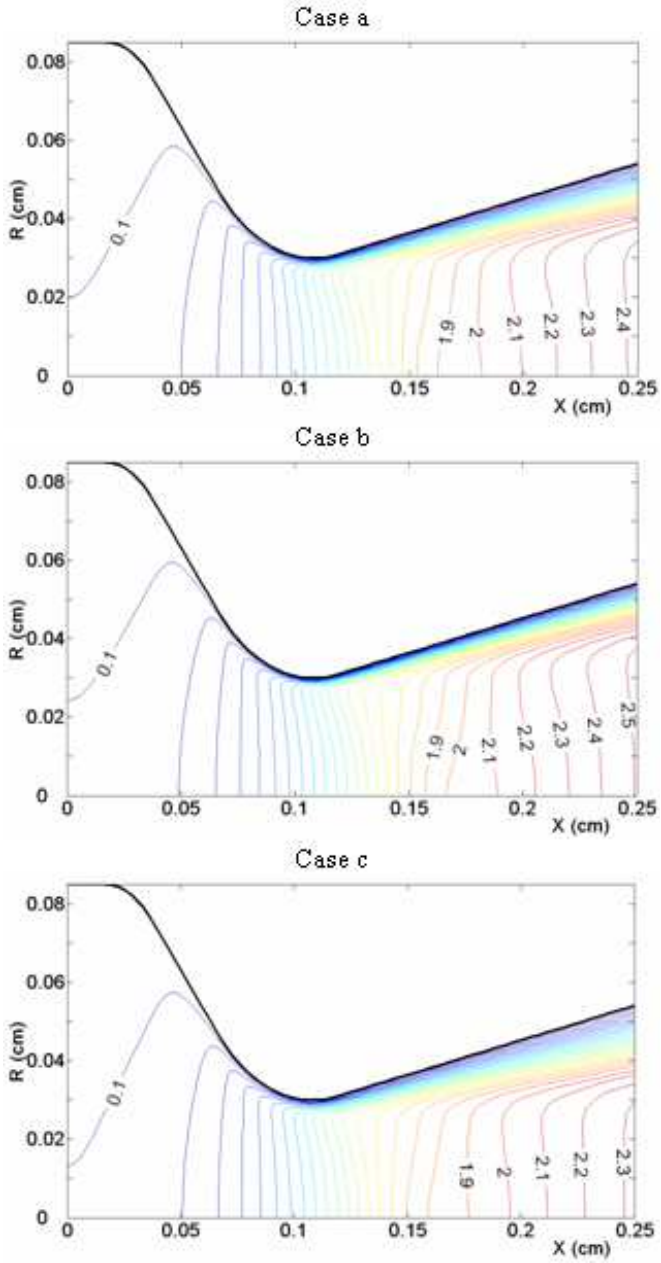

Figure 6. a, b, c. Isomachs in the physical plane ($\Delta M = 0.05$)

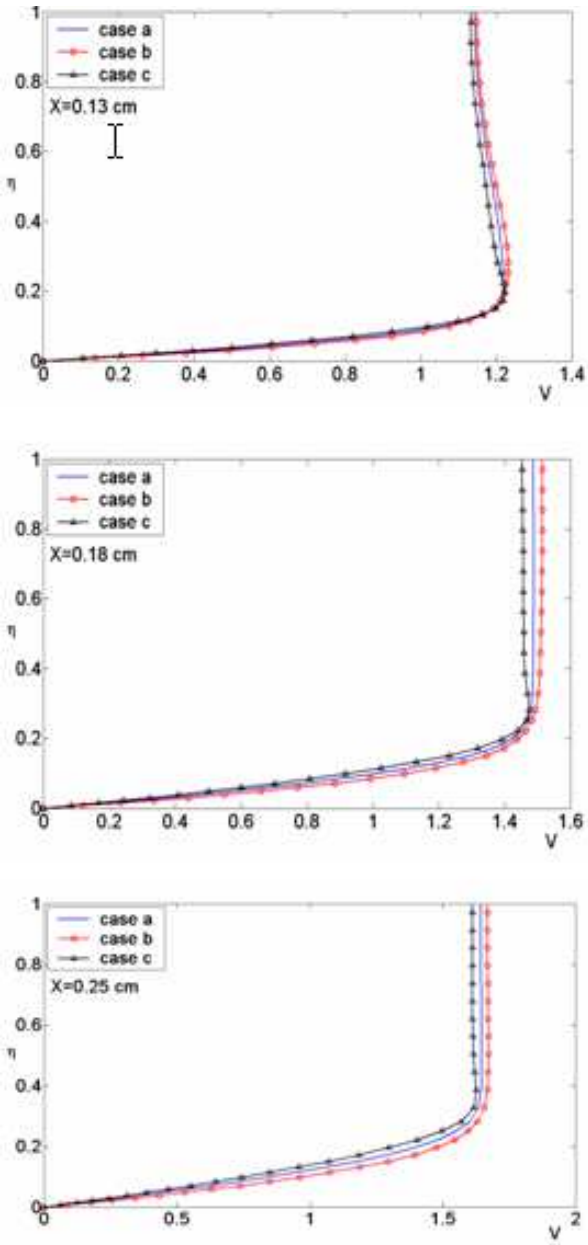

Figure 7. Non-dimensional velocity profiles in different cross section for the three cases

The same remarks can be made on the isobar curves, plotted in the physical plane, figures 8 a, b and c. The strongest expansion of the gas flow corresponds to the

cooling case and the weakest expansion corresponds to the heating case, figures 8 a, b, and c and figures 9 a, b and c for $x = 0.13\ cm$, $x = 0.18\ cm$ and $x = 0.25\ cm$.

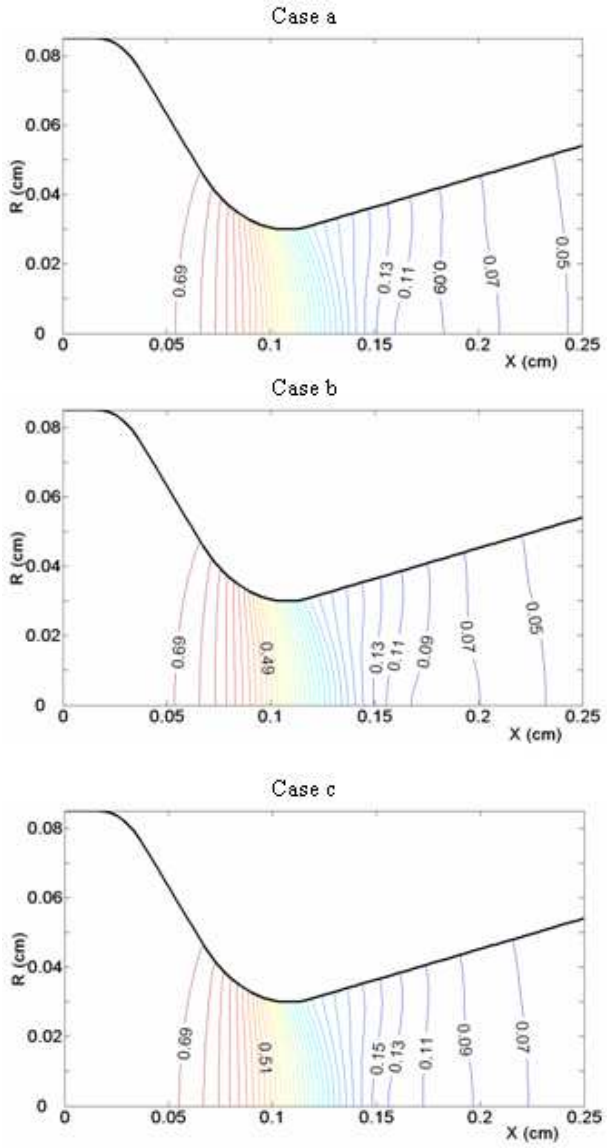

Figure 8. a, b, c. Contours of constant dimensionless pressure in the physical plane ($\Delta P = 0.02$) for the three cases

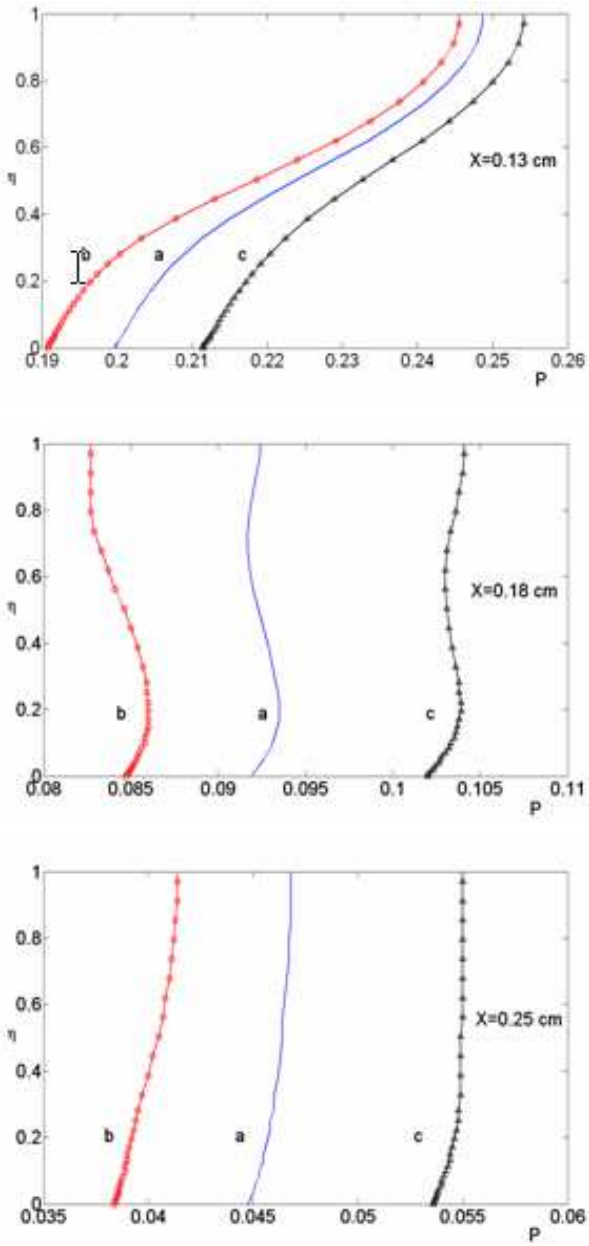

Figure 9. Non-dimensional pressure profiles in different cross sections for the three cases

5. Conclusion

Solutions for an axisymmetric nozzle flow were obtained numerically using the full Naviers-Stokes equations. The numerical study was performed with Mac Cormack finite difference scheme splitting of the operator in the two spatial directions. Three wall thermal conditions were analyzed (adiabatic, cooling and heating). The profile and contours of constant dimensionless temperature, Mach number and pressure are presented for the three cases. The results show that the dissipative effects are more significant for the heating case while of course, the expansion in the supersonic divergent is more important in the cooling case.

References

1. Meister, L., Burtschell, Y. and Zeitoum, D.E.: Numerical study of a reactive flow in an over-expanded nozzle: Influences of wall temperature and altitude. *Mécanique & Industries*, **4**, (2003), 339-346.
2. Vlad, G., Boiron, O., Le Place, G. and Bournot, P.: Numerical study of the compressible turbulent flow in a laser cavity. *Int. J. Heat Mass Transfer*, **38**, (1995), 2623-2633.
3. Jackson, M.J., Robinson, G.M., Gill, M.D.H. and O'Neill, W.: The effect of nozzle design on laser micro-machining of M2 tool steels. *Journal of Materials Processing Technology*, **160**(2), (2005), 198-212.
4. Tsunoda, K., Suzuki, T., and Asai, T.: Improvement of the performance of a supersonic nozzle by riblets. *Journal of Fluids Engineering*, **122**(3), (2000), 585-591.
5. Louisos, W.F. and Hitt, D.L.: Optimal Expansion Angle for Viscous Supersonic Flow in 2-D Micro-Nozzles, 35th AIAA Fluid Dynamics Conference and Exhibit, Toronto, Ontario, (2005), June 6-9.
6. Mac Cormack, R.W. and Baldwin, B.S.: A Numerical method for solving the Navier-Stokes equations with application to shock-boundary layer interactions, AIAA 13th Aerospace Sciences Meeting, Pasadena, Calif, (1975), January 20-22.
7. Xu, J. and Zhao, C.: Two-dimensional numerical simulations of shock waves in micro convergent-divergent nozzles. *Journal of Heat and Mass Transfer*, **50**(11-12), (2007), 2434-2438.
8. Park, J., Chung, S., Yun, H., Cho, K., Chung, C., Han, D-C. and Chang, J.K.: Asymmetric nozzle structure for particles converging into a highly confined region. *Current Applied Physics*, **6**, (2006), 992-995.
9. Jen, T-C., Li, L., Cui, W., Chen, Q. and Zhang, X.: Numerical investigations on cold gas dynamic spray process with nano- and microsize particles. *International Journal of Heat and Mass Transfer*, **48**, (2005) 4384-4396.
10. Lin, S-L. and Lin, J.: Flow characteristics and micro-scale metallic particle formation in the laser supersonic heating technique. *Optics & Laser Technology*, **39**, (2007), 53-60.
11. Lin, S-L. and Lin, J.: Characteristics of laser supersonic heating method for producing micro metallic particles. *Optics & Laser Technology*, **37**, (2005), 563-569.

12. Ziang, X.N., Zhoub, Z.Y., Huang, X.Y., Li, Y., Yang, Y. and Liu, C.Y.: Micronozzle / diffuser flow and its application in micro valveless pumps. *Sensors and Actuators*, A 70, (1998), 81-87.

13. Andrijasevic, D., Giouroudi, I., Smetana, W., Boehm, S., Zehetner, J. and Brenner, W.: New approach to micro-joining by hot gas stream. *Microelectronic Engineering*, **83**, (2006), 1445-1448.

14. Pan, J.F., Huang, J., Li, D.T., Yang, W.M., Tang, W.X. and Xue, H.: Effects of major parameters on micro-combustion for thermophotovoltaic energy conversion. *Applied Thermal Engineering*, **27**, (2007), 1089-1095.

15. Ye, X., Tang, F., Ding, H. and Zhou, Z.: A vaporizing water micro-thruster, Micro Electro Mechanical Systems, 2000. MEMS 2000. The Thirteenth Annual International Conference, Volume, Issue , 23-27 Jan 2000,74-79.

16. Cebeci, T. and Bradshaw, P.: Physical and Computational Aspects of Convective Heat Transfer (Springer-Verlag, New York, (1984).

17. Schlicting, H.: Boundary Layer Theory (McGraw Hill, New York, (1960) 177-184.

18. Peyret, R. and Taylor, T.D.: Computational Methods for Fluid Flow (Springer-Verlag. Berlin, (1982).

19. Anderson, D.A., Tannehill, J.C. and Pletcher, R.H.: Computational Fluid Mechanics and Heat Transfer, In Proceedings of 14th Australian Fluid Mechanics Hemisphere Publishing, Corporation, (1984).

20. Imbert, M. and Zeitoun, D.: Etude numérique d'un écoulement à nombre de Reynolds modéré dans une tuyère. *Journal de Mécanique Théorique et Appliquée*, 1(4), (1982), 595–609.

21. Steger, J.L. and Warming, R.F.: Flux vector splitting of the inviscid gasdynamic equations with application to finite-difference methods. *Journal of Computational Physics*, **40**, (1981), 263–293.

22. Yang, Y.M.: Modélisation mathématique d'un système de projection thermique à la flamme de type H.V.O.F.: application à l'élaboration de revêtements protecteurs, Thesis, Institut Polytechnique de Sévenans, (1986).

23. Perrin, A. and Hu, H.H.: An explicit finite-difference scheme for simulation of moving particles. *Journal of Computational Physics*, **212**, (2006), 166 -187.

24. Jorgenson, P.C.E. and Pletcher, R.H.: An implicit numerical scheme for the simulation of internal viscous flow on unstructured grids. *Journal of computers & Fluids*, **25**, (1996), 447-466.

25. Bijl, A.P.H and Wesseling, P.: A unified method for computing incompressible and compressible flows in boundary-fitted coordinates. *Journal of Computational Physics*, **141**, (1998), 153-173.

26. Anderson, W.K., Thomas, J.L. and Van Leer, B.: Comparison of finite volume vector splittings for the Euler eqautions. *AIAA Journal*, **24**, (1986), 1453-1460.

27. Poinsot, T.L. and Lele, S.K.: Boundary conditions for direct simulations of compressible viscous flows. *Journal of Computational Physics*, **101**, (1992), 104-129.

Journal of Computational and Applied Mechanics, Vol. 8., No. 1., (2007), pp. 21–37

TIP END-PLATE CONCEPT BASED ON LEAKAGE VORTEX ROTATION NUMBER CONTROL
[Leakage vortex rotation number based tip end-plate]

Alessandro Corsini
Department of Mechanics and Aeronautics, Sapienza University of Rome
Via Eudossiana, 18, I00184, Italy
corsini@dma.ing.uniroma1.it

Anthony G. Sheard
Fan Technology, Flakt Woods Ltd
Axial Way, Colchester, Essex, C04 5ZD, UK
geoff.sheard@flaktwoods.com
[Received: January 8, 2007]

Abstract. This paper reports on quantitative tests of passive techniques for rotor-tip noise control in ventilating fans using modifications to the blade-tip end-plate as anti-vortex appendages. A variable thickness in the end-plate appendage is shown to control the chord-wise evolution of leakage-vortex rotation number. The results show that the new end-plate design configuration provides passive control of vortex breakdown, and thus represents a mechanism whereby leakage-vortex bursting can be avoided.

Keywords: rotor noise passive control, tip end-plates, leakage vortex breakdown, rotation number stability criterion

1. Introduction

Blade-tip aerodynamics are driven by non-linear interactions among: (i) tip-leakage flow; (ii) skewed end-wall boundary layers; and (iii) blade-passage secondary flows. The complexity of blade-tip aerodynamics determines the rotor operating margin in tip-stalling rotors because the aerodynamics establish the blade span-wise loading and loss distributions, as well as the turbomachine's aero-acoustic signature [1-3]. As observed by Ganz et al [4], the physical mechanisms that determine the tip-region flow around blades in turbomachinery compressors also apply in industrial ventilating and cooling fans. The diminished performance associated with these flow mechanisms has prompted designers of fans and compressors alike to devise new design features that minimise the adverse aerodynamic effects of tip gap. In doing so, their objective is to manage the tip-clearance flow in a manner that reduces the self-generated noise without sacrificing aerodynamic efficiency. The objective of reducing noise without sacrificing aerodynamic performance can be accomplished either by reducing the leakage flow rate or by enhancing the primary–secondary flow momentum transfer.

For industrial fans and turbomachinery compressors, research efforts in pursuit of this objective can be categorised into two approaches. The use of casing treatments in the shroud portion over the blade tip was first reported in the early 1970s. This provided an improved stable flow range by weakening the tip-leakage vortex (TLV). Notable contributions have reported the use of grooves and slots [5, 6] and stepped tip gaps [7]. More specifically, in terms of fan technology, recirculating vanes and annular rings have been proposed as anti-stall devices [8]; indeed, these are now routine in commercial operations.

A second approach consists of passive control techniques. Various passive approaches based on blade-tip anti-vortex appendages have been proposed—such as those investigated by Quinlan and Bent [9] and those provided by several industrial patents for ventilating fans [8, 10-12].

Recently, Corsini et al. [13-15] investigated the application of profiled end-plates to the blade tips of a family of commercially available industrial fans. They reported benefits in terms of aerodynamic and aeroacoustic performance as a result of the adoption of modified blade-tip configurations. In particular, the adoption of a constant-thickness end-plate (designated AC90/6/TF) that had originally been designed at Fläkt Woods Ltd for an industrial fan provided effective control of leakage-flow phenomena over the fan operating range. However, in spite of the aeroacoustic gains, aerodynamic tests on AC90/6/TF revealed a diminution in performance in association with the occurrence of leakage vortex bursting over the tip end-plate. This breakdown was characterised by the abrupt expansion of the swirling core into a bubble-like circulatory zone.

The aim of the present paper is to present an anti-vortex tip end-plate of variable thickness. It is contended that the variable thickness of this new configuration controls the chord-wise evolution of the leakage-vortex rotation number. As such, the new end-plate configuration promises to provide a passive control mechanism whereby leakage-vortex bursting can be avoided.

Vortex breakdown is an intriguing phenomenon of practical importance. It occurs in swirling flows and, depending on the application, can be a positive or negative occurrence. Control of the phenomenon has been of interest to scholars for two decades, and continues to be an active area of research—especially in the field of aeronautical applications (for example, delaying delta wing vortices or accelerating trailing tip vortices [16]), and in combustors, valves, and cyclones [17]. In the present study, the modified configuration aims to influence the onset of vortex breakdown by the use of a variable chordwise end-plate thickness distribution. The aim is to enhance near-axis swirl [18, 19] by influencing the momentum transfer from the leakage flow and inducing some waviness into the leakage vortex trajectory, as suggested by Srigrarom and Kurosaka [20] in delta-wing platform design.

The remainder of this paper is organised as follows. In the next section, the family of test fans is described and the background quantitative experimental investigations are summarised. In the following section, leakage flow in the tip region of the AC90/6/TF fan is surveyed to provide evidence of the presence of vortex breakdown.

In the fourth section, the rationale for the proposed end-plate of variable thickness is described. The final section of the paper presents a comparative assessment of the end-plate aerodynamics of the datum fan, the constant-thickness AC90/6/TF fan, and the proposed end-plate of variable thickness (designated 'AC90/6/TFvte'). The overall objective is to investigate the technical merits of a passive control strategy for controlling leakage flow, with a view to ascertaining its potential for reducing tip-clearance interaction noise and rotor-tip noise.

2. Test fans and background studies

2.1. **2.1 Test fans.** The present study was undertaken using a family of commercially available industrial cooling fans. In-service experience had indicated that this family of fans provides state-of-the-art acoustic performance. The fan studied here featured a six-blade unswept rotor, with the blade profiles being a modified ARA-D configuration originally designed for propeller applications. The details of the blade profile for the AC90/6 fan are shown in Table 1. The design configurations for both the datum

Table 1. Blade profile geometry

	*AC*90/6 fan blade		
	hub	midspan	tip
ℓ/t	1.32	0.5	0.31
pitch angle (*deg*)	36	31.2	28
camber angle (*deg*)	46	44	41

and modified rotors are shown in Table 2. They featured a large tip-stagger angle of 28 degrees, which was measured (as is customary in industrial fan practice) from the peripheral direction. This rotor angular setting was chosen to exploit operating points at which the vortex flow near the rotor tip has its most significant effects on the aerodynamic performance and noise characteristics of the investigated fans.

Table 2. *AC*90/6 fan family specifications

Design specifications	
blade number	6
blade tip stagger angle (*deg*)	62
hub-to-casing diameter ratio v	0.22
D_h (*mm*)	200.0
D_c (*mm*)	907
rotor tip clearance χ (% *span*)	1.0
rotational frequency (*rpm*)	$900 \div 935$

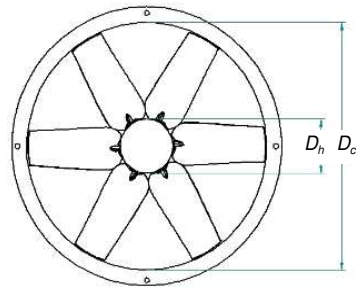

Figure 1 illustrates the configurations for: (i) the datum rotor (AC90/6); and (ii) a modified rotor (designated 'AC90/6/TF'), which was designed with a view to reducing noise emission. The modified AC90/6/TF rotor blades differed from the datum blades in the vicinity of the tip. The configuration of the AC90/6/TF blade tip, which was

Figure 1. Rotors blade details: a) *datum* fan, and b) improved AC90/6/TF.

originally inspired by designs developed for tip-vortex control and drag reduction in aircraft wings and catamaran hulls, differed from the datum fan by the addition of an end-plate. This end-plate ran along the blade pressure surface and ended on the blade trailing edge with a square tail. The addition of the end-plate meant that the blade section was locally thickened by a factor of three with respect to the maximum thickness at the tip of the datum blade. This dimension was chosen on the basis of previous studies of rotors of axial compressors [21] and fans [22], in which end-plate dimensions were determined in proportion to the radial dimension of the leakage vortex to be controlled—estimated in this case to be 0.1–0.2 blade spans.

2.2. **Background studies.** Recent studies by Corsini et al. [13–15] have assessed the performance of the modified end-plate configuration of the AC90/6/TF rotor. These studies demonstrated that the modified end-plate configuration effectively controlled leakage-flow phenomena over the fan operating range. In doing so, the modified end-plate improved the three-dimensional (3-D) loss behaviour, moved the peak efficiency plateau towards the lower flow rate, and markedly reduced the fan's aero-acoustic signature.

Table 3. Measured fans overall aerodynamic and acoustic performance

	Datum rotor		*AC*/90/6/*TF* rotor	
Aerodynamic	Δp_{stat} (Pa)	η	Δp_{stat} (Pa)	η
D point	134.8	0.49	126.2	0.51
P point	184.4	0.44	179.4	0.49
Acoustic	un-weighted SWL dB	A-weighted SWL $dB(A)$	un-weighted SWL dB	A-weighted SWL $dB(A)$
D point	72.38	70.85	70.17	66.92
P point	72.72	71.85	69.66	67.44

Table 3 shows the overall aerodynamic and acoustic performance for two operating points: (i) near-design condition (designated 'D point') with volume flow rate 7 m^3/s;

and (ii) a near-peak pressure condition (designated 'P point') with a volume flow rate of 6 m^3/s. In addition, Table 3 shows the overall noise performance in terms of the un-weighted and A-weighted sound-power levels (SWLs) at a distance of 6 m from the fan outlet.

3. **Leakage vortex breakdown detection**

3.1. **Evidence of the vortex breakdown.** One of the main findings reported by Corsini et al. [13] was that the leakage-flow control provided by the aerodynamic appendages at the blade tip of AC90/6/TF gave rise, under near-design operating conditions, to a bursting of the tip-leakage vortex. To provide greater insight into this phenomenon, the 3-D streamline behaviour in the tip gap of rotor AC90/6/TF was visualised (see Figure 2) under D operating conditions with a volume flow rate 7 m^3/s and a global flow coefficient ($\Phi\mathfrak{pg}$) of 0.278. The anti-vortex effect produced by

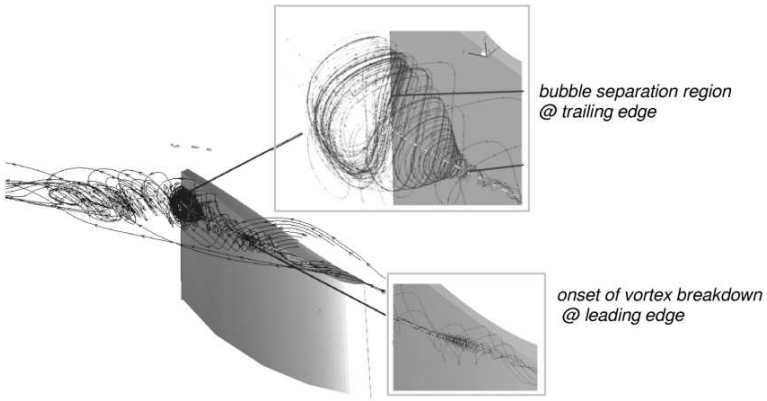

Figure 2. Streamlines in the rotor tip gap @ *D* operating point, and vortex bursting visualization

the end-plate acted as a physical obstacle to the pressure surface-flow migration and preserved the pressure-side tip vortex, thus promoting a *vena contracta* effect. As a consequence, the reduced leakage flow (visualised as 3-D streamlines) altered the swirl-to-axial vortex velocity component ratio, which gave rise to an unseparated bubble core about mid-chord, followed by of a large bubble-type separation in the aft portion of the blade passage. This finding was in accordance with the existence of a vortex breakdown (because the flow reversal is indicative of the critical bursting phenomenon [23]). Moreover, according to Liebovich [24], the appearance of the vortex bursting in the bubble form can be interpreted as a consequence of a sufficiently large swirl level. As observed by Escudier and Zehnder [25] and Inoue and Furukawa [26], the stability of the bubble form of the vortex increases with the level of swirl, which supports the proposition that the bubble-separation core is evidence of the occurrence of tip-leakage vortex breakdown. The mid-chord bubble-core can therefore be considered as evidence of the onset of the bursting of the rear vortex.

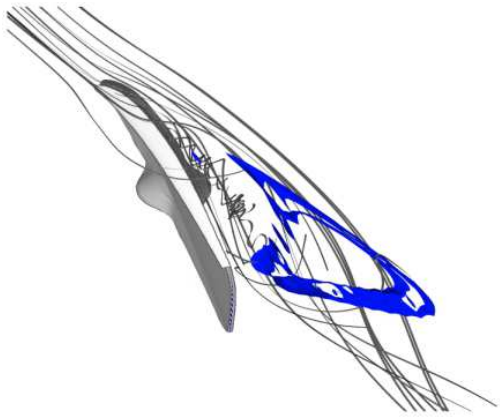

Figure 3. Streamlines and vortex axial velocity isosurface ($w_{aTLV} = 0$) in the rotor tip gap @ D operation

To assess the veracity of the above conjecture, tip-leakage vortex axial velocity zero iso-surfaces were drawn, as shown in Figure 3, together with 3-D streamlines in the blade-tip region. A zero w_{aTLV} core was located in coincidence with the unseparated bubble-core (see Figure 2), which was identified as the onset of the vortex breakdown. This finding was in accordance with the observation of Spall et al. [16], who first identified the presence of a stagnation point along the vortex axis as an essential precondition for the breakdown to appear. A second and larger zero-velocity iso-surface is also shown, which limits the bursting core featuring the flow reversal.

As a last criterion for the detection of vortex breakdown, the tip-leakage vortex structures were investigated using a normalised helicity (H_n) based on the absolute vorticity [2, 26] as a detection tool. H_n was defined and normalised as: $H_n = (\xi_i \cdot w_i) / (|\xi|\,|w|)$ with $i = 1 \ldots 3$, where ξ_i and w_i are the Cartesian components of the absolute vorticity and relative velocity vectors, $|\xi|$ and$|w|$ their norms. The normalised helicity (H_n) contours on cross-section for the datum and AC90/6/TF rotors are shown in Figure 4. The probing planes were located at 0.25 blade chords, 0.43 blade chords, 0.65 blade chords, 0.89 blade chords, and 1.2 blade chords from the tip-section leading edge. The normalised helicity distribution was then plotted with the vortex cores (coloured in accordance with the H_n local magnitude).

As shown in Figure 4, the AC90/6/TF rotor (Figure 4a) demonstrated a modified tip-leakage phenomenon compared with the datum rotor (Figure 4b). In particular, at about mid-chord, the main tip-leakage vortex featured a gradual reduction in H_n as a result of the weakening of the flow vortex and the deflection of the vortex core. This finding is in accordance with the hypothesis of mass leaking reduction along the chord, which gives rise to leakage-flow structures adjacent to the blade's suction surface. In the aft portion of the blade, the leakage flow insufficiently feed the main tip-leakage vortex (TLV) that collapses and evolves into a counter-clockwise vortex under the influence of trailing-edge leakage-flow streams, which rapidly washed out

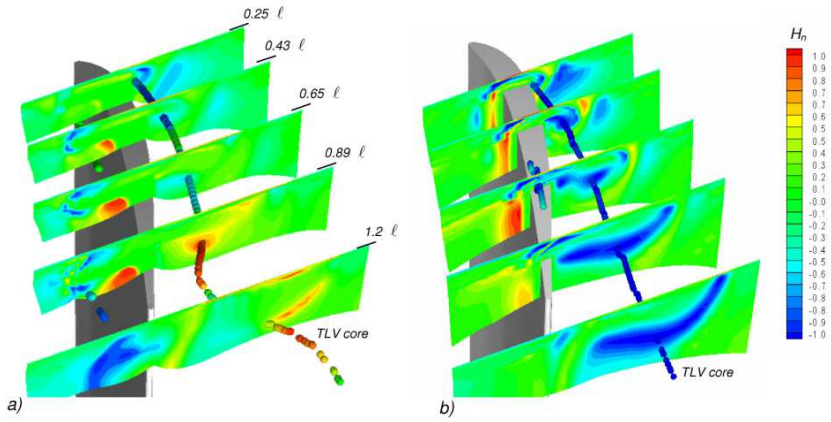

Figure 4. Normalized helicity H_n contours on cross sections and vortex cores at the tip, *D*operating point: a) AC90/6/TF rotor, b) AC90/6 *datum* rotor.

the vortex behind the rotor. Correspondingly, on the 1.2 ℓ plane, no coherent vortex structure was apparent.

These findings can be taken as additional evidence in support of the proposition that vortex breakdown occurred. The most distinctive feature was found in the helicity inversion, which occurred as a result of the counter-rotation of the vortex exiting from the bursting region. This phenomenon, which is accepted as evidence of vortex breakdown in compressor rotors [26], is consistent with the criterion based on the angle between the velocity and vortex vectors. Several studies have attempted to explain vortex breakdown on the basis of the behaviour of the azimuthal vortex component; in particular, Leibovich [27] has stated that a change in sign of the azimuthal vorticity is definitive evidence of the existence of vortex breakdown.

3.2. **Vortex breakdown Rossby number analysis.** Almost all of the studies on vortex breakdown, including those that have analysed linear stability and phase velocity [28] and those that have adopted a wave-trapping mechanism [29], have attempted to identify a critical condition for the appearance of vortex bursting using swirl-based parameters. Leibovich [24] explained a vortex breakdown as a change in the structure of the vortex initiated by a variation in the ratio between tangential velocity components and axial velocity components.

In a similar vein, Ito et al. [30], who undertook a theoretical study of unsteady and steady vortex breakdown, proposed a novel interpretive criterion based on the use of the Rossby number (or inverse swirl parameter), defined as:

$$Ro = V/\left(r\Omega\right) \tag{3.1}$$

with: V, r and Ω represent characteristic velocity, length and rotation rate scales.

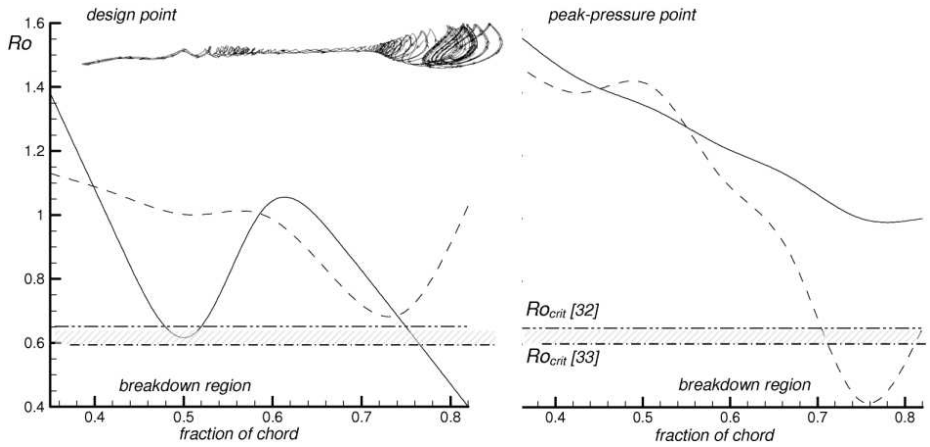

Figure 5. Chordwise distributions of tip leakage vortex rotation number *Ro* a) design and b) peak pressure operating points (dashed line: *datum* fan; solid line: $AC90/6/TF$ fan)

The breakdown criterion based on the Rossby number was completed by Spall et al. [16], who proposed scale definitions for the velocity distribution consistent with swirling flows, leading-edge vortices, and unconfined trailing wing-tip vortices. These definitions were adopted in the present study in the context of a confined tip-leakage vortex, which is typical of axial decelerating turbomachinery. In the present study: r, was taken to be the radial distance from the vortex axis at which the swirl velocity was at a maximum (corresponding to the characteristic viscous length scale, as suggested by Leibovich [31]); $V = w_{aTLV}$, was taken to be the axial velocity at r; and Ω, was taken to be the rotation rate in the wing-tip vortices due to the solid body rotation-like structure (estimated near the vortex centre).

The choice of w_{aTLV} as a velocity scale was consistent with the swirl scale ($\Omega\mathfrak{g} = w_{pTLV}$) and the critical Ro number values mentioned in the relevant literature. This ranged from 0.64 for a confined axi-symmetric vortex breakdown (Uchida et al. [32]) to 0.6 for wing-tip vortices with bubble- or spiral-type vortex breakdown (Garg and Leibovich [33]).

Figure 5 shows a comparison of the chord-wise distributions of the tip-leakage vortex Rossby numbers for the datum rotor and the AC90/6/TF rotor at the design point (Figure 5a) and at the peak-pressure point (Figure 5b). The Ro distributions under design conditions indicate that the AC90/6/TF fan featured a vortex breakdown and confirm that the unseparated bubble-core at mid-chord (as previously illustrated in Figure 2) corresponded to the attainment of the critical Rossby number value. This finding provides evidence for the validity of the Rossby breakdown concept in assessing the swirling flows of axial rotor turbomachinery.

The findings with respect to chord-wise Ro distributions also show that the trend in the Rossby number, approaching the critical value, was related to an incipient

breakdown. This is evident from the observation that Ro values below the critical threshold appeared for both the AC90/6/TF fan rotor (D point in Figure 5a) and the datum rotor (P point in Figure 5b). The Ro distributions also reveal that the approach to the breakdown is driven by a similar chord-wise decrease in the vortex rotation number. This suggests that control of the tip-leakage vortex Rossby number could be based on a near-axis swirl supply or subtraction, which could be implemented by a modification of the end-plate configuration with a view to establishing an original design concept for blade-tip aerodynamic appendages.

4. **Tip end-plate design concept**

To suppress the tip-leakage vortex-bursting phenomenon in the operation of the AC90/6/TF fan rotor, a new end-plate design concept has been recently proposed. The proposed configuration controls vortex breakdown by means of an end-plate of variable chord-wise thickness. The aim of the new concept is to enhance near-axis swirl [18, 19] by reconfiguring the end-plate at the tip with a view to influencing the momentum transfer from the leakage flow and to force some waviness into the leakage-vortex trajectory, as suggested by Srigrarom and Kurosaka [20] in delta-wing platform design. According to the analysis of tip-leakage vortices in terms of Rossby number behaviour (as shown in Figure 4), the shape of the end-plate is based on the definition of a safe rotation number chord-wise gradient.

The rationale of the present investigation was to compute the end-plate thickness distribution ($t_{ep}(s_c)$) by combining a simplified law for the tip-gap pressure drop with a stability criterion of TLV prescribed by a *safe* chord-wise distribution of the vortex Rossby number (as shown in Figure 5). The pressure losses within the tip gap at each chord-wise *abscissae* s_c was modelled by studying the leakage flow as a two-dimensional flow orthogonal to the chord line. The pressure drop could thus be expressed as a function of:

1. the geometry of the gap (height τ_{gap}, width t_{ep});
2. the kinetic energy of the leakage flow, as given by the leakage velocity component normal to the chord $(w_{Ln})^2$;
3. the friction factor f_f which is itself a function of leakage flow Reynolds number, $Re_{gap} = f(\tau_{gap}, w_{Ln})$ velocity scale;; and
4. the end-plate thickness $t_{ep}(s_c)$.

On the basis of the above, the pressure drop through the gap at each *abscissae* s_c is given by:

$$dp\,(s_c) = \rho \frac{f_f\,(Re_{gap})}{2\tau_{gap}} t_{ep}(s_c) w_{Ln}^2(s_c), \tag{4.1}$$

It is noteworthy that the friction factor f_f dependence on the chord-wise position s_c is fixed by means of the adoption of a scaling value for the leakage flow bulk velocity w_{Ln}. The derivation of equation (4.1) along the chord thus gives the directional

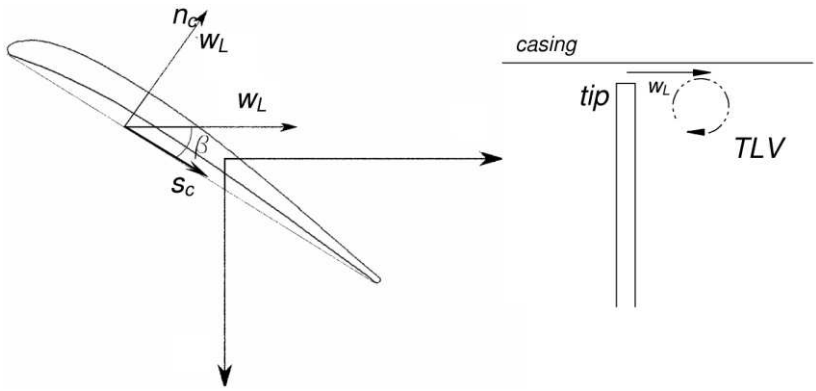

Figure 6. Coordinate system definition

gradient of the tip-gap pressure loss:

$$\frac{dp}{ds_c} = \rho \frac{f_f\left(Re_{gap}\right)}{2\tau_{gap}} \frac{d\left[t_{ep}(s_c) w_{Ln}^2(s_c)\right]}{ds_c}. \tag{4.2}$$

By re-arranging equation (4.2), it is possible to formulate a correlation between the end-plate geometry, parameterised by its thickness, and the aerodynamics of leakage flow in the form of an *ODE*, as follows:

$$\left[A_w \frac{dt_{ep}\left(s_c\right)}{ds_c} + A_{Ro} t_{ep}\left(s_c\right)\right] = B, \tag{4.3}$$

in which: B, accounts for the tip gap pressure drop; and A_w depends on the definition of a velocity scale for the leakage flow. The A_{Ro}coefficient is made proportional to the chord-wise gradient of the leakage-flow velocity normal to the chord w_{Ln}, as follows:

$$A_{Ro} \propto \frac{dw_{Ln}(s_c)}{ds_c}. \tag{4.4}$$

By means of the chord-wise gradient of $w_{Ln}(s_c)$ in equation (4.4), it is then possible to include in equation (4.3) an explicit dependence from the rotation number gradient. On the basis of the definition in equation (3.1), the Rossby number chord-wise gradient can be expressed as:

$$\frac{d_{Ro}}{ds_c} = \frac{d_{Ro}}{ds_c}|_{_{TLV\ stable}} = \frac{1}{r\Omega} \frac{dw_L(s_c)}{ds_c}\ . \tag{4.5}$$

The leakage-flow velocity $w_L(s_c)$ approximates the axial velocity of the leakage vortex w_{aTLV} at its periphery. By assuming a uniform direction of the leakage flow along the blade-tip chord, equation (4.4) can be rearranged in terms of the leakage-flow velocity normal to the chord $w_{Ln}(s_c)$, as follows:

$$\frac{1}{r\Omega} \frac{dw_L(s_c)}{ds_c} \cong \frac{1}{r\Omega} \frac{1}{sen\left(\beta_L\right)} \frac{dw_{Ln}(s_c)}{ds_c} \tag{4.6}$$

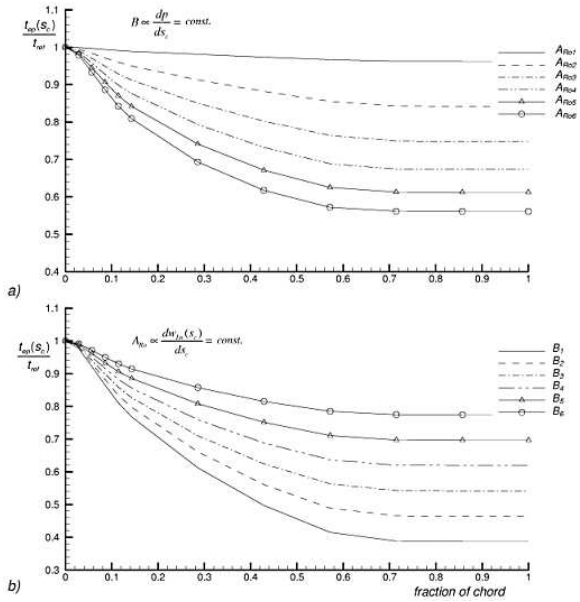

Figure 7. Parametric analysis of end-plate thickness design distributions, a) for increasing Rossby number gradient from A_{Ro1} to A_{Ro6}, and b) for increasing gap pressure drop gradient from B_1 to B_6

It is then possible to establish the end-plate thickness distribution according to any stable Rossby number gradient value as:

$$\frac{d_{Ro}}{ds_c}|_{TLV\ stable} = \frac{1}{r\Omega}\frac{dw_L(s_c)}{ds_c} \propto \frac{1}{r\Omega}\frac{1}{sen\,(\beta_L)}A_{Ro}. \tag{4.7}$$

A parametric analysis of the end-plate thickness distribution is presented in Figure 7. This was obtained by solving equation (4.3) by: (i)assuming a constant pressure-drop gradient and changing the rotation number gradient (Figure 7a); and (ii) assuming a constant A_{Ro} and varying the tip-gap pressure-drop gradient (Figure 7b). Figure 8 shows a qualitative view (not to scale) of the blade-tip of the new end-plate (designated 'AC90/6/Tfvte') compared with the datum fan and the constant-thickness end-plate (AC90/6/TF).

5. **Assessment of end-plate aerodynamics**

Experimental quantitative studies were conducted to assess the aerodynamic performance of the modified end-plate configuration (AC90/6/TFvte) compared with the datum fan and the AC90/6/TF fan. The studies were carried out in ducted configuration under near-design conditions. The Reynolds number, based on tip diameter and rotor tip speed, was $8.3\times\ 10^5$ (for ISO air conditions).

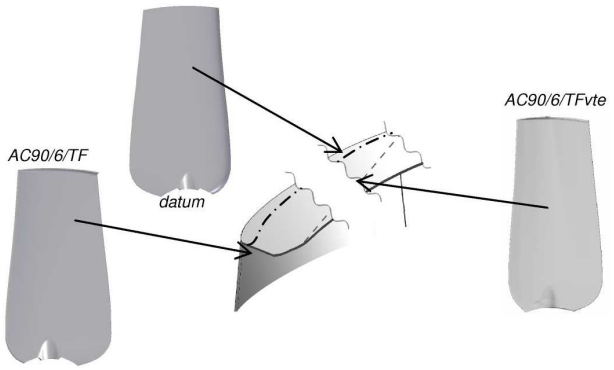

Figure 8. Test fans and end-plate geometries (not to scale)

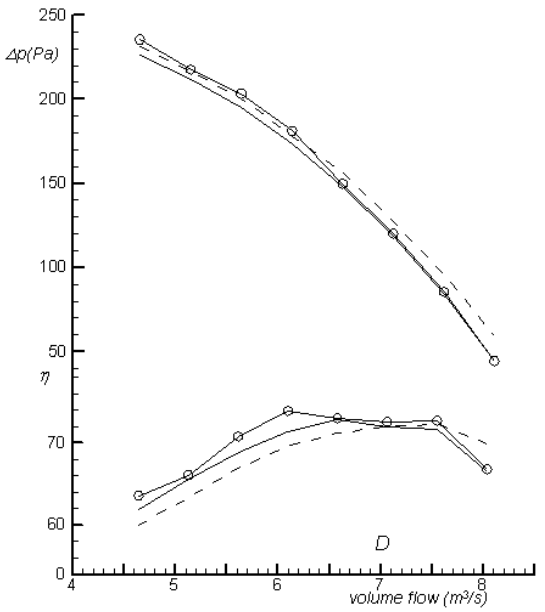

Figure 9. Measured static pressure and total pressure efficiency characteristic curves (dashed lines: *datum* fan; solid lines: $AC90/6/TF$ fan; line-symbols: $AC90/6/TFvte$ fan)

5.1. **Aerodynamic tests.** The main performance parameters used in this assessment were the fan static pressure and the efficiency. Measurements of static and dynamic pressure were carried out with four taps, equally spaced on the casing wall, and a standard Pitot-probe. The probe was mounted on a traverse mechanism fixed to the outer wall of the test rig. A Furness digital multi-channel micro-manometer (Model FC012, Furness Controls Ltd, UK) with 2 kPa range and a resolution of 1 Pa, was used to read pressure data. The accuracy of pressure measurements was $\pm$ 0.5% of read data. The efficiency was calculated as the ratio between the air power (computed on either static or dynamic pressure rise) and the electric power. The absorbed electric power was measured with an AC power analyser with an accuracy of 0.24% of read data.

The static pressure and efficiency characteristic curves for the datum rotor, the AC90/6/TF rotor, and the AC90/6/TFvte rotor are shown in Figure 9. As shown in the diagram, analysis of the static pressure curves revealed a small reduction in

Table 4. Predicted and measured fan overall performance @ 7 m^3/s

	Measurements		Predictions	
	Δp_{stat} (Pa)	η	Δp_{stat} (Pa)	η
datum	134.8	0.49	133.3	0.510
$AC90/6/TF$	126.2	0.51	126.1	0.504
$AC90/6/TFvte$	129.0	0.52	128.2	0.516

performance (about 2% at 6m^3/s) in the AC90/6/TF rotor as a result of the interaction between the tip-clearance flow and the suction-side near-surface fluid [35]. This diminution in performance was recovered (at least in part) by the AC90/6/TFvte rotor, in which the static pressure rise increased by throttling the rotor towards peak pressure.

A comparison of the efficiency curves revealed that both of the modified rotors (AC90/6/TF and AC90/6/TFvte) demonstrated an improvement in efficiency when the volume flow rate was greater than the design volume flow rate. Moreover, comparison of the efficiency curves indicates that the adoption of the modified tip end-plates resulted in the appearance of a clear efficiency plateau, which shifted the peak η volume flow rate towards the rotor stall margin.

The rotor performance was assessed along the operating line. Table 4 shows a comparison of the predicted overall performance (at 900-rpm rotational frequency) with the experimental data. Efficiency η was computed in terms of static pressure rise. The comparison confirmed the validity of the predicted performance at the chosen blade angle—the blade angle at which the fan blades are most heavily loaded (and thus more prone to flow separation). The parameters for prediction of performance referred to axial sections located at: (i) the inlet of the domain; and (ii) 20% midspan chords downstream of the blade's trailing edge. The comparison validated the predicted performance.

5.2. **Loss at the rotor tip.** Rotor loss behaviour at the blade tip was assessed under near-design conditions (D point) in terms of the local total loss coefficient ($\zeta\mathfrak{p}$,defined as: $\zeta = \overline{p}_{0in} - p_0 \big/ 0.5\rho\overline{w}_{in}^2$, in which: p_0 is the local total pressure, $\overline{p}_{0in}$ and $0.5\rho\overline{w}_{in}^2$ are respectively the reference pitch-averaged relative total and dynamic pressures computed at the inlet mid-span plane.

The total loss coefficient distribution within the blade passage was obtained by probing the flow fields in the vicinity of the blade leading edge at about mid-chord and in the region behind the blade (at approximately 25%, 65%, and 120% chords from the leading edge). The predicted loss evolutions, under design operating conditions, as shown in Figures 10a, 10b, and 10c, were in accordance with studies of low-speed rotors [36] and with the other aerodynamic tests carried out in the present study. At the rotor inlet, all rotor distributions demonstrated loss cores that were mainly concentrated on the hub annulus walls. Moving towards the aft portion of the blade, the loss maps were characterised by loss core directly related to the development of primary tip vortices travelling through the blade vane. As a result of vortex

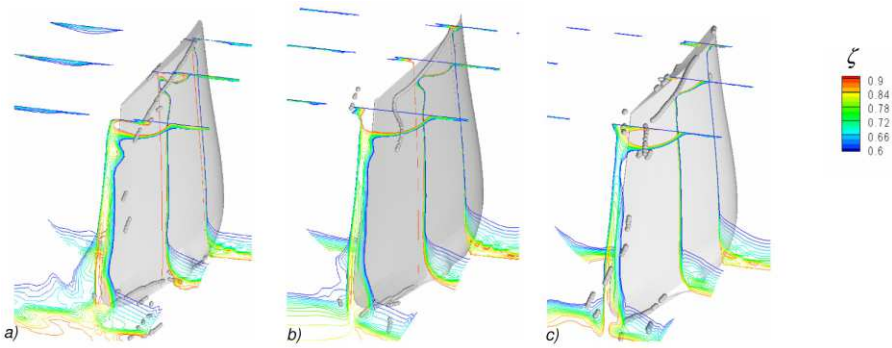

Figure 9. Evolution of total pressure loss coefficient (ζ) inside the blade passage: a) datum rotor, b) AC90/6/TF rotor, and c) AC90/6/TFvte

breakdown, a larger peak loss core was associated with the modified tip configuration of the AC90/6/TF rotor (Figure 10b). A comparison of the AC90/6/TF rotor and the datum rotor loss map at 1.2 ℓ revealed that the modified tip rotor featured a beneficial span-wise loss distribution; it outperformed the datum fan within the wake and on the hub end-wall where it provided healthier near wall layers on pressure- and suction-side corners.

With regard to the AC90/6/TFvte fan rotor (Figure 10c), there was evidence that the control of the leakage-vortex breakdown was able to reduce the high loss core at the tip—both behind the rotor and along the blade suction side within the interaction region between leakage and near surface flows. This can be considered to be a consequence of the reduced 3-D flow rearrangement occurring as a result of the reduction in mass leaking through the tip gap. The limited radial migration of near-wall surface fluid induced smaller hub loss core and contraction of the suction/corner stall (Figures 10b and 10c).

6. **Conclusions**

The aim of the present study was to develop improved tip configurations to control leakage-flow phenomena and rotor aero-acoustic signatures in a family of axial flow fans. The passive control technique explored in the study was based on blade tips that had been modified by the addition of anti-vortex appendages as end-plates. The objective of the modified end-plates was to control the chord-wise evolution of the leakage-vortex swirl level by preventing the occurrence of tip-leakage vortex bursting by the enhancement of near-axis swirl. Two end-plate configurations were investigated: (i) an end-plate with constant thickness; and (ii) an end-plate with a variable thickness distribution according to the concept of a safe rotation number chord-wise gradient.

The aerodynamic tests reported here indicate that the original tip concept demonstrated reduced performance along the operating line, but that this was recovered by the adoption of the end-plate designed according to the concept of the leakage-vortex rotation number. The measured efficiency revealed an improvement with increased peak performance. It was thus apparent that the variable-thickness end-plate was able to provide a wider high-efficiency plateau towards the rotor stall margin.

The loss coefficient distributions confirmed that the highest loss regions were always observed in coincidence with the leakage-vortex core, with a nearly constant peak loss value. The comparative loss behaviour was in accordance with the aerodynamic test results, and the overall efficiency gain for the investigated end-plates was found to be a consequence of the reduced 3-D flow rearrangement caused by the improved tip configurations.

Acknowledgement. The present research was undertaken in the context of a contract (FW-DMA03) between Fläkt Woods Ltd and the Dipartimento di Meccanica e Aeronautica ('Sapienza'), University of Rome. One of the authors (Corsini) acknowledges the assistance provided by the Italian Ministry for Academic Research (MIUR) under the auspices of the 'Ateneo 2005' and 'Facoltà 2005' projects. The authors also thank Bruno Perugini for his contribution to the quantitative analyses.

References

1. Fukano, T. and Takamatsu, Y.: The effects of tip clearance on the noise of low-pressure axial and mixed flow fans. *Journal of Sound and Vibration*, **105**, (1986), 291-308.
2. Furukawa, M., Inoue, M., Kuroumaru, M., Saiki, K. and Yamada, K.: The role of tip leakage vortex breakdown in compressor rotor aerodynamics. *Journal of Turbomachinery*, **121**, (1999), 469-480.
3. Storer, J.A. and Cumpsty, N.A.: Tip leakage flow in axial compressors. *Journal of Turbomachinery,* **113**, (1991), 252-259.
4. Ganz, U.W., Joppa, P.D., and Scharpf, D.F.: Boeing 18-inch fan rig broadband noise test, NASA CR-1998-208704.
5. Takata H. and Tsukuda Y.: Stall margin improvement by casing treatment - its mechanism and effectiveness. *Journal of Eng. for Power*, **99**, (1977), 121-133.
6. Smith G.D.J. and Cumpsty N.A.: Flow phenomena in compressor casing treatment, J. Eng. Gas Turbines Power, 106, (1984), 532-541.
7. Thompson D.W., King P.I., and Rabe D.C.: Experimental and computational investigation on stepped tip gap effects on the flowfield of a transonic axial-flow compressor rotor. *Journal of Turbomachinery*, **120**, (1998), 477-486.
8. Jensen, C.E.: Axial-flow fan, US Patent No. 4,630,993, (1986).
9. Quinlan, D.A. and Bent P.H.: High frequency noise generation in small axial flow fans. *Journal of Sound and Vibration*, **218**, (1998), 177-204.
10. Longet, C.M.L.: Axial flow fan with noise reducing means, US Patent 2003/0123987 A1, (2003).
11. Mimura, M.: Axial flow fan, US Patent 6,648,598 B2, (2003).

12. Uselton, R.B., Cook, L.J. and Wright, T.: Fan with reduced noise generation, US Patent 2005/0147496 A1, (2005).

13. Corsini, A., Perugini, B., Rispoli, F., Kinghorn, I. and Sheard, A.G.: Investigation on improved blade tip concept, ASME Paper GT2006-90592, 2006a.

14. Corsini, A., Rispoli, F. and Sheard, A.G.: Development of improved blade tip endplate concepts for low-noise operation in industrial fans, In Proceedings of Conference on Modeling Fluid Flows CMMF'06, Budapest, 2006b.

15. Corsini, A., Perugini, B., Rispoli, F., Kinghorn, I. and Sheard, A.G.: Experimental and numerical investigations on passive devices for tip-clearance induced noise reduction in axial flow fans, In Proceedings of the 7th European Conference on Turbomachinery, Athens, (2007).

16. Spall, R.E., Gatski, T.B. and Grosch, C.E.: A criterion for vortex breakdown. *Phys. Fluids*, **30**(11), (1987), 3434-3440.

17. Escudier, M.: Confined vortices in flow machinery. *Ann Rev Fluid Mech.*, **19**, (1987), 27-52.

18. Herrada, M.A. and Shtern, V.: Vortex breakdown control by adding near-axis swirl and temperature gradients, Physical Review E, 68, (2003), 041202 1-8.

19. Jones, M.C., Hourigan, K., and Thompson, M.C.: The generation and suppression of vortex breakdown by upstream swirl perturbations, In Proceedings of 14th Australian Fluid Mechanics Conference, Adelaide, Australia, (2001).

20. Srigrarom, S. and Kurosaka, M.: Shaping of delta-wing planform to suppress vortex breakdown, AIAA Journal, 38, (2000), 183-186.

21. Inoue, M., Kuroumaru, M. and Furukawa, M.: Behavior of tip leakage flow behind an axial compressor rotor. *Journal of Gas Turbine and Power*, **108**, (1986), 7-14.

22. Corsini, A. and Rispoli, F.: Using sweep to extend stall-free operational range in sub-sonic axial fan rotors. *Journal of Power and Energy*, **218**, (2004), 129-139.

23. Lucca-Negro, O. and O'Doherty, T.: Vortex breakdown: a review, Progress in Energy and Combustion Science, 27, (2001), 431-481.

24. Leibovich, S.: The structure of vortex breakdown. *Ann Rev Fluid Mech.*, **10**, (1978), 221-246.

25. Escudier, M. and Zehnder, N.: Vortex flow regimes. *Journal of Fluid Mech.*, **115**, (1982), 105-121.

26. Inoue, M. and Furukawa, M.: Physics of tip clearance flow in turbomachinery, ASME paper FEDSM2002-31184, (2002).

27. Leibovich, S.: Wave propagation, instability, and breakdown of vortices, In Hornung, Mueller (eds), Vortex motion, 50-67, (1982).

28. Benjamin, T.B.: The theory of vortex breakdown. *Journal of Fluid Mech.*, 14, (1962), 583-629.

29. Tsai, C-Y. and Widnall, S.E.: Examination of group-velocity criterion for breakdown of vortex flow in a divergent duct. *Phys. Fluids*, **23**, (1980), 864-870.

30. Ito, T., Suematsu, Y. and Hayase, T.: On the vortex breakdown phenomena in a swirling pipe-flow, Nagoya University, Faculty of Engineering, Memoirs (ISSN 0027-7657), 37(2), (1985), 117-172.

31. Leibovich, S.: Vortex stability and breakdown: survey and extension, AIAA Journal., 22, (1984), 1192-1206.

32. Uchida, S., Nakamura, Y., and Ohsawa, M.: Experiments on the axisymmetric vortex breakdown in a swirling air flow. *Trans. Jpn. Soc. Aero Space Sci.*, **27**(78), (1985), 206-216.

33. Garg, A.K. and Leibovich, S.: Spectral characteristics of vortex breakdown flowfields. *Phys. Fluids*, **22**(11), (1979), 2053-2064.

34. Gbadebo, S.A., Cumpsty, N.A. and Hynes, T.P.: Interaction of tip clearance flow and three-dimensional separations in axial compressors, ASME paper GT2006-90071, (2006).

Journal of Computational and Applied Mechanics, Vol. 8., No. 1., (2007), pp. 39–55

NUMERICAL PREDICTIONS OF LOW REYNOLDS NUMBER FLOW OVER AN OSCILLATING CIRCULAR CYLINDER

Eric Didier, António R. J. Borges
Faculdade de Ciências e Tecnologia Universidade de Lisboa
2829-516 Caparica, Portugal
deric@fct.unl.pt

[Received: January 15, 2007]

Abstract. Flow over an oscillating cylinder at $Re = 300$ is simulated. For in–line oscillations, the vortex–shedding frequency locks–on the cylinder frequency in a wide frequency band, around twice the natural vortex–shedding frequency observed for a stationary cylinder. For cross–flow oscillations, lock–in occurs in a narrow frequency band around the natural frequency. When circular motion is simulated the two bandwidths of lock–in are slightly different than those observed for simple in-line or transverse oscillation.

Keywords: finite volume method, fully coupled resolution method, lock-in, circular motion of a circular cylinder, vortex shedding

1. Introduction

Study of flow past a circular cylinder is of special interest for basic understanding of the aerodynamics of aeroelastic phenomena. Despite the simplicity of geometry the flow around a cylinder is very complicated and of particular importance, since it may induce unsteady forces on structures associated with vortex shedding. Unsteady forces acting in both directions, in-line and cross–flow, represented by drag and lift coefficients respectively, can induce structure vibrations. Bodies oscillate in response to these forces, possibly in linear or orbital motion. In such cases the vortex shedding properties will change resulting in quite different lift and drag periodic fluctuations in time.

The time-varying component of the lift force is usually an order of magnitude larger than that corresponding to the drag force. Therefore, in general, the cylinder oscillations are predominantly in the cross–flow direction. For this reason most of the research efforts in the past have been concentrated on cross–flow oscillations. A cylinder that is subjected to forced cross–flow oscillations with an amplitude beyond a certain threshold value exhibits the phenomenon of lock-in. The vortex-shedding frequency of the oscillating cylinder changes to the frequency of cylinder vibrations [1]. Similar observations also apply to cylinders mounted on flexible supports and

allowed to undergo vortex–induced oscillations of sufficient amplitude [2]. The observation that the flow field changes significantly as a result of the cylinder oscillations was already noticed in the computational study of Mittal [3]. Flow past cylinders subjected to forced in-line oscillations was studied experimentally by Griffin [4] and numerically by Chang [5], Mittal [3] and Didier [6]. Flow structure in the wake of an oscillating cylinder has been investigated by many other researchers, e.g. Bearman [7], Okajima [8], Mittal [9], Griffin [10], Lecointe [11], Williamson [12], and Nobari [13]. In some of these studies the cylinder is subjected to oscillations at frequencies that are sub- and super-harmonics of the natural vortex-shedding frequency for a stationary cylinder.

As already mentioned, the cylinder oscillations are predominantly in the cross-flow direction, but strictly speaking the cylinder describes an orbital motion. Vortex-induced vibrations of a circular cylinder placed in an uniform flow at Reynolds number 325 are investigated numerically by Mittal [9]. In this study the cylinder is allowed to vibrate in both directions. In most of the cases, the trajectory of the cylinder corresponds to a Lissajou figure of an 8. Mittal observes that the vortex-shedding frequency of the oscillating cylinder does not match exactly the structural frequency. More recently, Lewis [14] investigated the orbital motion of a circular cylinder in an uniform flow using a vortex cloud flow modelling. Studies of this type were previously undertaken by Baranyi [15, 16] employing a grid-based Eulerian type method for solving the two-dimensional Navier-Stokes equations. Abrupt jumps were found in the time-mean and rms values of lift and drag that seem to be caused by a critical change in the vortex structure.

This paper focuses on the case of uniform flow past an oscillating cylinder in the in-line, cross-flow or both in-line and cross-flow directions that results in an circular motion in the present study. Computations are carried out for various values of the structural frequency, including the natural shedding frequency, and velocity amplitude of cylinder, 10 to 30% of the free-stream velocity. The flow field changes significantly and manifests in the forces experimented by the cylinder and the related Strouhal number.

Computational investigations are performed considering unsteady two-dimensional flow for an incompressible viscous fluid. An implicit second order fully coupled resolution method [17, 18, 19] developed for structured and unstructured meshes with a finite volume framework for cell-centered collocated grids is presented. This approach is an alternative to classical segregated methods, like SIMPLE [20] or PISO [21]. Whereas the segregated methods lead to a sequential resolution of discrete equations, the fully coupled resolution method solves only one linear system in velocity-pressure. This approach does not require correction steps, relaxation parameters or other special treatment to ensure convergence, and reduces the number of non-linear iterations needed to converge. Flow past a stationary cylinder at $Re = 300$ is simulated and provide a good test of the accuracy of the fully coupled resolution method.

2. **Governing equations**

The unsteady two-dimensional Navier-Stokes equations for incompressible viscous fluid are considered in conservative dimensionless integral form and written in the referential of the cylinder.

$$\int_S u_j \, n_j \, dS = 0, \tag{2.1}$$

$$\int_V \frac{\partial u_i}{\partial t} dV + \int_S (u_j n_j) \, u_i dS = - \int_V \frac{\partial p}{\partial x_i} dV + \int_S \frac{1}{Re} \frac{\partial u_i}{\partial x_j} n_j dS - \int_V \frac{\partial u_i^{cyl}}{\partial t} dV. \tag{2.2}$$

These equations involve dimensionless variables: the Cartesian components u_i of the velocity, the pressure p, and the time t. V is the volume of an element, S its area and n_i the components of the outward unit vector normal to the surface, $\overrightarrow{n}$. The Reynolds number Re is defined using the free-stream velocity U_∞, the cylinder diameter D and the fluid viscosity ν.

The motion of the centre of the cylinder is specified as follows:

$$u_1^{Cyl} = u_{e1} cos(2\pi f_{e1} t), \tag{2.3}$$

$$u_2^{Cyl} = u_{e2} sin(2\pi f_{e2} t), \tag{2.4}$$

where u_{e1}, u_{e2} and f_{e1}, f_{e2} are the dimensionless amplitude velocities and frequencies of the cylinder oscillatory motion in the in-line and cross-flow directions. When the two amplitudes and frequencies are equal, $f_{e1} = f_{e2}$ and $u_{e1} = u_{e2}$, the motion path becomes a circle. If one of the amplitudes is zero, longitudinal or transverse oscillation is obtained. Evidently when both amplitudes are zero the cylinder is stationary.

3. **Fully coupled resolution method**

3.1. **Introductory remarks.** The fully coupled resolution method is developed for structured and unstructured grids and unsteady flow within a finite volume framework. This method differs from segregated formulations by the implicit treatment of pressure-velocity coupling. Only one linear system is solved and no relaxation parameters or special operations are required to ensure convergence.

3.2. **Finite volume mesh convention.** Finite volume discretization schemes are used with collocated cell-centered unknowns. The central control volume is denoted by c and the neighbouring control volumes are denoted by nb. M_{nb} is the midpoint of the face shared by two adjacent cells. For a non-orthogonal grid, the face midpoint may be different from the point defined by the intersection cell-centroids line and the face. Therefore a correction is required to transfer the values from the cell center c and nb to the points c' and nb' (Figure 1).

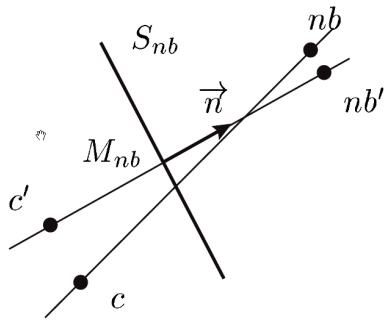

Figure 1. Interface of two adjacent cells and notation for discretization

3.3. **Discretization schemes.** The fully coupled resolution method involves solving a complex linear system of algebraic equations. It is thus necessary to consider compact implicit schemes, based only on the adjacent cells, conserving in the same time a precision of second order.

An implicit three-level second order scheme is used to discretize the transient term [22].

Central differencing scheme, that involves only the values of adjacent cells, is used to evaluate the viscous term.

The pressure term is calculated using a linear interpolation between the cells centre c' and nb'.

The advection term is calculated using the deferred correction approach [23], combining a first-order UDS and a higher-order scheme, WACEB [24], with the factor ω_{DC} set to 1. At non-linear convergence, the advection term is of WACEB scheme order, e.g. third order. The i^{th} component velocity at the interface f of the control volume can be written as follows:

$$(u_i)_f = \left(u_i^{UDS}\right)_f^{implicit} + \omega_{DC}\left(u_i^{WACEB} - u_i^{UDS}\right)_f^{explicit}. \tag{3.1}$$

When the grid is non-orthogonal, corrections are required to estimate pressure and velocity at the midpoint of the face. These corrections, involving gradients evaluated at the element's centroid using the Gauss theorem, are small compared to the other, if the grid non-orthogonality is not severe. They are added explicitly to the source term of discrete equations.

3.4. **Fully coupled system.** The momentum equation can be written as follows:

$$(u_i)_c = b^{u_i} + \frac{1}{a_c^{u_i}} \sum_{nb} a_{nb}^{u_i} (u_i)_{nb} - \frac{1}{a_c^{u_i}} \left(a_c^p \, p_c + \sum_{nb} a_{nb}^p \, p_{nb} \right). \tag{3.2}$$

The source term b^{u_i} gathers contributions of the explicit part of discretization schemes.

Following Prakash and Patankar [25], the convected velocity $(u_i)_c$ can be considered as the sum of a pseudo-velocity $(u_i^*)_c$ and a pressure gradient term:

$$(u_i)_c = (u_i^*)_c - \left(\frac{a_c^p}{a_c^{u_i}} p_c + \sum_{nb} \frac{a_{nb}^p}{a_c^{u_i}} p_{nb} \right). \tag{3.3}$$

The pseudo-elocity gathers all contributions of discrete momentum equations, except the pressure gradient contribution:

$$(u_i^*)_c = b^{u_i} + \sum_{nb} \frac{a_{nb}^{u_i}}{a_c^{u_i}} (u_i)_{nb}. \tag{3.4}$$

The continuity equation (2.1) is expressed in discrete form as follows:

$$\sum_{nb} (u_i n_i)_{nb} S_{nb} = 0. \tag{3.5}$$

It requires a mass flux specification, at the interfaces of the control volume surrounding the node c. The velocity (u_i) in this equation is obtained from relation (3.3). Then, the continuity equation, expressed in terms of pseudo-velocity and reconstructed pressure [26], allows to obtain a pressure equation.

$$\sum_{nb} \left(\left(u_i^* - \left(\frac{a_c^p}{a_c^{u_i}} p_c + \sum_{nb} \frac{a_{nb}^p}{a_c^{u_i}} p_{nb} \right) \right) n_i \right)_{nb} S_{nb} = b^p. \tag{3.6}$$

3.5. **Resolution strategy.** The fully coupled system is constructed gathering equations (3.3), (3.4) and (3.6). In the linear system (3.7), $\mathbf{I}$ is the identity matrix, $\mathbf{G}$ denotes the gradient operator, $\mathbf{C}$ gathers the off–diagonal influence coefficients of the convective–diffusion scheme, $\mathbf{D}$ denotes the divergence operator, and $\mathbf{S}$ represents the explicit part of discrete equations.

$$\begin{bmatrix} \mathbf{I} & -\mathbf{I} & \mathbf{G} \\ \mathbf{C} & \mathbf{I} & 0 \\ 0 & \mathbf{D} & -\mathbf{DG} \end{bmatrix} \begin{bmatrix} \mathbf{U} \\ \mathbf{U}^* \\ \mathbf{P} \end{bmatrix} = \begin{bmatrix} 0 \\ \mathbf{S}_{\mathbf{U}^*} \\ \mathbf{S}_{\mathbf{p}} \end{bmatrix}. \tag{3.7}$$

The matrix of this linear system is sparse, non–symmetrical, with a large dimension and an ill–conditioned pressure block. The linear system is solved using the iterative algorithm $BiCGSTAB - \omega$ [27], in conjunction with a LU preconditioner.

In opposition to segregated methods, like SIMPLE [20] or PISO [21], that lead to a sequential resolution of discrete equations, the fully coupled resolution method allows to solve only one single linear system, gathering pressure and velocity, to obtain the solution. The residual convergence is fast due to the implicit velocity-pressure coupling. A residual reduction of six to seven orders is obtained in a few number of non-linear iterations (Figure 3). At the beginning of the non-linear process, a rather high number of iterations is mandatory to solve the linear system, see Figure 2, and a severe variation of normalized residual is observed, Figure 3. This step corresponds to the main non-linear reduction phase.

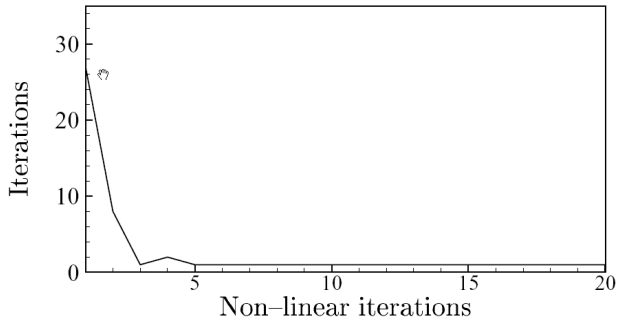

Figure 2. Convergence history for a stationary cylinder, $Re = 300$, at $t = 100$: number of iterations to solve the fully linear system during the non-linear convergence process

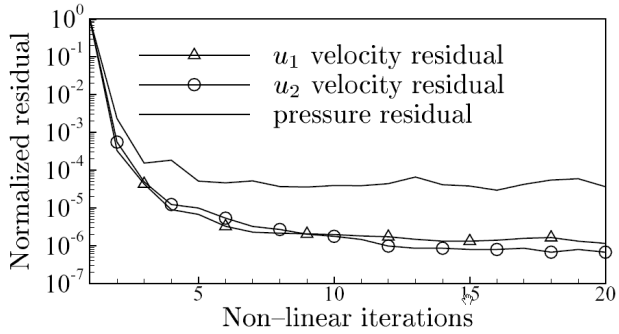

Figure 3. Convergence history of non-linear normalized residue convergence for a stationary cylinder, $Re = 300$, at $t = 100$

4. **CFD results and discussion**

CFD results at $Re = 300$ are presented for motions with various velocity amplitudes and frequencies, namely: 10, 20 and 30% of the free-stream velocity and normalized frequencies between 0.2 and 3.0. Before simulating the flow past an oscillating cylinder, the stationary cylinder is considered first. It serves as a reference to analyse forces and flow topology when oscillations occur. These reference values are represented by a thin horizontal line in figures that present drag and lift coefficient, and Strouhal number.

4.1. **Stationary cylinder.** In this section the flow around a stationary cylinder is considered, since it shall provide a good test of the accuracy of the fully coupled resolution method and, additionally, shall function as a reference to the subsequent, more elaborate cases. A preliminary grid refinement study revealed that an O–grid with 200 and 155 nodes in angular and radial direction, respectively, with a first

grid–point near to the wall situated at $5 \times 10^{-4} D$ is well adapted to the present simulation. To ensure that external boundary effects are sufficiently minimized the integration volume has a radius equal to $50D$ (Figure 4). The time step is equal to 10^{-2}.

Table 1. Comparison of present results with literature data

	Present method	Singh [28]	Henderson from [29]	Nobari [13]	Roshko from [13]	Schlichting [30]
$\bar{C}_{D_o}$	1.352	1.357	1.360	1.365	-	1.378
St_o	0.214	0.210	0.212	0.207	0.21	-

Table 1 presents the drag coefficient and the Strouhal number, $St = fD/U_\infty$, with f being the vortex–shedding frequency. The present results exhibit good agreement with numerical results of Singh [28], Nobari [13] and Henderson, from Williamson [29], and experimental data of Roshko, from [13], and Schlichting [30]. The rms of drag and lift coefficients, $C_{D_o,rms}$ and $C_{L_o,rms}$, are equal to 5.3×10^{-2} and 0.62 respectively. Efficiency and accuracy of the present resolution method were demonstrated by the authors in [19, 31, 6].

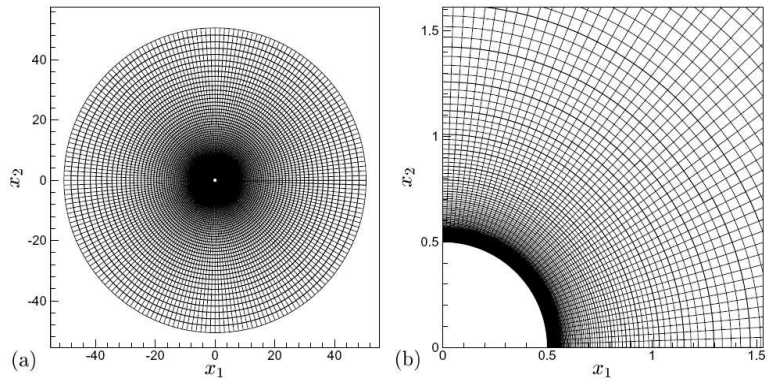

Figure 4. Computational O–grid around the cylinder: (a) overall view and (b) detail near the wall

4.2. **In-line oscillation.** When in-line oscillation occurs, the cylinder oscillates only in the direction of the free-stream velocity. Calculated Strouhal number and drag coefficient are presented in Figures 5(a) and 5(b). Figures 5(c) and 5(d) show the rms drag and lift coefficients versus the normalized in-line excitation frequency f_{e1}/f_o, with f_o being the natural frequency of vortex shedding for a stationary cylinder in an uniform flow.

It can be observed that the in-line oscillation alters the flow field significantly, as has been reported by various authors [5, 3, 6]. These effects manifest themselves in the forces experienced by the cylinder and the related Strouhal numbers for the vortex-shedding frequencies.

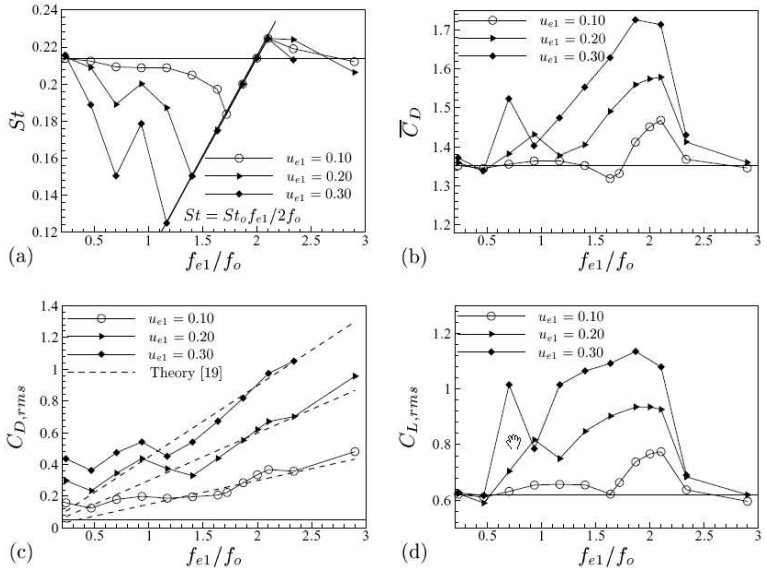

Figure 5. In–line oscillation: (a) Strouhal number, (b) mean drag coefficient, (c) drag coefficient rms and (d) lift coefficient rms

As can be seen in Figure 5(a), in-line cylinder oscillations cause a global diminution of the shedding frequency. This is not true for frequencies higher than $2f_o$, where the Strouhal number is either higher or equal than St_o. The minimum shedding frequency decreases when velocity amplitude of the cylinder increase. The shedding frequency locks-on the excitation frequency, in a large frequency band for frequencies lower or slightly higher than $2f_o$, with the following relation: $St/St_o = f_{e1}/2f_o$. The bandwidth of lock-in increases with the amplitude of velocity oscillation. For $f_{e1} = 2f_o$ the lock-in is strong, the shedding frequency is equal to the natural shedding frequency. This effect is called synchronization.

The longitudinal and transversal forces acting on the cylinder globally increase when compared to the values calculated for stationary uniform flow. Mean drag and rms lift coefficients are larger when lock-in occurs. Maximum values of mean drag and rms lift coefficients take place for synchronization, i.e. $f_{e1} = 2f_o$. However, another smaller peak appears when $f_{e1} \sim f_o$ for the larger amplitude velocity fluctuation. For normalized frequency f_{e1}/f_o under 0.3 or above 2.7, mean drag and rms lift coefficients converge to the values of the stationary cylinder case. The rms drag coefficient does not follow this behaviour and increases with frequency. This is connected with

inertial effects. Effectively, numerical values agree well with the theoretic formulation, considering the added mass and neglecting viscous effects. This agreement is especially observed at high frequencies where the inertial effects dominate the viscous non-linear phenomenon, as shown previously in [6].

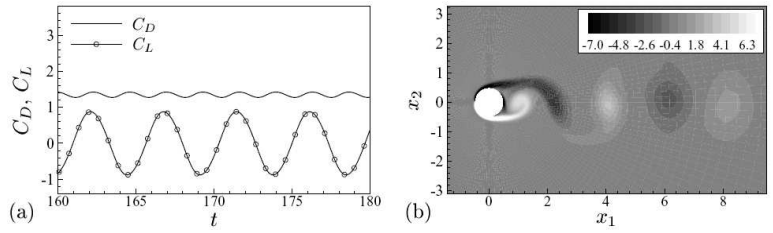

Figure 6. Stationary cylinder: (a) drag and lift coefficients and (b) vorticity field

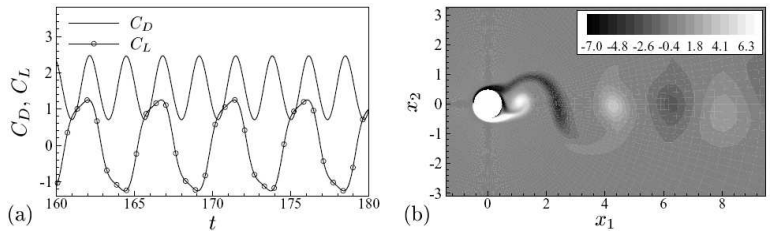

Figure 7. In-line oscillation, $f_{e1}/f_o = 2$ and $u_{e1} = 0.20$: (a) drag and lift coefficients and (b) vorticity field

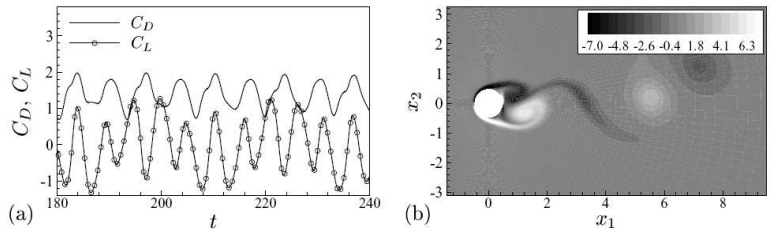

Figure 8. In-line oscillation, $f_{e1}/f_o = 0.7$ and $u_{e1} = 0.20$: (a) drag and lift coefficients and (b) vorticity field

Figures 6(a) and 7(a) show the time history of drag and lift coefficients for a stationary cylinder and for an in-line cylinder oscillation in an uniform flow, with $u_{e1} = 0.20$ and $f_{e1}/f_o = 2$. Figures 6(b) and 7(b) show the vorticity field at the

non-dimensional time $0.1/St$, considering the temporally periodic solution for the two cases. As can be seen, the *rms* lift coefficient is larger than the natural one. The C_L temporal signal becomes asymmetric, while the uniform flow lift coefficient is harmonic. This is a characteristic feature of the lock-in phenomena. As can be seen in Figures 6(b) and 7(b), the near vorticity field is rather affected by the cylinder oscillations. The structure of positive and negative vorticity is significantly modified.

The time history of drag and lift coefficients, for a low oscillation frequency with $u_{e1} = 0.20$ and $f_{e1}/f_o = 0.70$, are presented in Figure 8. The flow topology is strongly modified comparing with the flow past a stationary cylinder. Vortex structures depart from the classical vortex-street pattern. As expected, the forces acting on the cylinder are very variable. A spectral analysis, presented in the next section, shows that other frequencies appear due to the combination of the frequency f_{e1} and the vortex-shedding frequency.

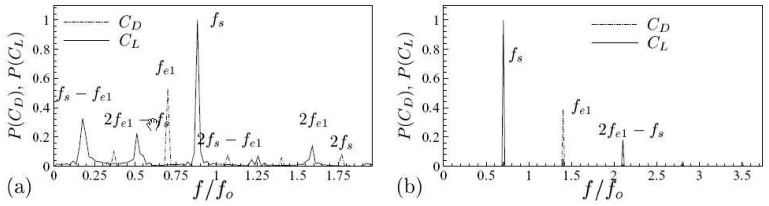

Figure 9. Power spectra for in-line oscillation, $u_{e1} = 0.20$: (a) $f_{e1}/f_o = 0.7$ and (b) $f_{e1}/f_o = 1.4$

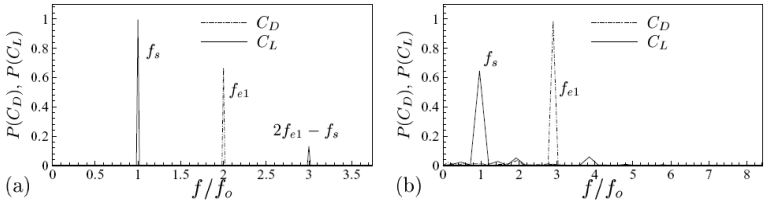

Figure 10. Power spectra for in-line oscillation, $u_{e1} = 0.20$: (a) $f_{e1}/f_o = 2$ and (b) $f_{e1}/f_o = 2.9$

The normalized power spectra for four oscillation frequencies is presented in Figures 9(a) and 9(b), $f_{e1}/f_o = 0.7$ and $f_{e1}/f_o = 1.4$, and Figures 10(a) and 10(b), $f_{e1}/f_o = 2$ and $f_{e1}/f_o = 2.9$. Observation of these figures reveals that in-line cylinder oscillation causes interferences between the cylinder motion and the vortex-shedding which can result in the appearance of additional frequencies in the spectrum. Around the oscillation frequency $f_{e1} = 0.7$ the spectrum is rich. Observed frequencies result from the combination of the oscillation frequency f_{e1} and the vortex-shedding frequency f_s: $f_s - f_{e1}$, $2f_{e1}$, $2f_s$, $2f_s - f_{e1}$ and $2f_{e1} - f_s$. Dominant frequencies are those

associated with the lift coefficient signal. When lock-in occurs, like for $f_{e1}/f_o = 1.4$ and $f_{e1}/f_o = 2$, vortex-shedding locks-on to the oscillation frequency. In the spectrum, the oscillation frequency f_{e1} and the vortex-shedding frequency $f_s = f_{e1}/2$ appear. A single additioned frequency appears, $2f_{e1} - f_s$. For an higher frequency, like $f_{e1}/f_o = 2.9$, only the oscillation frequency and the vortex-shedding frequency are identified in the spectrum.

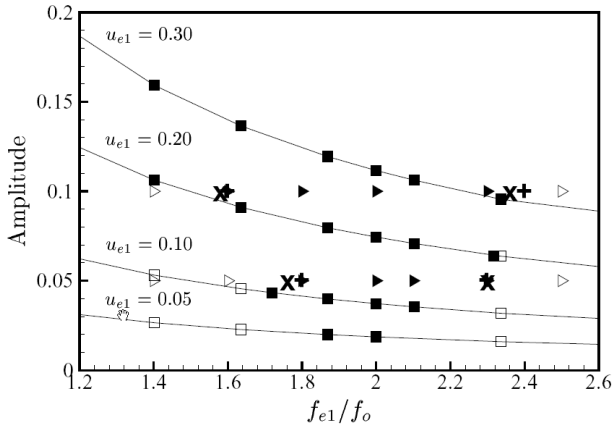

Figure 11. Simulation points for in-line oscillation at $Re = 300$. Lock-in does not occur (□) and lock-in occur (■). Bounds of the lock-in region: (+). Results of Griffin [4] at $Re = 190$, (x) results of Hall [32] at $Re = 200$.(▷). Numerical results of Nobari [13] at $Re = 300$

The simulation results for values of velocity amplitude, transformed in motion amplitude, and frequency oscillations are presented in Figure 11. These results are compared with the numerical results of Nobari [13] at $Re = 300$ and experimental data obtained by Griffin [4] and Hall [32], respectively at $Re = 190$ and $Re = 200$. Bounds of the lock-in region, adapted from the results of Griffin[4], are plotted. Solid circles indicate occurrence of lock-in. As has been demonstrated by the authors in [6], the lock-in bandwidth is Reynolds number dependent, between $Re = 100$ to $Re = 300$. The lock-in bandwidth increases when Reynolds number increases: the upper bound of lock-in frequency region is rather affected and is slightly higher than $f_{e1}/f_o = 2$, but the lower bound decreases. The present computational results are in reasonable agreement with available experimental data and in good accordance with computational results obtained by Nobari [13] with a finite element method.

4.3. **Cross-flow oscillation.** Figures 12(a), 12(b) and 13 show the Strouhal number, the mean and *rms* drag coefficient versus the normalized cross-flow excitation frequency f_{e2}/f_o.

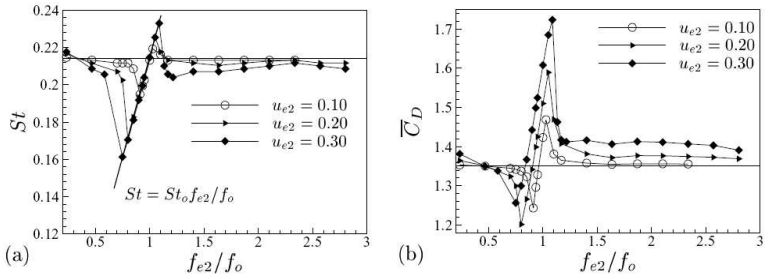

Figure 12. Cross-flow oscillation: (a) Strouhal number and (b) mean drag coefficient

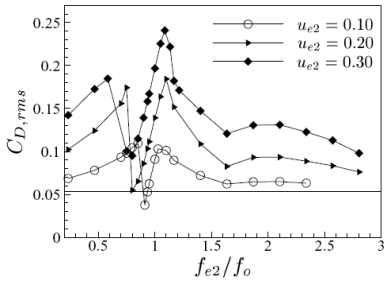

Figure 13. Cross-flow oscillation: *rms* drag coefficient

Cross-flow oscillations cause only a significant variation of the shedding frequency in a band around the natural shedding frequency f_o. This frequency band is narrowed compared with that obtained for an in-line oscillation. The shedding frequency locks-on the excitation frequency, with the following relation: $St/St_o = f_{e2}/f_o$. For $f_{e2}/f_o = 1$ the shedding frequency equals the natural frequency. It is the synchronization. The lock-in frequency band increases with amplitude velocity of cylinder. For the higher excitation frequencies it can be seen that the Strouhal number is slightly lower than the natural Strouhal number. However, Strouhal number, mean drag and *rms* drag coefficients tend toward natural St_o, $\overline{C}_{D_o}$ and $C_{D_o,rms}$.

For each amplitude the mean drag coefficient presents a linear variation in the lock-in zone, like the *rms* drag. For low lock-in frequencies the mean drag is slightly lower than the natural one. For the higher lock-in frequency the mean drag is maximum and much higher than the natural drag. The *rms* drag coefficient presents a type of crisis before the lock-in zone. The $C_{D,rms}$ decrease to reach its minimum value. It then increases, linearly, in the lock-in band up to its maximum value before decreasing again, slowly, tending to the natural $C_{D_o,rms}$. This abrupt jump can be caused by a critical change in vortex the structure.

4.4. **Circular motion.** Computations are carried out for equal cylinder amplitude velocity, $u_{e1} = u_{e2}$, set to 10% of the free-stream velocity. In-line and cross-flow motion frequencies are equal and denoted f_e. Results are compared with reference values and with results obtained for in-line and cross-flow oscillations.

Figures 14(a) and 14(b) show the Strouhal number and the mean drag coefficient against the normalized frequency. The lock-in occurs in two frequency bands around $f_e/f_o = 1$ and $f_e/f_o = 2$. However, frequency lock-in bands are different than those obtained for in-line or cross-flow oscillating cylinder. The first one is located in the normalized frequency interval 0.94 to 1 and can be defined by the relation $St = St_o f_e/f_o$. The lock-in occurs in a restricted bandwidth, narrower than the frequency band associated to the cross-flow oscillation cylinder motion. The second one, defined by $St = St_o f_e/2f_o$, appears between 1.63 to 2.13. The lock-in bandwidth is slightly broader than the frequency band defined for an in-line oscillating cylinder.

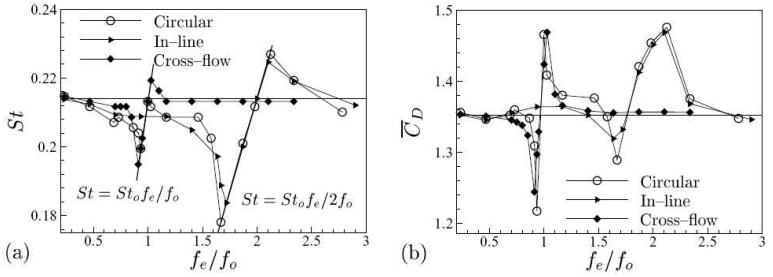

Figure 14. Circular oscillation: (a) Strouhal number and (b) mean drag coefficient

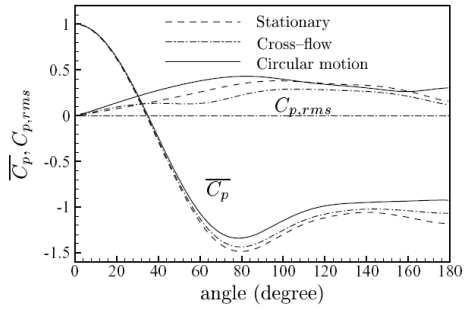

Figure 15. Mean and *rms* pressure coefficient for $f_e/f_o = 0.94$ and $u_{e1} = u_{e2} = 0.10$

In Figure 14(b), it can be seen that the mean drag variation in the first lock-in band, around $f_e/f_o = 1$, is not equal to mean drag evolution obtained for cross-flow cylinder motion. Firstly, the band frequency is smaller. Secondly, minimum and

maximum mean drag coefficient values in the lock-in band are larger. The jump of mean drag coefficient in this lock-in zone presents a slightly larger amplitude than that occurring for cross-flow motion.

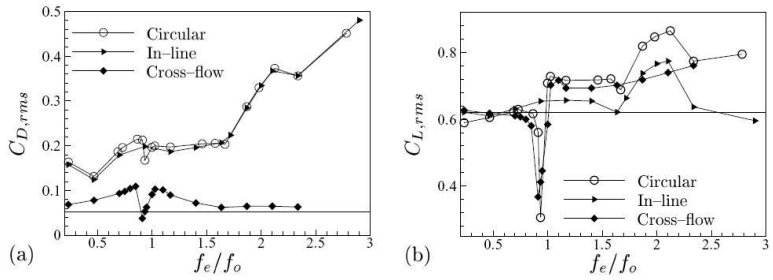

Figure 16. Circular oscillation: (a) *rms* drag and (b) *rms* lift coefficients

Figure 15 shows the mean and *rms* pressure coefficients on the cylinder surface in transversal and circular motion, compared with a stationary one. Mean $\overline{C}_p$ values are similar for all cases in the front region of the cylinder. Beyond 80 degrees, the mean $\overline{C}_p$ for circular motion is larger than the others, like the $C_{p,rms}$, and minimum mean drag coefficient is smaller than for the other motions. Flow topology analysis shows that, for circular motion, the separation points move further downstream. Hence, the variation of mean drag coefficient is larger than that obtained for the cross-flow cylinder motion. The line slope defined by df_e/df_o is twice that obtained for cross-flow only oscillation. For high frequencies, around $f_e/f_o = 2$, the mean drag coefficient is similar to that of in-line oscillation.

Figures 16(a) and 16(b) show the *rms* drag and lift coefficients. Inertial effects are observed for both coefficients at higher frequencies. As can be seen in Figure 16(a), the *rms* drag coefficients for circular cylinder motion and in-line motion present a similar evolution. Only small lock-in effects are observed around $f_e/f_o = 1$ and $f_e/f_o = 2$. In Figure 16(b), evolution of *rms* lift coefficient is similar than that obtained for cross-flow motion of cylinder: inertial effects are observed like the influence of the lock-in in the band frequency around $f_e/f_o = 2$. The jump of *rms* lift coefficient in the lock-in zone, around $f_e/f_o = 1$, presents a slightly larger intensity than that obtained for cross-flow oscillating cylinder. Particularly, the *rms* lift coefficient is almost half than the reference value. Like the mean drag coefficient, the line slope variation df_e/df_o is twice that obtained for cross-flow only oscillation. This effect is clearly induced by the in-line component of the circular motion of the cylinder.

5. **Conclusions**

Numerical simulation of flow past an oscillating cylinder in an uniform free-stream was done using an implicit fully coupled second order resolution method, developed by the first author. This constitutes an original approach to solve Navier-Stokes

equations. Numerical simulation of the flow past a stationary circular cylinder shown the efficiency and accuracy of this resolution method.

Lock-in and synchronisation were observed for all cases studied: for in-line and cross-flow cylinder oscillation and for the various amplitudes of cylinder motion. The cylinder in-line and cross-flow oscillations of sufficient amplitude alter the flow field significantly, and consequently the time-varying forces acting on the cylinder.

For in-line oscillations, the shedding frequency locks-on the excitation frequency, in a large frequency band for frequencies lower or slightly higher than $2f_o$, with the following relation: $St/St_o = f_{e1}/2f_o$. In comparison with the stationary cylinder, the flow is perturbed in a large band of normalized frequencies, between 0.3 to 2.6. Mean drag and rms lift coefficients are both larger than the natural values when lock-in occurs and also for the normalized frequency band 0.25 to 2.6.

For cross-flow oscillations, the flow is disturbed in a narrower frequency band. The shedding frequency locks-on the cross-flow oscillation around the natural frequency f_o, with the following relation: $St/St_o = f_{e2}/f_o$. Mean drag and rms drag and lift coefficients present a sharp variation in this narrow band. The lock-in bandwidth is narrower in this case. The abrupt jump and drop observed in the $C_{D,rms}$ can be caused by a critical change in vortex structure.

The analysis of the circular motion of the cylinder shows that aerodynamical coefficients and the related Strouhal number include contributions from in-line and cross-flow motions. However, differences are observed: first, lock-in bandwidth is narrower than the cross-flow one; second, lock-in zone is broader than the in-line one; the slope of mean drag and rms lift coefficients in lock-in band, around $f_e/f_o = 1$, is twice the slope obtained for the cross-flow oscillation. Those differences are clearly due to the cylinder circular motion. Around $f_e/f_o = 2$, mean drag and rms lift coefficient are not significantly affected by the circular motion if compared with the in-line ones. The rms drag coefficient is not modified in this case.

References

1. Koopmann, G.H.: The vortex wakes of vibrating cylinders at low Reynolds numbers. *J. Fluid Mech.*, **28**, (1967), 501-512.
2. Griffin, O.M., Skop, R.A. and Koopmann, G.H.: The vortex-exited resonant vibrations of circular cylinders. *J. Fluid Mech.*, **54**, (1973), 235-249.
3. Mittal, S. and Tezduyar, T.E.: A finite element study of incompressible flows past oscillating cylinders and airfoils. *Int. J. Numer. Methods Fluids*, **15**, (1992), 1073-1118.
4. Griffin, O.M. and Ramberg, S.E.: Vortex shedding from a cylinder vibrating in line with an incident uniform flow. *J. Fluid Mech.*, **75**, (1975), 257-271.
5. Chang, K.S. and Sa, J.Y.: Patterns of vortex shedding from an oscillating circular cylinder, *JAIAA J.*, **30**, (1992), 1331-1336.
6. Didier, E., Borges, A.R.J. and Gil, L.: Simulação numérica da interacção entre un corpo cilindrico e un escoamento flutuante usando um método de resolução totalmente acoplado, In Proceedings of Congreso de Métodos Numericos en Ingennieria, Granada, Spain, (2005).

7. Bearman, P.W., Downie, M.J., Graham, J.M.R. and Obasaju, E.D.: Forces on cylinders in viscous oscillatory flow at low Keulegan-Carpenter number. *J. Fluids Mechanics*, **154**, (1985), 337-356.

8. Okajima, A.: Numerical analysis of the flow around an oscillating cylinder, In Proceedings of Sixth International Conference on flow-Induced Vibration, London, Great Britain, (1995), pp. 159-166.

9. Mittal, S. and Kumar, V.: Finite element study of vortex-induced cross-flow and in-line oscillations of a circular cylinder at low Reynolds numbers. *Int. J. Numer. Meth. Fluids*, **31**, (1999), 1087-1120.

10. Griffin, O. M.: The unsteady wake of an oscillating cylinder at low Reynolds number. *J. Appl. Mech.*, *38*, (1971), 729-738.

11. Lecointe, Y., Piquet, J. and Plantec, J.: Flow structure in the wake of an oscillating cylinder, In Proceedings of Forum on Unsteady Flow Separation, Cincinanti, USA, (1987), pp. 147-157.

12. Williamson, C. H. K. and Roshko, A.: Vortex formation in the wake of an oscillating cylinder. *J. Fluids Struct.*, **2**, (1988), 355–381.

13. Nobari, M. R. H. and Naderan, H.: A numerical study of flow past a cylinder with cross flow and inline oscillation. *Computers Fluids*, **35**, (2006), 393-415.

14. Lewis, R.I.: Application of the vortex cloud flow modelling to cylinders in orbital motion at low Reynolds numbers and comparisons with some published grid-based CFD predictions, In Proceedings of Conference on Modelling Fluid Flow, Budapest, Hungary, (2006), pp. 157-164.

15. Baranyi, L.: Numerical simulation of flow past a cylinder in orbital motion. In Proceedings of Conference on Modelling Fluid Flow, Budapest, Hungary, 2003, pp. 365-372.

16. Baranyi, L.: Lift and Drag evaluation in translating and rotating non-inertial systems. *J. Fluids Struct.*, **20**, (2005), 25-34.

17. Deng, G.B., Piquet, J., Vasseur, X. and Visonneau, M.: A new fully coupled method for computing turbulent flows. *Comput. Fluids*, **30**, (2001), 445-472.

18. Ammara, I. and Masson, C.: Development of a fully coupled control–volume finite element method for incompressible Navier-Stokes equations. Int. J. Numer. Meth. Fluids, **44**, (2004), 621-644.

19. Didier, E. and Borges, A.R.J.: Unsteady Navier-Stokes equations: A fully coupled method for unstructured mesh, In Proceedings of Conference on Modelling Fluid Flow, Budapest, Hungary, (2003), pp. 814-821.

20. Issa, R.I.: Solution of the implicit discretized fluid flow equations by operator-splitting, J. Comp. Physics, (1985), 40-65.

21. Patankar, S.V.: Numerical Heat Transfer and Fluid Flow, McGraw–Hill Book Compagny, New York, 1980, ISBN 007 048-7405.

22. Ferziger, J.H. and Peric, M.: *Computational Methods for Fluid Dynamics.* Springer-Verlag, Berlin, (1999), ISBN 3–540-65373–2.

23. Khosla, P. and Rubin, S.: A diagonally dominant second-order accurate implicit scheme. *Comput. Fluids*, **2**, (1974), 207-209.

24. Song, B., Liu, G.R., Lam K.Y. and Amano,R.S.: On a higher-order bounded discretization scheme. *Int. J. Numer. Meth. Fluids*, **32**, (2000), 881-897.

25. Prakash, C. and Patankar, S.V.: A control-volume-based-finite-elemet method for solving the Navier-Stokes equations using equal-order velocity-pressure interpolation. *Num. Heat Transfer*, **8**, (1985), 259-280.

26. Rhie, C.M. and Chow, W.L.: A numerical Study of turbulent flow past an isolated airfoil with trailing edge separation. *A.I.A.A. J.*, **21**, (1983), 1525-1532.

27. Sleijpen, G.L.G. and Van der Vorst, H.A.: Maintaining convergence properties of BiCGSTAB methods in finite precision arithmetic. *Numer. Algorithms*, **10**, (1995), 203-223.

28. Singh, S.P. and Mittal, S.: Shear layer instability and drag crisis. *Int. J. Numer. Meth. Fluids*, **47**, (2005), 75-98.

29. Williamson, C.H.K.: Vortex dynamics in the cylinder wake. *Annu. Rev. Fluid. Mech.*, **28**, (1996), 477-539.

30. Schlichting, H.: Boundary-layer theory, McGraw–Hill Book Compagny, New York, (1978).

31. Didier, E. and Borges, A.R.J.: Numerical simulation of two-dimensional flow past a cylinder using an unstructured mesh based fully implicit second order coupled method, In Proceedings of 4th European & African Conference on Wind Engineering, Praha, Tchecoslovaky, (2005).

32. Hall, M.S. and Griffin, O.M.: Vortex shedding and lock-on in a perturbed flow. *J. Fluid. Eng.*, (1993), 115-283.

Journal of Computational and Applied Mechanics, Vol. 8., No. 1., (2007), pp. 57–70

A NUMERICAL STUDY ON THE FREE-SURFACE CHANNEL FLOW OVER A BOTTOM OBSTACLE

Csaba Hős, László Kullmann
Budapest University of Technology and Economics (BUTE),
Department of Hydrodynamic Systems
1111 Budapest, Műegyetem rkp. 3.
csaba.hos@hds.bme.hu

[Received: March 19, 2007]

Abstract. This paper presents the results of a numerical study on a two-dimensional free-surface channel flow over a bottom obstacle. Of main interest is the capability of commercial CFD codes to solve such problems. ANSYS CFX 10.0 was used with its built-in two-phase flow model. While keeping the upstream water level in the channel constant, the downstream water level was systematically decreased, which results in increasing flow rate, supercritical flow, transcritical flow and weak hydraulic jump. The surface shapes of the subcritical CFD computations are compared to the results of the classic 1D theory. In the supercritical case, the parameters - wave crest and toe heights - of undular hydraulic jumps obtained by CFD are compared to the classic theory and to experimental results.

Keywords: open channel flow, undular hydraulic jump

1. Introduction

Free-surface flows and hydraulic jumps are important for environmental engineering (river flows, sediment distribution), ship engineering, water turbine engineering etc. The actual problem motivating this paper was the need for open-surface channel modelling for the steady-state calculation of an urban water supply network. The basic concept was to verify the results of the model based on the classic 1D theory by means of 2D Computational fluid dynamics (CFD) simulations. Furthermore, classic theory gives only limited description of the flow but cannot handle e.g. supercritical cases. Also, there are parameters (notably the friction coefficient), which are hard to estimate. Finally, two-dimensional (and three-dimensional) effects are interesting as understanding these issues might help to improve the simple 1D models.

The classic models on free-surface flows are based on the shallow water equations (see [1] or [2]), neglecting the deviation from the hydrostatic pressure distribution (vertical accelerations). These simple models are suitable only for purely subsonic or supersonic flows and more sophisticated models are needed for transonic flows and hydraulic jumps. The hydraulic jump is a spectacular phenomenon, with a lot of

turbulence, waves, unsteadiness and air entrainment, hence seems to be an appropriate test case for advanced numerical techniques of fluid mechanics.

Hydraulic jumps (analogous to shock waves in gas dynamics) are easily formed in free-surface flows as the wave velocity ($\sqrt{gh}$ in rectangular channels, h being the fluid depth) is often in the same order of magnitude as the flow velocity scale. The transition from supercritical to subcritical flows occurs via hydraulic jumps, through which the well-known 1D models describing the surface shape are not valid. Hydraulic jumps are not only challenging from the theoretical viewpoint (e.g. lack of an inviscid solution, deviation from the hydrostatic pressure distribution [3], presence of multiple scales [10]) but also raise problems in numerical modelling due to the sharp local gradient in the surface shape near the jump. Advanced numerical techniques employed to solve such problems start from finite difference methods [11], include local time stepping techniques [13] and generalised Riemann solvers [12] and attain full growth in the 3D RANS models as e.g. in [6] or [5]. Systematic measurements were also performed, see e.g. [3], [4], [9] and [8]. Ohtsu in [8] and Chanson in [9] give flow conditions for undular jump formation in terms of the Froude number (being the ratio of flow and wave velocity) and channel width, consider Reynolds number effects, describe the main flow patterns and classifies the hydraulic jumps. They also report on the velocity and pressure distribution under the wave crests and at the wave toes.

The aim of the present paper is to test the capabilities of a commercial CFD code (ANSYS CFX 10.0) in terms of free-surface flows on a test case with subcritical and weakly supercritical flows. The paper is organised as follows. First, the classic theory is briefly summarised. Then, the CFD set-up (grid, turbulence model, boundary conditions, etc.) is presented. The results are split into two groups; subcritical and supercritical cases. The results of subcritical cases are compared to the classic 1D theory. The numerical results of the supercritical cases are finally compared to measurements.

2. **Theory**

In this section we briefly summarise some classic theoretical results of the corresponding literature. Consider the free-surface flow of an incompressible fluid in a channel of uniform width. In the case of steady-state behaviour, the losses in the flow (friction head loss) are compensated by the bottom slope. The flow is governed by the Bernoulli (energy) equation

$$\frac{d}{dx}\left(y + z + \frac{v^2}{2g} + h'\right) = 0, \tag{2.1}$$

where y denotes the water height, z represents the bottom contour and h' is the head loss. The continuity equation can be written as

$$Q = Byv = \text{const.} \tag{2.2}$$

with channel width B and average flow velocity v. Note that (2.1) assumes uniform velocity distribution (straight streamlines) and hydrostatic pressure distribution along

the depth. For most open-channel flows, the friction factor is independent of the Reynolds number and is only a function of the wall roughness. Its actual value is usually calculated by means of the Chézy rule by virtue of

$$\frac{dh'}{dx} = \frac{v^2}{C^2\, R_h}, \text{ where } C = R_h^{1/6}/n. \tag{2.3}$$

Here R_h is the hydraulic radius ($R_h = A/P$, i.e. wetted area over wetted perimeter) and n is a roughness coefficient having different values for different types of channel wall roughness.

Our study neglects 3D effects, thus only a segment of the flow with width B is considered, without side walls. We assume that $B \gg y$. Thus, $A = By$, $P = B$, $R_h = y$ and $q = yv\,[m^2/s]$. Inserting (2.2) and (2.3) into (2.1) we arrive at the ordinary differential equation for the water surface $y(x)$

$$\left(1 - \frac{q^2}{g\, y^3}\right) \frac{dy}{dx} = i - q^2\, n^2\, y^{10/3}, \tag{2.4}$$

where the new notation $i = -dz/dx$ was introduced. Note that if the term on the right-hand side vanishes, the slope of the surface does not change. This flow rate is called the normal flow rate and is given by

$$q_n = \frac{i\, y^{10/3}}{n}. \tag{2.5}$$

On the other hand, if the term on the left-hand side vanishes, the slope of the surface becomes infinite. Let us rewrite this term as

$$1 - \frac{q^2}{g\, y^3} = 1 - \left(\frac{v}{\sqrt{gy}}\right)^2 = 1 - Fr^2. \tag{2.6}$$

The Froude number Fr is the ratio of the fluid and wave velocity and is analogous to the Mach number in gas dynamics. As $Fr \to 1$, $dy/dx \to \infty$, which is not possible. Indeed, with strongly curved water surface, the assumptions of straight streamlines and hydrostatic pressure variations are no longer valid. If $Fr < 1$, the flow is called subcritical while if $Fr > 1$, the flow is called supercritical.

The transition from subcritical to supercritical flow (or vice versa) cannot be computed by means of (2.4). Instead, let us apply the frictionless momentum equation, i.e.

$$\frac{v_1^2}{g} y_1 + \frac{y_1^2}{2} = \frac{v_2^2}{g} y_2 + \frac{y_2^2}{2}. \tag{2.7}$$

By making use of the continuity equation, it is easy to show that

$$\frac{y_2}{y_1} = \frac{1}{2}\left(\sqrt{1 + 8\, Fr_1^2} - 1\right). \tag{2.8}$$

Equation (2.8) gives the connection between the upstream and downstream velocities and water heights across a hydraulic jump, where subscript '1' refers to the upstream side and subscript '2' to the downstream side of the jump.

3. **CFD setup**

The commercial computational fluid dynamics code ANSYS CFX 10.0 was used for 2D steady-state numerical simulation. The set of equations solved by CFX 10.0 are the unsteady Reynolds-averaged Navier-Stokes equations in their conservation form, see [7] for details. An additional general transport equations is solved for each component's volume fraction. The total length of the bottom obstacle was $L = 0.355m$ (see Figure 1) and the computational domain stretched $3L$ length before and $10L$ after the obstacle. The height of the domain was $0.5m$. Two-dimensional structured mesh was created, with a thickness of $0.01m$ in the span-wise direction. Mesh sensitivity tests were performed with three different mesh densities on the same blocking structure and the middle one containing approx. 25k of cells was found to be adequate. (These results are not reported here; the difference in mass flow rate was below 1% for the middle and the finest mesh. The computational effort on the finest mesh was almost unbearable; a typical computation needed approx. 6 days on our 2.4 GHz PC with 1GB RAM.) Due to visibility reasons, a blow-up of the *coarsest* mesh close to the obstacle is shown in Figure 2. The actual (middle) mesh used in the computations contained four times denser mesh in the vertical direction and twice denser in the horizontal direction. The cell aspect ratio was between 0.025 and 0.9996, the skewness was between 0.646 and 1.000 and the maximal volume ratio was between 1.0004 and 4.9.

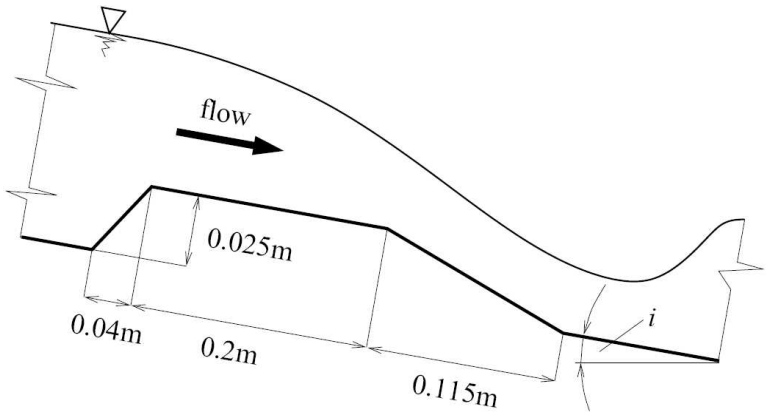

Figure 1. Geometry of the bottom obstacle

The inclination of the bottom was set to $i = 3 \times 10^{-4}$, which was taken into account by defining the appropriate components of the gravity force g_x and g_y. Water level boundary conditions were set on the upstream and downstream side being prescribed through hydrostatic pressure profiles. Rough wall with $0.5\,mm$ wall roughness was set for the channel bottom and opening boundary condition with uniform static pressure of $1\,bar$ was set for the upper boundary. High resolution spatial difference scheme was

applied and relatively small, $0.01\,s$ physical time step was prescribed. Note that as the wave velocity was typically $1.32\,m/s$ ($y_u = 0.18\,m$) and the overall length of the computational domain was $4.97\,m$, the characteristic time was $3.73\,s$. Yet numerical experiments showed that a maximal time step of $0.01\,s$ was needed for stable simulation, which resulted in a large number of iterations, typically between 5000 and 10000. The convergence was judged by means of mass flow rate balance at the inlet and outlet because it was found that during the computations, the usual convergence criteria for the residuals (typically, 10^{-5}) do not guarantee a mass balance error smaller than 0.1%. Homogenous multiphase model was used, which handles the two phases as a single mixture with different volume fractions. The surface tension, interphase mass transport and interphase forces were neglected. Standard $k-\epsilon$ turbulence model was adopted.

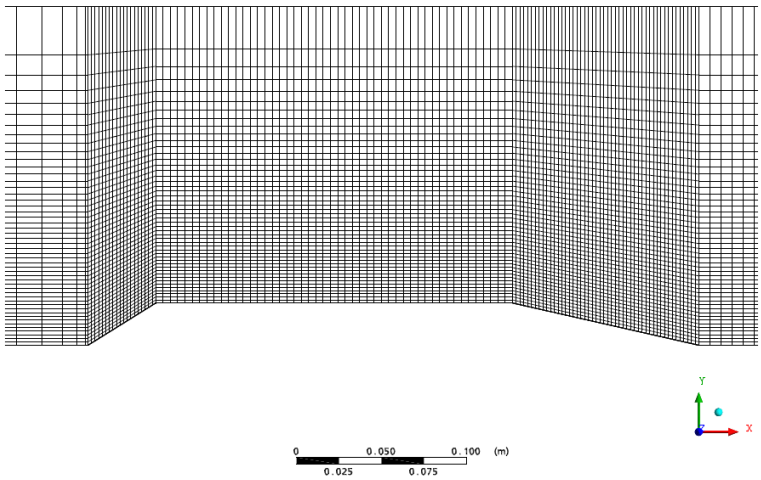

Figure 2. The coarsest computational mesh close to the obstacle, see text for details

4. **Overview of the results**

Table 1 gives a general overview of the simulations. The upstream water height was kept constant at $y_u = 0.18\,m$ while the downstream water height was decreased systematically, from $y_d = 0.18\,m$ to $y_d = 0.11\,m$. The water surface is defined as an isosurface with 50% volume fraction of water. The water surface shapes are depicted in Figure 3.

The very first simulation with the same upstream and downstream water level allows us to calculate the normal flow rate and thus to identify the wall roughness parameter n defined in (2.3), which was found to be $n = 0.0149$. Note that this value is consistent with the literature, e.g. for smooth metal flumes, cement mortar surfaces or unplaned plank flumes, [14] (p.435) gives $n = 0.011 \ldots 0.015$.

Table 1. Summary of the CFD runs. †: indicates that the undular jump stretched outside the computational domain. For all calculations $y_u = 0.18m$.

$y_d\,[m]$	$Q \times 10^3\,[m^3/s]$	$Fr_{max}\,[-]$	Comment
0.180	0.667	0.334	subcritical
0.175	1.104	0.630	subcritical
0.170	1.256	0.791	subcritical
0.160	≈1.410	≈0.958	unstable
0.155	1.402	1.076	undular jump
0.150	1.422	1.236	undular jump
0.145	1.429	1.415	undular jump
0.140	1.432	1.411	undular jump
0.130	1.463	1.402	undular jump †
0.120	1.487	1.395	undular jump †
0.110	1.529	1.349	undular jump †

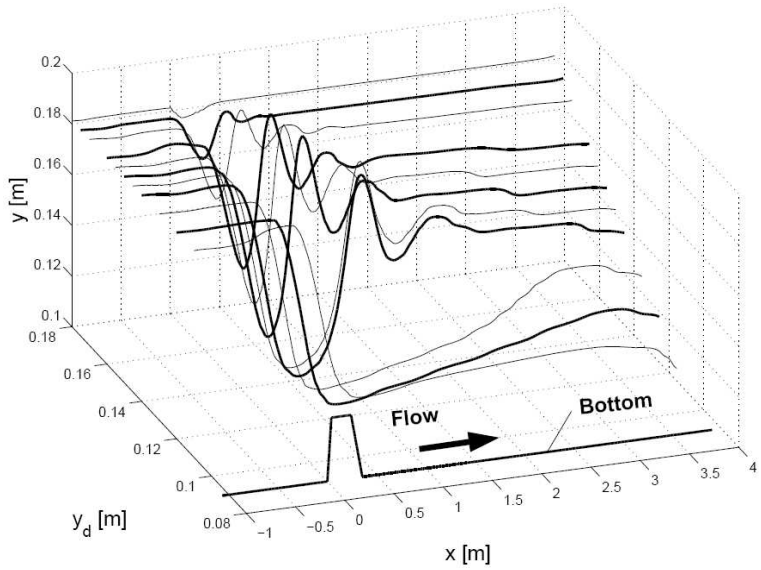

Figure 3. Fluid surface shapes for several downstream water heights (see Table 1 for the actual values). The different line widths are only for visibility reasons

As the downstream water level was decreased, the flow rate increased. Calculating the maximal Froude number along the channel shows that the subcritical/supercritical transition occurs at approx. $y_d = 0.16\,m$. Indeed, this calculation was unstable and only approximate values of flow rate and Froude number were obtained. (By

"unstable" a periodic oscillation with an amplitude of about 10% of the flow rate is meant. During the oscillation, the RMS value of the residuals was continuously below 10^{-5}.)

By decreasing the downstream water height below $0.16\,m$, the flow became supercritical. As it is known from the literature (e.g. [3]), for small Froude numbers of $1 < Fr < 1.7$, undular jumps are formed. In the last three simulations, the Froude number was between 1.4 and 1.35 yet no undular jumps were observed, which is probably due to the insufficient length of the computational domain in the downstream direction. This issue needs further study and the analysis of these results is not addressed in this paper, however for the sake of completeness, the main parameters of these runs and the corresponding surface shapes are also given.

5. **Analysis of the subsonic results**

In the case of subcritical flow (first three simulations in Table 1), the CFD results are compared to the surface predicted by the 1D model. The ordinary differential

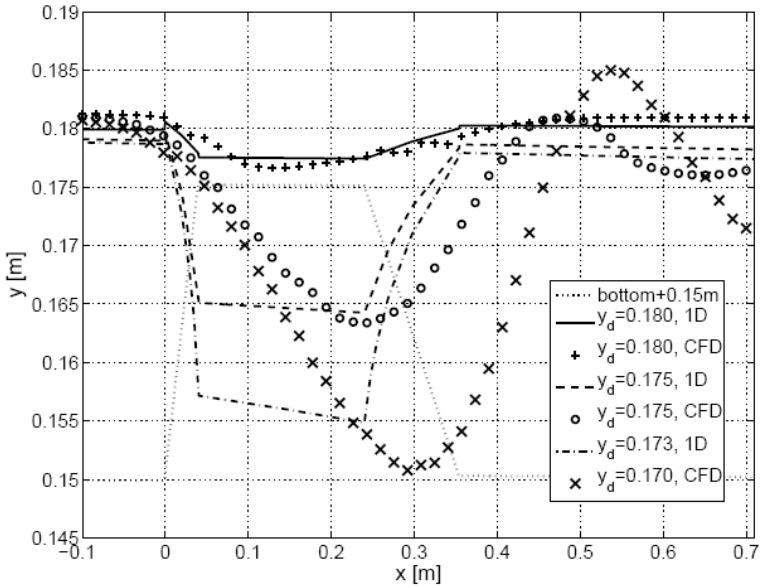

Figure 4. Subcritical computations, comparison of 1D model and CFD results. Note that for better visibility, the bottom obstacle was shifted by $0.15\,m$ in the y (vertical) direction

equation (2.4) together with the upstream and downstream water heights defines a boundary value problem with two boundary conditions and one free parameter, namely the flow rate. The problem was solved with Matlab's boundary value solver `bvp4c`. The roughness parameter n was kept constant (0.0149) during the calculations.

The 1D model predicts the subcritical/supercritical transition to $y_d \approx 0.172\,m$, thus the solution obtained with $y_d = 0.173\,m$ was plotted vs. the CFD result with $0.17\,m$. Note that the boundary value problem was solved on the same domain as the CFD calculations (total length of 14 times the obstacle length) but for better visibility, only the region close to the obstacle is presented in Figure 4.

As the flow rate increases (y_d decreases), an increasing difference between the 1D model and the CFD results is observed. The main reason for this increasing deviation is the increasing curvature of the streamlines and thus the loss of validity of the 1D assumptions (uniform flow profile, hydrostatic pressure distribution). It is also interesting that the 1D model predicts much sharper surfaces and the wavy contour after the obstacle is missed. This suggests that although (2.4) remains physically meaningful up to $Fr = 1$, it provides acceptable results only for a much narrower range of the Froude number, i.e. for flows with slightly curved surface.

6. **Analysis of the supercritical results**

For slightly supercritical flows with $1 < Fr_1 < 1.7$ undular jumps are formed, see e.g. [9] for details. The situation is sketched in Figure 5: the supersonic ($Fr_1 > 1$) upstream flow slows down to subsonic flow via a hydraulic jump. As the energy is not dissipated by rollers or regions of high turbulence intensity, the energy losses are radiated forward in a train of stationary waves. The most important parameters are the Froude number and the water height at the toe of the jump and at the first wave crest. According to the classic 1D theory, these values are connected by (2.8).

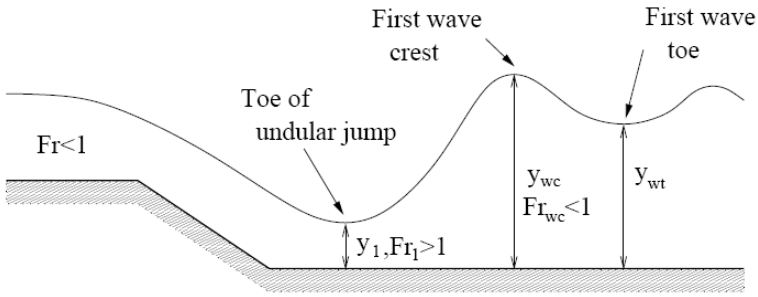

Figure 5. Parameters of the undular hydraulic jump

The experiments of Ohtsu et al. [8] are used as reference for validating the computations. Also, some preliminary measurements were performed on the recently built channel of the Dept. of Hydrodynamic Systems but as the experimental rig is not yet fully set up these results are only for rough checking. The authors in [8] give the following conditions for the classification of undular jumps (UJ): $1 \le Fr_1 \le Fr_{1limit}$ for breaking UJ and $Fr_{1limit} \le Fr_1 \le Fr_{1u}$ for nonbreaking UJ, where

$$Fr_{1limit} = 1.79 - 0.03\,(10 - B/y_1)^{1.35}\,, \tag{6.1}$$

$$Fr_{1u} = 2.10 - 0.03\,(12 - B/y_1)^{1.35}, \tag{6.2}$$

with $2 \leq B/y_1 \leq 10$ and $2 \leq B/y_1 \leq 12$ for (6.1) and (6.2), respectively. Here B is the channel width. As only 2D simulations were performed in this study, we use the largest value of the B/y_1 values, which gives $Fr_{1limit} = 1.78$ and $Fr_{1u} = 2.1$. Indeed, the largest Froude number (at the toe of the UJ) in the simulation was 1.457 and undular jumps were observed in the computations.

Let y_{wc} denote the height of the first wave crest and y_{wt} stand for the height of the first wave toe, see Figure 5. Than, according to [8], we have

$$\frac{y_{wc}}{y_1} = -0.76\,(Fr_1 - 1)^2 + 2.3\,(Fr_1 - 1) + 1, \tag{6.3}$$

$$\frac{y_{wt}}{y_1} = 0.90\,(Fr_1 - 1)^{2.5} + 0.2\,(Fr_1 - 1) + 1. \tag{6.4}$$

Table 2 presents the comparison between the CFD results, (2.8) (with $y_2 = y_{wc}$) and Ohtsu's formula (6.3) from [8]. The water heights at the first wave crest predicted by classic theory and those ones of CFD computations agree well. Note that as the energy dissipation in undular jumps is very low, classic analytical formula (2.8) is well applicable. From the CFD point of view, as wild recirculation zones with high turbulence intensity and air entrainment (e.g. rollers) are not present, turbulence modelling is not a primary issue and also as the interface of the two phases remain well-defined (no air entrainment or bubble formation), there is no need for inhomogeneous multiphase models. Ohtsu's formula slightly overpredicts the height but it should be emphasised that this formula has been developed for a much wider Froude number range.

Table 2. Undular hydraulic jump: comparison of classic theory, CFD results and Ohtsu's formula (6.3) in [8]

y_d $[m]$	y_1 $[m]$	Fr_1 $[-]$	Fr_{wc} $[-]$	y_{wc}/y_1, (2.8) $[-]$	y_{wc}/y_1, CFD $[-]$	y_{wc}/y_1, (6.3) $[-]$
0.155	0.1192	1.179	0.617	1.241	1.233	1.387
0.150	0.1091	1.310	0.631	1.419	1.412	1.640
0.145	0.1010	1.460	0.678	1.624	1.624	1.897
0.140	0.0970	1.457	0.684	1.620	1.690	1.892

Figures 6 and 7 provide a visual interpretation of Table 2. Starting with Figure 6, we conclude again that the CFD results show a satisfactory coincidence with the classic theory (2.8) while (6.3) gives slightly larger values. It is not clear for the authors why (6.3) is inconsistent with (2.8): at least for the $Fr_1 \to \infty$ limit (6.3) should tend asymptotically to (2.8). Due to the uncertainties in water level measurement, the experimental results are hard to judge. The error in the height measurement is estimated to be $3mm$, the velocity measurement (performed with metering orifice) is loaded with max. 1% error. This results in a relative error in Fr_1 between 2.7% and 5.7%, and 6.3 . . . 13.3% in y_{wc}/y_1 and y_{wt}/y_1.

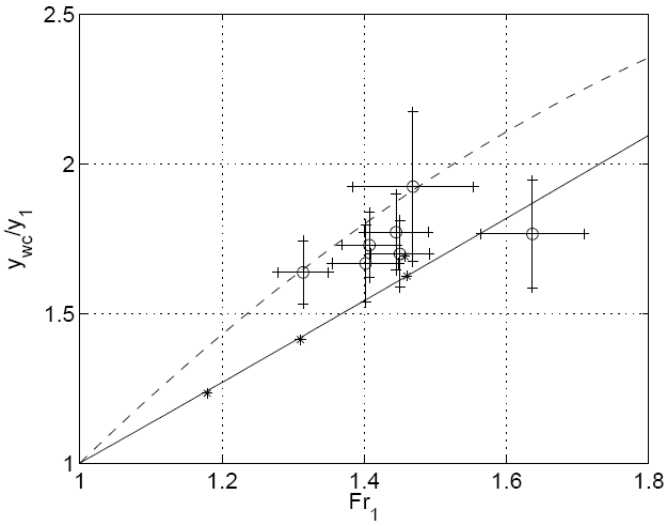

Figure 6. Dimensionless wave crest height vs. upstream Froude number. Circles denote measurement, asterisk stands for CFD results, the continuous line is (2.8) and dashed line is (6.3)

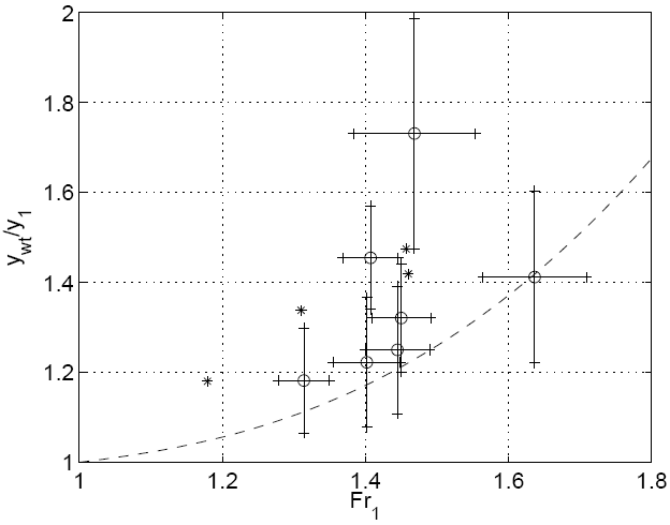

Figure 7. Dimensionless wave toe height vs. upstream Froude number. Circles denote measurement with error bars, asterisk stands for CFD results and the dashed line is (6.4)

The parameters of the first wave toe depicted in Figure 7 is again very hard to judge. On one hand, the measurements are close to Ohtsu's formula (6.4) apart from the two points of high w_{wt}/y_1. On the other hand, the measurements and Ohtsu's results do not coincide with the CFD results but it is not clear that if CFD predicts the first wave crest height properly, why would it miss the first wave toe. However, one should be aware that during the post-processing of the CFD results, another uncertainty is introduced: the extracted water heights depend on the volume fraction level through which the surface is defined (50% in this paper): by varying the volume fraction level (say, to 90%), the surface also changes. This issue needs further study and notably a systematic CFD study coupled with experiments.

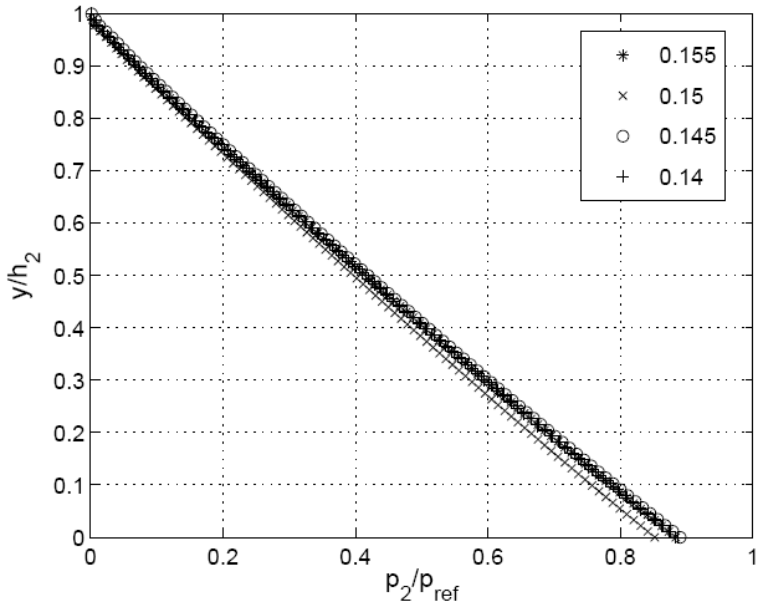

Figure 8. Dimensionless pressure distribution vs. dimensionless depth at the crest of the first wave. The parameters in the legend refer to y_d

Next, the pressure distributions are studied. Figures 8 and 9 depict the dimensionless pressure distributions across the depth at the toe of the jump and at the first wave crest. The reference pressure was set to $p_{ref} = \rho\, g\, y_{wc}$ and $p_{ref} = \rho\, g\, y_{wt}$ (respectively), i.e. the hydrostatic pressure according to the water height. The results are in good accordance with [4] and [15], especially the profiles beneath the first wave crest. Clearly, the pressure distribution is not hydrostatic beneath the undulations; the pressure gradients were larger when the free-surface was curved upwards (i.e. concave) and less than the hydrostatic gradient when the surface was convex. Note that no recirculation zones have been observed in these calculations. For the last two cases ($y_d = 0.145$ and $y_d = 0.14$) the hydrostatic pressure distribution was regained at the

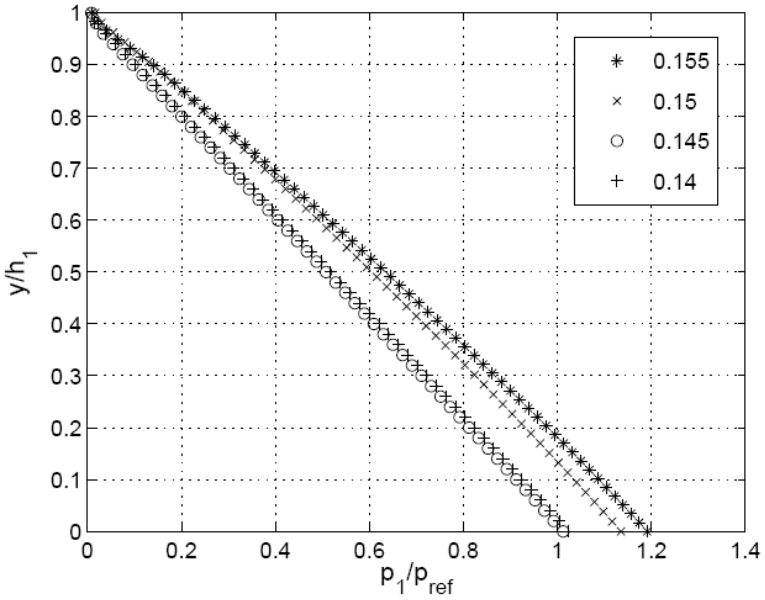

Figure 9. Dimensionless pressure distribution vs. dimensionless depth at the toe of the hydraulic jump. The parameters in the legend refer to y_d

toe of the jump, however, for $y_d = 0.155$ and $y_d = 0.15$ a higher pressure gradient has been observed. Figure 10 provides a visual interpretation of the highly curved streamlines in the undular hydraulic jump.

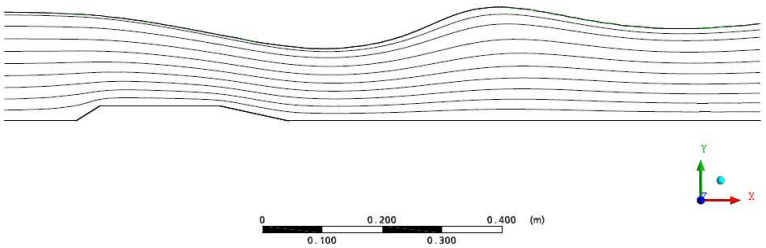

Figure 10. Streamlines beneath the undular jump, $y_d = 0.145m$

7. **Conclusion**

It was shown that commercial CFD codes offer the possibility of analysing free-surface flows without differentiating between or separately modelling subcritical, transcritical and supercritical cases. The price is the computational effort: one steady-state run

for the presented problem would require 10-15 hours of computation on a 2.4 GHz PC with 1GB RAM. Two-dimensional features of such flows were highlighted, notably non-hydrostatic pressure distribution. Weak hydraulic jumps (undular jumps) were studied; classic theory, recent experiment-based formulae, CFD results and experiments were compared. Although several questions have not yet been solved (e.g. why CFD and measurement do not coincide at the first wave toe) it is clear that commercial CFD codes - under careful supervision - are useful tools for analysing such problems. However, whether stronger jumps (larger Fr numbers) with wilder transition zones, air entrainment and unsteady phenomena can be analysed with such numerical techniques is an issue the authors whish to study in the future.

References

1. Fox, R.W. and McDonald, A.T.: *Introduction to Fluid Mechanics*. John Wiley & Sons, (1995), ISBN: 0-471-59274-9.
2. Halász, G., Kristóf, G. and Kullmann, L.: Flow in Pipe Systems, Műegyetem Kiadó, (2002), ISBN: 963-420-708-1 (in Hungarian).
3. Svendsen, IB.A., Veeramony, J., Bakunin, J. and Kirby, J.T.: The flow in weak turbulent hydraulic jumps, *Journal of Fluid Mechanics*, **418**, (2000), 25-57.
4. Chanson, H.: Boundary shear stress measurements in undular flows: Application to standing wave bed forms. *Water Resources Research*, **36**(10), (2000), 3063-3076.
5. Metcalf, B., Longo, J., Ghosh, S. and Stern, F.: Unsteady free-surface wave-induced boundary-layer separation for surface-piercing NACA-0024 foil: Towing tank experiments. *Journal of Fluids and Structures*, **22**, (2006), 77-98.
6. Rhee, S.H., and Stern, F.: RANS model for spilling breaking waves. *Journal of Fluids Engineering*, **124**, (2002), 424-432.
7. Ansys Inc.: CFX 10 Users' Manual, (2006).
8. Ohtsu, I., Yasuda, Y. and Gotoh, H.: Flow conditions of undular hydraulic jumps in horizontal rectangular channels. *Journal of Hydraulic Engineering*, **129**, (2003), 948-955.
9. Chanson, H.: Characteristics of undular hydraulic jumps: experimental apparatus and flow patterns. *Journal of Hydraulic Engineering*, **121**(2), (1995), 129-144.
10. Steinruck, H., Schneider, W. and Grillhfer, W.: A multiple scale analysis of the undular hydraulic jump in turbulent open channel flow. *Fluid Dynamics Research*, **33**, (2003), 41-55.
11. Zeruhin, Y.T. and Fenton, J.D.: One-dimensional simulation model for steady transcritical free surface flows at short length transitions. *Advances in Water Resources*, **29**, (2006), 1598-1607.
12. Birman, A. and Falcvitz, J.: Application of the GRP scheme to open channel flows. *Journal of Computational Physics*, (2006), doi:10.1016/j.jcp.2006.07.008.
13. Crossley, A.J., Wright, N.G. and Whitlow, C.D.: Local time stepping for modelling open channel flows. *Journal of Hydraulic Engineering*, (2003), doi:10.1061/(ASCE)0733-9429 (2003)129:6(455).

14. Daugherty, R.L., Franzini, J.B. and Finnemore E.J.: *Fluid Mechanics with Engineering Applications*. McGraw-Hill Book Company, Singapore, (1989), ISBN:0-07-100405-X.

15. Chanson, H.: Physical modelling of the flow field in an undular tidal bore. *Journal of Hydraulic Research*, **43**(3), (2005), 234-244.

Journal of Computational and Applied Mechanics, Vol. 8., No. 1., (2007), pp. 71–83

NUMERICAL INVESTIGATION OF ROTOR-STATOR INTERACTIONS IN A 1.5-STAGE LOW-SPEED AXIAL COMPRESSOR

Huixia Jia, Konrad Vogeler, Lutz Müller, Ronald Mailach
School of Energy and Power Engineering, Xi'an Jiaotong University
Xi'an, Shaanxi Province, 710049, China
anniejia@mailst.xjtu.edu.cn

[Received: January 15, 2007]

Abstract. The relative motion of rotor and stator leads to viscous and inviscid interactions between the blade rows. This is the reason why the flow in turbomachines is periodically unsteady. The unsteady flow field of the first stage with inlet guide vane row (IGV) of the Dresden Low-Speed Research Compressor ($LSRC$) is investigated using a 3D time-accurate, viscous solver. The unsteady profile pressure distribution on the pressure side (PS) and the suction side (SS) of the rotor at midspan (MS) for the design point are presented and analysed. A comparison to experiments performed at the same compressor is drawn [1, 2]. The pressure fluctuation on the rotor depends on the superimposed effect of the wakes of the inlet guide vane and the potential effect of the downstream stator. The time-resolved pressure in the simulation changes nearly simultaneously along the whole chord length like as also observed in the experiment. A phase shift between the pressure fluctuations on the PS and the SS is found. Furthermore the unsteady blade pressure forces of the rotor blades are calculated from the profile pressure distribution at midspan. The results are compared with the experimental results.

Keywords: axial compressor, rotor-stator-interaction, periodic unsteady blade pressure fluctuation, unsteady blade pressure force

Nomenclature

A	$[m^2]$	area of blade surface
c_F	[-]	pressure force coefficient
c_M	[-]	moment coefficient
F	$[N]$	pressure force
f	$[Hz]$	frequency
K	[-]	number of time steps
l	$[m]$	chord length
M	$[Nm]$	moment
N	[-]	number of time steps
p	$[Pa]$	static pressure
t	$[s]$	time

w	$[m/s]$	relative velocity
x	$[m]$	chordwise position
y	$[m]$	position perpendicular to chord
γ	$[deg]$	angle between resulting force and normal direction
ρ	$[kg/m^3]$	density

Subscripts and superscripts

$\bar{}$	time-averaged values
∞	average of the velocity vectors of the incoming and outgoing flow
$-$	fluctuating part
$<>$	ensemble-averaged value
1	measuring plane upstream of the rotor blade row
cg	centre of gravity
cl	centre of lift
dyn	dynamic
i, j	indices for time traces
x	component in blade chord direction
y	component perpendicular to the blade chord

Abbreviations

BPF	blade passing frequency
IGV	inlet guide vane
$LSRC$	Low-Speed Research Compressor
MS	midspan
PS	pressure side
RMS	Root Mean Square Value
SS	suction side

1. Introduction

The flow in turbomachinery is inherently unsteady because of the relative motion between stationary and rotating blade rows. The relative motion between rotor and stator blades induces unsteady aerodynamic interactions which lead to a periodic fluctuation of the profile pressures. The resulting unsteady blade forces have a significant influence on the fatigue behaviour of the blades. Therefore it is necessary to gain a better understanding of the unsteady interaction mechanisms in turbomachines.

Early investigations on rotor-stator interaction were carried out by Kemp et al. [3]. They analysed the unsteady pressure response and the excitation of the unsteady forces theoretically. Within recent years several experimental investigations and numerical simulations on this topic were carried out. Hsu and Wo [4] experimentally investigated the unsteady blade row interaction in a large-scale low-speed 1.5-stage axial compressor. Lee and Feng [5] studied the same compressor numerically. Dorney et al. [6, 7] investigated the clocking effect on unsteady force in an axial compressor

and a turbine. The pressure fluctuations and the unsteady force changes on the blades were considered for the operating points with maximum and minimum efficiency. Li and He [8] numerically investigated the effect of different stator blade numbers on the unsteady blade loading on the rotor blades and stator blades in a 1.5-stage transonic turbine. Marconcini and Pacciani [9] simulated the effects of clocking on efficiency and unsteady forces in a 1.5-stage high-pressure turbine.

In this paper, the numerical investigation is carried out with the geometry of the Dresden $LSRC$. The pressure fluctuation and the unsteady blade loading on rotor blades of the first stage are presented and compared with the experimental results from Mailach et al [1, 2].

2. **Numerical method**

The Dresden $LSRC$ consists of 4 repeating stages which are preceded by an inlet guide vane row. The blading of the compressor was developed from a typical middle stage of a high pressure compressor of a gas turbine. A detailed description of the Dresden $LSRC$ is given in [10-12].

In this paper, the unsteady flow field of the first stage with IGV of the Dresden $LSRC$ is numerically investigated. The calculations were carried out at MS for design conditions of the compressor.

The $3D$ time-accurate, viscous flow solver $FINE^{TM}/Turbo$ for a compressible ideal gas was used for these investigations. The Baldwin-Lomax algebraic vortex-viscosity model is employed to solve the turbulent flow field. The spatial discretization of the Reynolds-averaged Navier-Stokes equations is based on a cell-centered control volume scheme. The control equations are advanced by a time-marching scheme using an explicit 4-stage Runge-Kutta method. Local time stepping, implicit residual smoothing and multigrids are used to accelerate the computational convergence. A dual time stepping method is used to carry out the unsteady simulation.

The blade number of the IGV, the rotor and the stator blade rows in the experiment are 51, 63 and 83, respectively. In the calculation, the blade number is scaled to 42 inlet guide vanes, 63 rotor blades and 84 stator blades in order to make a compromise between a reasonable precision of the simulation and the cost of the computational time. Thus, with the scaled blade numbers only 2 passages of the IGV, 3 passages of the rotor and 4 passages of the stator have to be simulated in the computational domain.

The complete mesh and the details of the meshes at the leading edge and at the trailing edge of the rotor are shown in Figure 1. To resolve the flow field near the blades O-type grids are used. H-grids are used to resolve the flow field in the blade passages. The total number of grid points is $348,825$.

As boundary conditions at the inlet, the stagnation parameters and the flow angle are specified. At the outlet, the pitch-wise mean static pressure is defined. The shroud and hub walls are treated as Euler-wall. The sliding mesh method is employed at the rotor/stator interface. Using this method, the grid of the rotor is rotated in function

of the physical time step and the rotor turning speed. Then the flow field is resolved at the given physical time step. In one simulation period, 90 physical time steps are simulated. One simulation period is the time that one rotor passes two IGV's.

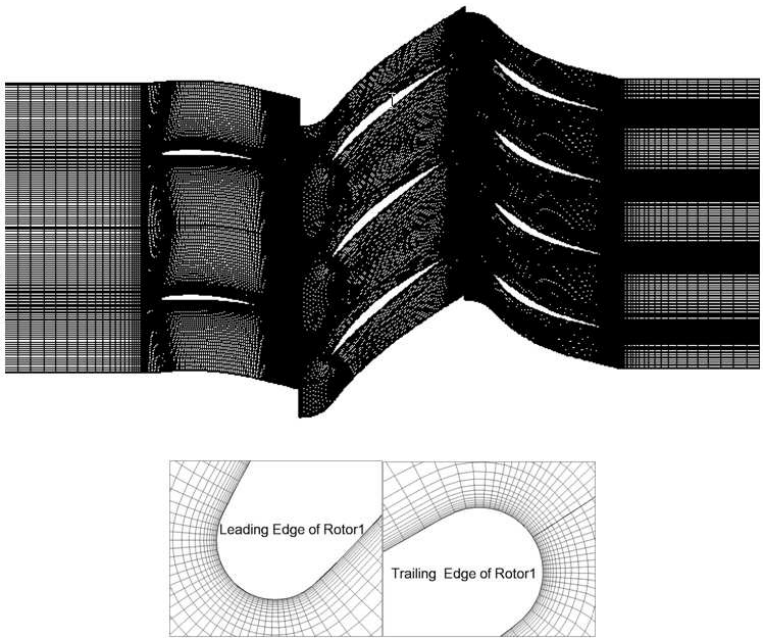

Figure 1. Computational mesh

3. Time-averaged pressure distribution on the rotor blades

Figure 2 shows the steady distribution of the pressure coefficient for the design condition on the rotor blade at MS. The agreement of the results of the simulation with the experimental data is satisfactory.

It can be observed in Fig. 2 that the flow accelerates to 15% chord on the SS. At 15% chord, the pressure minimum is reached. After the pressure minimum, the flow begins to decelerate towards the blade trailing edge. On the PS the flow accelerates to 8% chord where the pressure is minimal. Then the flow decelerates to 80% chord. From 80% chord towards the trailing edge the flow accelerates slightly.

4. Unsteady pressure distribution on the rotor blades

In Figure 3 the time-averaged pressure distribution is given as solid lines for the calculation (Figure 3a) and the experiment (Figure 3b). The pressure coefficient is calculated from the time-averaged values of the unsteady simulation.

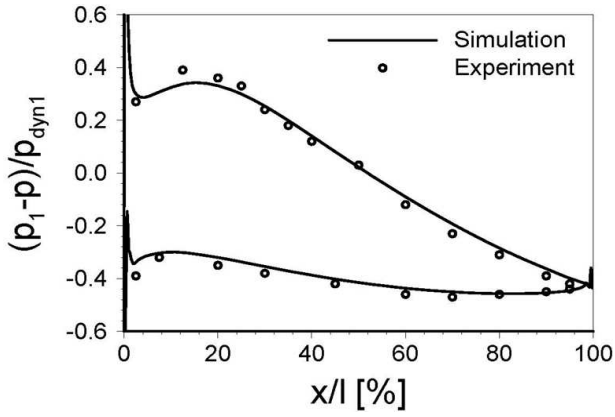

Figure 2. Steady pressure distribution, rotor 1, MS, design point

The time-averaged Root Mean Square-value (RMS) is calculated as following

$$\overline{RMS} = \sqrt{\frac{1}{N}\sum_{i=0}^{N-1}\left[p_i\left(t\right) - \overline{p}\right]^2} \tag{4.1}$$

which represents information about periodic fluctuation in the simulation. In the experiment, it includes both periodic and stochastic pressure fluctuations.

In Fig. 3 the fluctuations around the time-averaged pressure distributions are shown as dashed lines. It can be seen, that the fluctuations in the experiment are somewhat stronger than that in the simulation. This can also be observed in the space-time-diagrams of the unsteady pressure distribution on the rotor, shown later in this section.

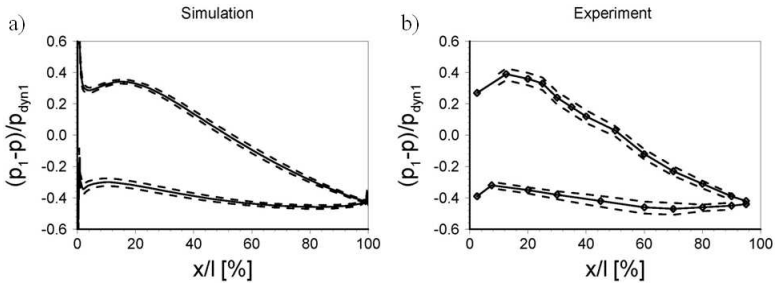

Figure 3. Steady pressure distribution with RMS-values, rotor 1, MS, design point

In the simulation, the relative position of the IGV and the stator in every IGV passage is identical, because the stator blade number is twice the blade number of the IGV (42 IGV's and 84 stator blades).

In the experimental setup, the blade numbers of IGV (51) and stator (83) are not multiples. So the relative configuration between the IGV and the stator in every passage is different.

Therefore the experimental data are considered at a circumferential position of the compressor, where a comparable relative position of IGV and stator blades can be found like in the simulation.

Figure 4a and 4c shows the numerical results for this configuration, whereas the experimental results are shown in Figure 4b and 4d. The time is related to the passing time of the downstream stator tstator. In each case the fluctuating part of the profile pressures is shown. The experimental results are ensemble-averaged using a once-per-revolution signal. This was done with the equation

$$< p\,(t) >= \frac{1}{K} \sum_{j=0}^{K-1} p_j\,(t) \tag{4.2}$$

It can be observed, that the unsteady profile pressure fluctuation is influenced by the superimposed effect of the IGV wake and the potential effect of the downstream stator. For both, the simulation and the experiment, on the PS and the SS the pressure changes nearly instantaneously in time along the chordwise direction.

The unsteady profile pressure fluctuation in the simulation appears periodically. In every second stator passing period the pressure fluctuation repeats since the blade number of the stator is twice the IGV number. In the experiments 2 blade passing periods of the stator corresponds to 1.23 periods of the IGV.

If the pressure fluctuation induced by the IGV and the pressure fluctuation due to the downstream stator potential field are superimposed, the pressure fluctuation is intensified (Fig. 4a). This appears at every second blade passing period of the stator. When t/tstator is equal to 1.2 and 3.2, the unsteady pressure fluctuation is intensified on the PS of the rotor. When t/t_{stator} is equal to 0.2 and 2.2, the pressure fluctuation due to the downstream stator is superimposed with a pressure fluctuation of the IGV wake with the opposite sign. As a result the resulting pressure fluctuation is reduced.

The same situation can be observed in the experiment (Fig. 4b). If t/t_{stator} is 1.3 and 3.2, respectively, the unsteady pressure amplitude on the PS of the rotor blade reaches a maximum. At $t/t_{stator} = 2.2$ the unsteady pressure amplitude is clearly smaller.

The largest pressure fluctuations on the PS appear between the leading edge and 50% chord. In the simulation the maximum pressure fluctuation amplitude is $+/-5\%$ of the dynamic head of the incoming flow. Compared to the experimental results, the maximum pressure fluctuations of the simulation are somewhat lower than that from the experiments.

Also on the SS the superposition of the IGV wakes and the potential field of the stator leads to a modulation of the resulting pressure fluctuation amplitudes (Fig. 4c). So the pressure amplitudes at $t/t_{stator} = 0.6$ and 2.6 are somewhat higher than at $t/t_{stator} = 1.6$ and 3.6.

The experimental results on the SS show a comparable pressure distribution concerning the fundamental pattern and the pressure amplitudes (Fig. 4d). However, the increase of the pressure amplitudes for every second passing stator blade does not appear since the ratio of stator blade to IGV number is not equal to two.

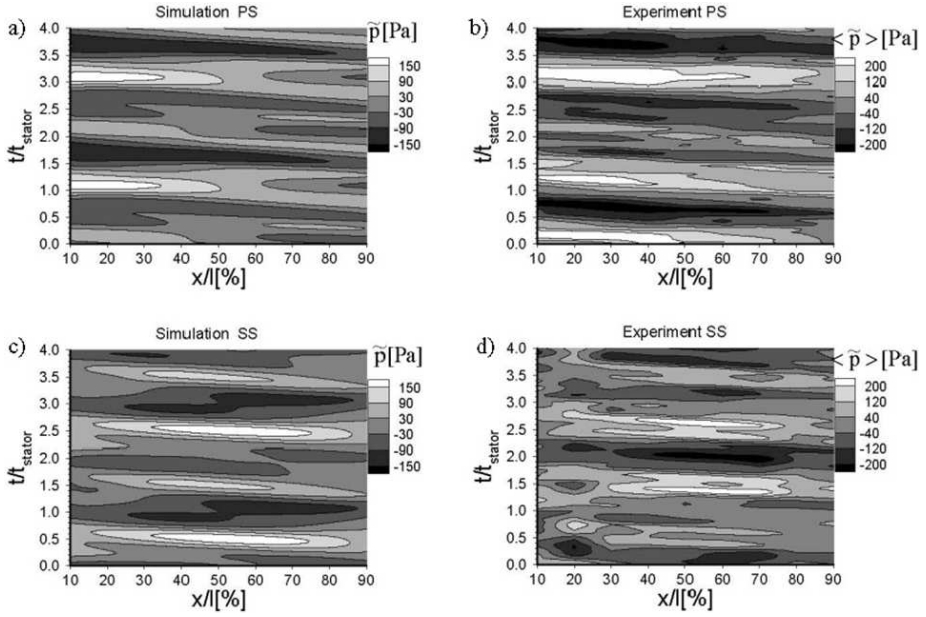

Figure 4. Unsteady pressure distribution on PS and SS of rotor1, MS, design point

On the SS, the largest pressure fluctuations appear in the range of $20-80\%$ chord (Figs. 4c and 4d). In this area the flow decelerates. Similarly, the maximum pressure fluctuations on the PS appear in the region with decelerated flow (from $10-50\%$ chord, Figs. 4a and 4b).

It can be stated, that a good qualitative consistency of the experiment and the simulation exists. Differences can arise from the fact, that the unsteady pressure fluctuations on rotor 1 are also affected by the potential fields of the stators of the subsequent compressor stages, which are not considered in the simulation. Furthermore the neglected spanwise pressure distribution as well as the not modelled radial gaps of the rotor blades leads to differences between simulation and experiment.

As part of the data of Fig. 4, in Figure 5 the fluctuating part of the profile pressures at the 50% chord positions on PS and SS are presented. Figure 5a shows the time

traces of the pressure fluctuation on PS and SS as a result of the calculation. The timescale is again normalised with the passing period of the downstream stator. The 4 passing periods of the downstream stator corresponds to 2 passing periods of the IGV. The pressure fluctuations are caused by the superimposed effect of the IGV wakes and the potential effect of the downstream stator blades. Because of the given blade count ratio the characteristic pattern of pressure fluctuations repeat periodically in every second passing periods of the downstream stator. Between the signals on PS and SS a constant phase shift between the pressure fluctuations on PS and SS of about 180 degrees can be observed.

The corresponding experimental data show more spiky fluctuations with larger amplitudes. The phase shift between the signals on PS and SS is changing in time between $90 - 180$ degrees, depending on the relative position of the IGV wakes and the stator potential effects [1]. This changing phase shift appears because the stator blade number for the experiment is not a multiple of the IGV number.

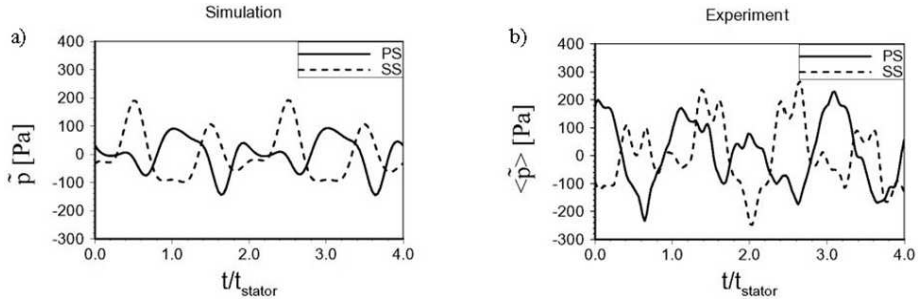

Figure 5. Pressure fluctuations at 50% chord of the rotor blades at MS, design point

In Figures 6a and 6b the frequency spectra of the pressure at the 50% chord position on the PS of the rotor are given for the simulation and the experiment. The design rotational speed of the compressor is 1000 revolutions per minute. In the simulation, the blade passing frequencies (BPF) of the IGV and the stator are $700Hz$ and $1400Hz$, respectively (42 IGV and 84 stator blades). In the experiment the 1. BPF of IGV is $850Hz$ and $1383Hz$ for the stator (51 IGV and 83 stator blades).

In the simulation the dominant periodic influence of the IGV wakes is reflected by the 1. BPF of the IGV. The 2. BPF of the IGV corresponds to the 1. BPF of the stator blades. Thus for this frequency component the stator potential effect cannot be distinguished from the IGV wake effect. However, in Fig. 4 the dominance of the potential effect of the stator blades versus the IGV wake effect is obvious. According to that, it can be assumed, that the main contribution to the peak at $1.4kHz$ stems from the potential field of the downstream stator.

This is also confirmed by the experimental data (Fig. 6b). The amplitude of the potential effect of the downstream stator is about two times of the wake effect of the

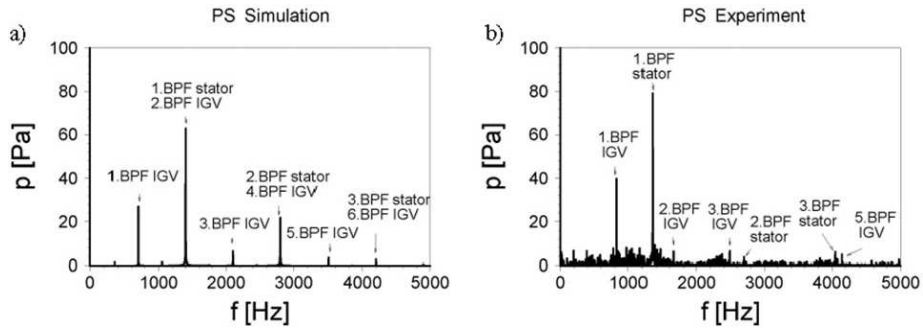

Figure 6. Frequency spectra of pressure on the rotor blades, 50% chord, design point

IGV (1. *BPF*'s of *IGV* and stator blades). The higher harmonics of the *BPF*'s of the blade rows can be neglected.

In the numerical results the amplitude at the 1. *BPF* of the *IGV* is only 43% of that appearing at the 1. *BPF* of the stator (Fig. 6a). This is the same order of magnitude than observed in the experimental results. At $2.8kHz$ the pressure amplitude from the simulation is considerably higher than in the experiment. This is due to the superimposed effects of the 2. *BPF* of the stator and the 4. *BPF* of the *IGV*. Other higher harmonics of stator and *IGV BPF*'s are of less importance for the blade excitation.

On the *SS* (no figure) comparable observations can be made like described for the *PS*. That means, the amplitude due to the potential effect of the downstream stator (1. *BPF* stator) is largest and the effect of the *IGV* wake (1. *BPF IGV*) amounts to about 50% of the potential effect of the downstream stator (1. *BPF* stator).

5. **Unsteady pressure force on the rotor blades**

Due to the unsteady profile pressure distribution an unsteady blade pressure force and unsteady moment are generated. The unsteady aerodynamic blade loading significantly influences the blade life cycle. In this section, the unsteady blade pressure forces at *MS* on the rotor blade in the first stage for the design condition will be discussed. The algorithm used here to calculate the unsteady force is described by Mailach et al. [2].

Figure 7 shows the force component definitions in the blade coordinate system. The components of the force F are denoted as F_x and F_y. These components are directed along the blade chord direction and perpendicular to that, respectively. The moment M_{cg} acts around the centre of gravity of the blade.

The unsteady pressure force in the experiment is calculated from the pressure distribution, which is measured with piezoresistive pressure transducers [1]. These sensors are arranged at *MS* on *PS* and *SS* each from 10% chord to 90% chord with

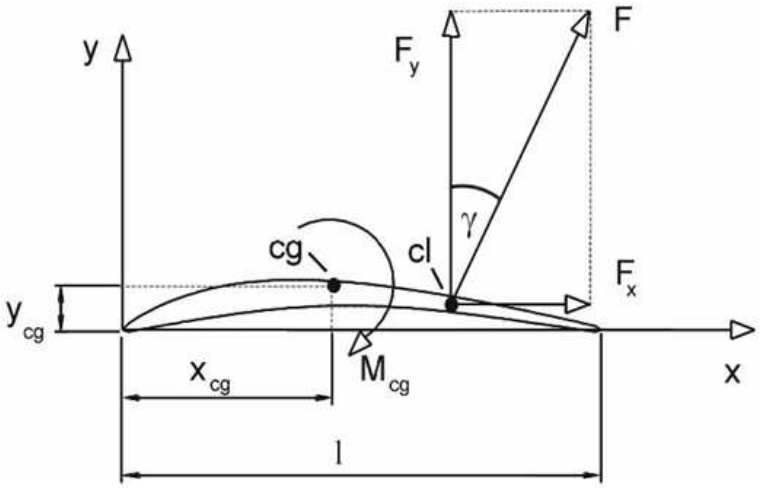

Figure 7. Forces in blade coordinate system

an equal spacing of 10% chord. At the leading edge and the trailing edge no pressure transducers could be mounted. In the experiment the time traces of the pressure at the leading edge and the trailing edge are extrapolated from the transducers mounted at 10% and 90%, respectively.

In the simulation, the force is calculated from the unsteady profile pressure distribution along the whole chord of the rotor blades at MS, including the leading edge and the trailing edge regions.

Because the pressure force is related to the up- and downstream flow field, the force coefficient is calculated with the following relation

$$c_F(t) = \frac{F(t)}{\rho/2 \cdot \overline{w}_\infty^2 \cdot A} \tag{5.1}$$

while the nondimensional moment is calculated with

$$c_{m,cg}(t) = \frac{M_{cg}(t)}{\rho/2 \cdot \overline{w}_\infty^2 \cdot A \cdot l} \tag{5.2}$$

In Table 1 the time-averaged pressure force coefficient c_F on the rotor, its components $c_{F,x}$ along blade chord direction (x) and $c_{F,y}$ in the perpendicular direction to the blade chord (y) as well as the moment around the center of gravity are given. A good agreement of these time-averaged quantities from the simulation and the experiment is evident. The dominating force component is F_y. Its mean value is about 10 times of F_x. Thus, the force coefficient c_F is nearly equal to the force component coefficient in y direction. Time-resolved values from the force calculation are shown in Figure 8. These are the force coefficient, the moment around the centre of gravity and the angle between F_y and F.

Table 2. Time-averaged pressure force coefficients of the rotor blade for design point

Rotor 1	$\overline{c}_F$	$\overline{c}_{F,y}$	$\overline{c}_{F,x}$	$\overline{c}_{M,cg}$	$\overline{\gamma}$ [deg]
Simulation	0.566	0.563	-0.05	0.56	-5.2
Experiment	0.55	0.55	-0.06	0.65	-6.7

As already observed for the unsteady profile pressure distribution, the *IGV* wakes and the potential effects of the downstream stator blades are the dominating periodic influences.

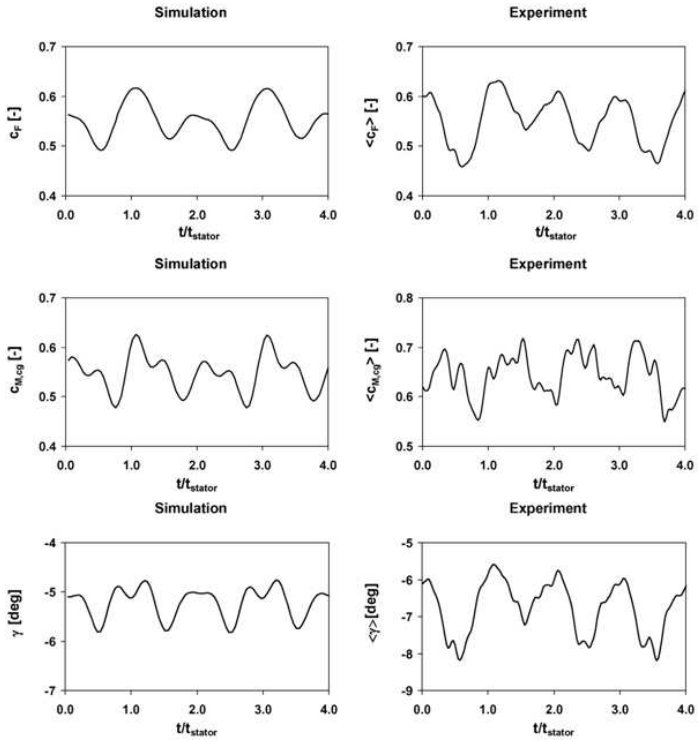

Figure 8. Unsteady pressure force coefficients, momentum coefficient and angle γ on rotor blades, design point

In the simulation the maximum fluctuation amplitude of the force coefficient c_F is $+/-12\%$ of the averaged values. Because of the lower values of $c_{F,x}$, the maximum fluctuation amplitude of the force coefficient $c_{F,y}$ is also $+/-12\%$ of the averaged values (no figure). The maximum fluctuation amplitude of the force coefficient in x-direction ($c_{F,x}$) is $+/-8\%$ of the mean values. The maximum fluctuation amplitude

of the moment around the centre of gravity is $+/-14\%$ of the mean values. The fluctuation of the angle γ between c_F and $c_{F,x}$ is only $+/-0.5$ degrees.

Somewhat larger fluctuation amplitudes of the force parameters are observed in the experiments. As reported in [2], the maximum fluctuation amplitudes of the force coefficient are $+/-15\%$ of its mean values for the experiment. The fluctuation of the angle γ between c_F and $c_{F,x}$ is about $+/-1.0$ degrees in the experiment. However, the time-resolved force parameters from the simulation and the experiment show a comparably good agreement. The experimental results are more noisy because the limited spatial resolution and the missing sensors at the leading and trailing edge of the blade.

The frequency spectrum of the force coefficient from the simulation is shown in Figure 9. As already observed for the pressure fluctuation on PS and SS, the potential flow field effect from stator 1 is the dominating periodic influence. In the frequency spectrum of the force the amplitude of the IGV wake effect is 50% of the potential effect of the downstream stator. The distribution of the peaks in the force spectrum is comparable to that of the pressure spectrum (Fig. 6a).

6. **Summary**

The unsteady flow field of a 1.5-stage configuration of the Dresden Low-Speed Research Compressor is investigated using a $3D$ time-accurate, viscous solver. The numerical results are analysed and compared with the experiments at midspan.

The unsteady profile pressure distributions on PS and SS of the rotor blades in the first stage are presented for the design conditions. The profile pressures are periodically affected by the IGV wakes and the potential effect of the downstream stator blades. The potential effect of the downstream stator dominates the pressure fluctuation. The wakes of the IGV play only a secondary role because of the comparably small velocity deficit of the IGV wakes. The maximum pressure fluctuation is about $+/-5\%$ of the dynamic head of the incoming flow. There is a phase shift of the pressure signals on PS and SS, which amounts to about 180 degrees.

The unsteady blade pressure force parameters of the rotor blades are calculated from the profile pressure distribution. The time traces and frequency contents of the pressure forces are also presented. The mean value of the force coefficient in y-direction is 10-times of that in x-direction. The maximum fluctuation amplitude of the force coefficient c_F is $+/-12\%$ of the mean values.

A detailed comparison of the results from the simulation and the experiments showed a good agreement of both time-averaged and time-resolved flow quantities.

Acknowledgement. The lead author would like to express her appreciation to the DAAD (German Academic Exchange Service) for the scholarship, provided for her stay at the TU Dresden. The experimental data are from the project: "Unsteady Forces and Boundary Layer Behaviour on the Blades of a Low-Speed Research Compressor" which also was performed at the TU Dresden and funded by the DFG (German Research Society).

References

1. Mailach, R. and Vogeler, K.: Rotor-Stator Interactions in a Four-stage Low-speed Axial Compressor - Part I: Unsteady Profile Pressures and the Effect of Clocking. *ASME Journal of Turbomachinery*, 126, (2004), 507-518.
2. Mailach, R., Müller, L. and Vogeler, K.: URotor-Stator Interactions in a Four-stage Low-speed Axial Compressor - Part II: Unsteady Aerodynamic Forces of Rotor and Stator Blades. *ASME Journal of Turbomachinery*, **126**, (2004), 519-526.
3. Kemp, R.H., Hirschberg, M.H. and Morgan, W.C.: Theoretial and Experimental Analysis of the Reduction of Rotor Blade Vibration in Turbomachinery through the Use of Modified Stator Vane Spacing, NACA, Technical Note 4373, (1958).
4. Hsu, S.T. and Wo, A.M.: Reduction of Unsteady Blade Loading by Beneficial Use of Vortical and Potential Disturbances in an Axial Compressor With Rotor Clocking, ASME Journal of Turbomachinery, 120, (1998), 705-713.
5. Lee, Y. and Feng, J.: Potential and Viscous Interactions for a Multi-Blade-Row Compressor. *ASME Journal of Turbomachinery*, **126**, (2004), 464-472.
6. Dorney, D.J., Sondak, D.L., Cizmas, P.G.A., Saren, V.E. and Savin, N.M.: Full-Annulus Simulations of Airfoil Clocking in a 1-1/2 Stage Axial Compressor. *International Journal of Turbo and Jet Engines*, **16**, (1999), 149-160.
7. Dorney, D.J., Croft, R.R., Sondak, D.L. and Stang, U.E.: Computational Study of Clocking in an Embedded Stage in a 4-Stage Industrial Turbine, ASME 2001-GT-0509.
8. Li, H.D. and He, L.: Blade Count and Clocking Effects on Three-Bladerow Interaction in a Transonic Turbine. *ASME Journal of Turbomachinery*, **125**, (2003), 632-640.
9. Marconcini, M. and Pacciani, R.: Numerical Investigation of Wake-Shock Interactions and Clocking in a Transonic HP Turbine, ASME GT2003-38401.
10. Sauer, H., Bernstein, W., Bernhard, H., Biesinger, T., Boos, P. and Möckel, H.: Konstruktion, Fertigung und Aufbau eines Verdichterprüfstandes und Aufnahme des Versuchsbetriebes an einem Nieder-geschwindigkeits-Axialverdichter in Dresden, Abschlußbericht zum BMBF-Vorhaben 0326758A, Dresden, Germany, (1996).
11. Müller, R., Mailach, R. and Lehmann, I.: The Design and Construction of a Four-Stage Low-Speed Research Compressor, Proceedings of the IMP 97 Conference on Modelling and Design in Fluid-Flow Machinery, Gdansk, Poland, (1997), pp. 523-530.
12. Boos, P., Möckel, H., Henne, J.M., and Selmeier, R.: Flow Measurement in a Multistage Large Scale Low Speed Axial Flow Research Compressor, ASME 98-GT-432.

Journal of Computational and Applied Mechanics, Vol. 8., No. 1., (2007), pp. 85–100

ANALYSIS OF SPRAY EVOLUTION IN INTERNAL COMBUSTION ENGINES USING NUMERICAL SIMULATION

András Kadocsa, Reinhard Tatschl, Gergely Kristóf
Department of Fluid Mechanics Faculty of Mechanical Engineering, Budapest University of Technology and Economics
H-1111 Budapest, Bertalan L. u. 4-6, Hungary
kadocsa@ara.bme.hu

[Received: January 29, 2007]

Abstract. Numerical simulation is a widely used research tool in internal combustion related research. This paper summarizes results of research on a new approach of spray formation calculations. Using a primary breakup model for separately describing the initial liquid disintegration of injected liquid based on the flow properties stemming from a previous calculation of injector nozzle flow gives a better predicting capability and is able to suit the new needs of advanced combustion systems such as HCCI engines or various forms of split injection. The child breakup mechanism provides the necessary droplet surface for evaporation in the vicinity of nozzle, but it causes bimodality in the size spectrum, hence there is an unrealistic factor behind seemingly good agreement of calculation results and measurement data. The new homogenous distribution child production model proposed here is aimed at reducing this effect, and providing a more even size distribution while retaining good agreement with measurement data in other aspects of examination.

Keywords: Diesel injection, numerical simulation, primary breakup, child droplet size distribution

Nomenclature

C_i	[-]	breakup model constants
C_μ	[-]	standard $k-\varepsilon$ turbulence model constant ($C_\mu = 0.09$)
D	$[m]$	droplet diameter
SMD	$[m]$	Sauter Mean Diameter
$\mathrm{Re} = \dfrac{u\rho_l D}{\mu_l}$	[-]	Reynolds number
T	[-]	Taylor parameter
$We_g = \dfrac{u^2\rho_g D}{\sigma}$	[-]	Weber number defined with ambient gas density
$We_l = \dfrac{u^2\rho_l D}{\sigma}$	[-]	Weber number defined with injected liquid density
a	$[m]$	stable droplet radius
k	$[m^2/s^2]$	turbulent kinetic energy
r	$[m]$	actual droplet radius

r_c	$[m]$	child droplet radius
t	$[s]$	time
u	$[m/s]$	relative velocity
z	[-]	non-dimensional radius
ε	$[m^2/s^3]$	turbulent dissipation rate
τ	$[s]$	characteristic breakup time
Λ	$[m]$	wavelength of fastest growing surface wave
Ω	$[1/s]$	growth rate of fastest growing surface wave
μ_l	$[kg/ms]$	dynamic viscosity of injected liquid
ρ_g	$[kg/m^3]$	gas density at ambient pressure
ρ_l	$[kg/m^3]$	density of injected liquid
σ	$[N/m]$	characteristic breakup time

1. **Introduction**

Numerical simulation has played an important role in engine development for two decades. As the models applied developed, and the increase in computational performance created the opportunity to include larger domains and more detailed modeling approaches, it became an acknowledged research tool as well. Numerical simulation has played an important role in engine development for two decades. As the models applied developed, and the increase in computational performance created the opportunity to include larger domains and more detailed modeling approaches, it became an acknowledged research tool as well.

The accuracy of prediction of mixture formation is of great importance concerning the subsequent combustion processes, and thus it influences the ability of numerical simulation to predict e.g. pollutant emission. With the increased attention on environmental aspects of internal combustion engines, the simulation of spray formation gained on increased importance, and became an area of intensive development. The changing requirements represented by advanced injection systems – e.g. spilt injection or $HCCI$ engines – resulted in a need for rethinking the conception of spray formation simulation, and providing a new approach to fulfill these requirements.

Since measurement technology provides due to its limitation concerning time and length scales and because of its outstandingly high cost demand only a limited opportunity to investigate the very small time and length scales characteristic to direct fuel injection, numerical simulation plays an important role in engine related research as well.

The new approach of using a separate primary breakup model to better simulate the initial phase of liquid breakup represents an answer to the newly arising needs of internal combustion engine research and development. The new model used throughout the simulations of this paper is implemented in a specialized commercial CFD code [1], and is used for diesel engine injection simulations. The calculations presented here and the new method for predicting child droplet production were realized in the framework of a research project aiming at gaining experience about the combination

and interaction of models, to identify areas for improvement and to propose or realize new ideas aiming at better prediction capability.

2. **Breakup of fluids**

Fluid columns break up into ligaments or droplets, and these latter break up into further droplets according to different, simultaneously acting mechanisms, depending on a number of physical characteristics. The first process is generally referred to as *primary breakup* and the latter process is called *secondary breakup* [2, 3, 4]. Based on their characteristic physical processes, these basic breakup regimes can be differentiated, and they are treated in literature usually separately.

In both basic breakup regimes a number of different breakup types appear. These breakup types can be characterized by various properties of spray. The most important quantity summarizing the influential factors concerning the intensity and type of breakup is the Weber number, calculated with droplet (or nozzle orifice) diameter, and either with ambient gas or injected liquid density, and is referred to as We_g and We_l respectively. The type of Weber number to be used depends on the aim of investigation, but both dimensionless parameters describe the same phenomenon, only from another perspective.

Another important quantity is the Reynolds number, defined in spray literature in general [5, 6] with density and viscosity values referring to injected liquid.

The third important quantity representing the effect of viscosity and surface tension in the context of spray breakup is the Ohnesorge number as defined in equation (1)

$$Oh = \frac{\sqrt{We_l}}{\mathrm{Re}} = \frac{\mu_l}{\sqrt{\sigma D \rho_l}} \tag{1}$$

Based on these quantities, there are a number of classification methods for describing the regimes of initial liquid disintegration, i.e. primary breakup. A classification is given by Schneider [7] based on the works of Lefebvre [5] and Reitz [8], as depicted in Fig. 1.

In general it can be stated that the higher the Weber number, the more intensive the breakup is, thus ranging from Rayleigh type of breakup (*Zone A*) through first (*Zone B*) and second (*Zone C*) wind-induced breakup to atomization (*Zone D*). In case of our investigations the general Weber number far exceeds the highest limit of regime switch, therefore the breakup process is characterized by properties of the regime "atomization" [9].

The subsequent breakup of ligaments and droplets, i.e. secondary breakup can also be classified according to Weber number, as depicted in Fig. 2. It ranges from bag breakup through bag and stamen type of breakup to boundary layer stripping and catastrophic breakup, with increasing Weber number. For diesel conditions boundary layer stripping, capillary wave detachment (Kelvin-Helmholtz instability) and catastrophic breakup by Rayleigh-Taylor waves are typical [10].

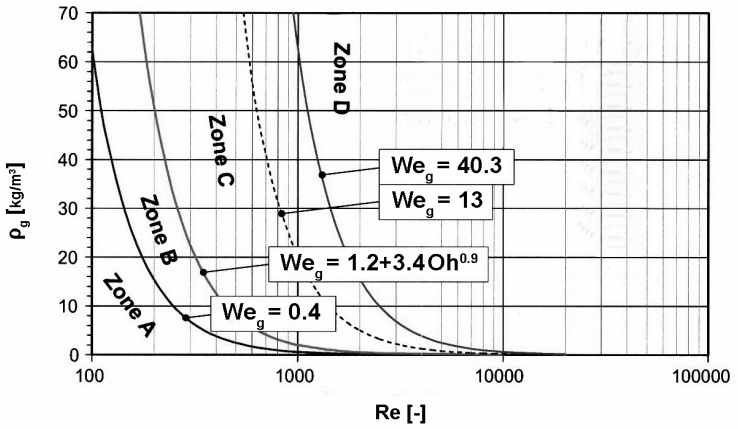

Figure 1. Primary breakup zones as a function of Reynolds number and ambient gas density [7]

The most important factor influencing primary breakup – as agreed by most of recent literature – is the character of the fluid flow leaving the injector orifice [12, 13], being injection pressure [14], L/D ration [13] and shape of injection nozzle bore [15] the most decisive aspects. Secondary breakup is most influenced by properties of injected liquid – mostly viscosity [16, 17] – and by ration of liquid and gas density [18, 19].

3. **Modeling spray formation**

To appropriately model spray formation, a number of physical processes must be taken into consideration. For most of these processes a separate sub-model accounts for. Besides breakup such processes are evaporation, droplet drag and collision and coalescence of droplets [1]. All these processes are covered in the calculations presented here by separate, generally accepted models, however the emphasis of this research is put on primary and secondary breakup, therefore other mechanisms are not discussed here in detail.

Modeling of liquid breakup has been developed significantly in the past two decades, however most of these models adapted the approaches generally used in simulations. A good example on this is that droplets are generally tracked in a Lagrangian way in a gas flow field, which latter is treated by conservation equations for mass, momentum and energy as well as turbulence in an Eulerian frame of reference.

Another general framework is represented by the *Discrete Droplet Model* (DDM) [20]. Since the typical number of droplets arising during a high pressure diesel injection is in the order of magnitude of 10^6-10^8, the registration and tracking of each and every individual droplet is not practical and not even necessary. Therefore, in the DDM

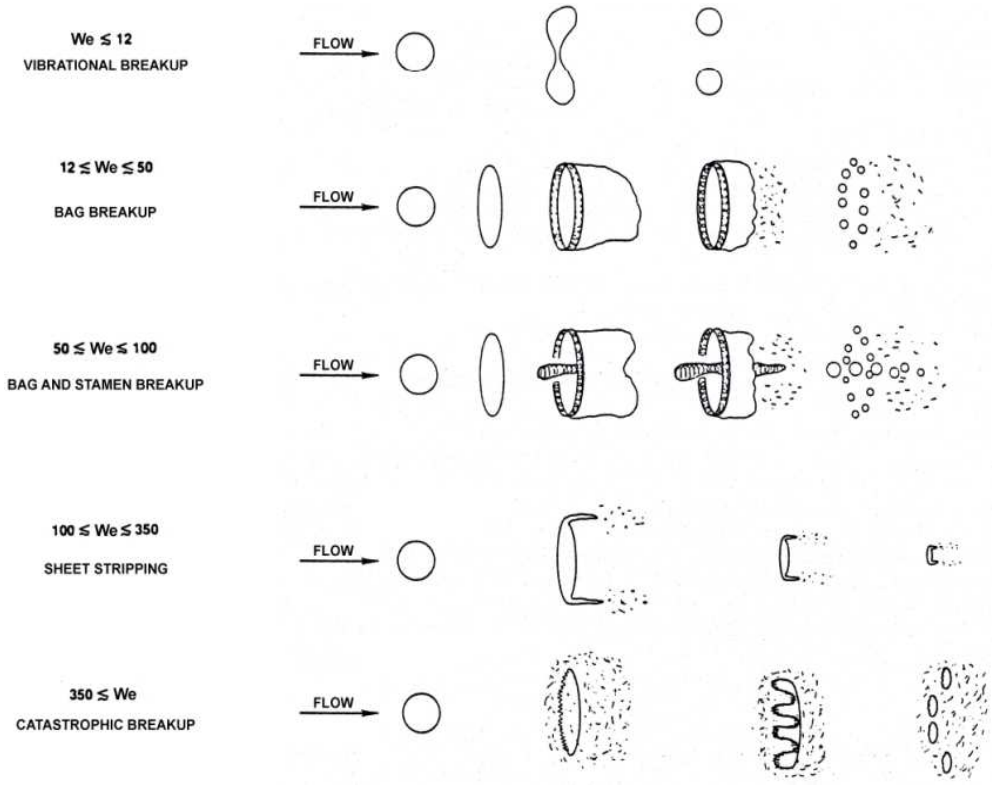

Figure 2. Secondary breakup zones as a functionof Weber number [11]

approach the droplets are collected into parcels, and they have uniform properties (diameter, velocity, temperature etc.) within one parcel. A parcel behaves like one drop with the additional information on the number of identical droplets represented. Hence, the calculation is not necessary to be performed for every single droplet, however, the diversity of droplets is still well represented by choosing an appropriate number of parcels (typically in the order of 10^4).

The calculation of the parcel movement is done with a subcycling procedure between the gas phase time steps taking into account the forces exerted on droplets in the parcels by the gas phase as well as the related heat and mass transfer. In an analogous way the gas phase receives the forces resulted from spray movement as source terms in the next gas time step.

A further approach that is used by most of the prevalent models is the *rate approach* [6]. As it is described by equation (2), it grabs the phenomenon of breakup through

the velocity of loss of droplet radius, providing a widely used approach of breakup.

$$\frac{dr}{dt} = -\frac{r-a}{\tau} \tag{2}$$

The submodels for breakup used in most of CFD codes all aim at determining the value of stable radius a and characteristic breakup time τ determining the breakup rate, and they mostly use all the above mentioned approaches as framework for operation. The advancement is thus usually achieved through creating new models for determining the stable radius a and characteristic breakup time τ.

One of the earliest attempts for this was the *Taylor Analogy Breakup* (TAB) model [21], which is based on the analogy between an oscillating and distorting droplet and a spring-mass system. The external force is represented by the aerodynamic forces acting on the droplet, the spring force is related to the surface tension, and the damping force corresponds to the force due to liquid viscosity. Hence, as a reaction on the aerodynamic forces, the droplet starts to oscillate. As soon as the amplitude of this oscillation reached a predefined level, the droplet disintegrates, i.e. breakup occurs.

A similar idea, based also on the elliptic deformation of the droplet is reflected in the *Dynamic Droplet Breakup* (DDB) model, which tracks the motion of the mass centers of the half droplets [22]. It is essentially a nonlinear formulation of the TAB model equations, and the time consuming numerical integration seems not to have been offset by the increase in accuracy, since the model has not found wide acceptance [23].

The most commonly used single secondary breakup model was developed by Reitz [6] and is called $Wave$. This model is used for simulation of secondary breakup in calculations of this paper, therefore its working principles are described here in more detail.

This model relates breakup to the Kelvin-Helmholtz instability, as depicted in Figure 3.

The growth of an initial perturbation of a liquid surface is linked to liquid Reynolds number as well as gas Weber number and other physical and dynamic parameters (e.g. viscosity) of the injected fuel and the domain fluid. The stable radius is linked to the wavelength of the fastest growing surface wave according to equation (3) [6].

$$a = C_1 \Lambda \tag{3}$$

where Λ represents the wavelength of fastest growing surface wave, and is defined in equation (4).

$$\Lambda = 9.02r\frac{(1+0.45Oh^{0.5})(1+0.4T^{0.7})}{(1+0.87We_g^{1.67})^{0.6}} \tag{4}$$

whereas

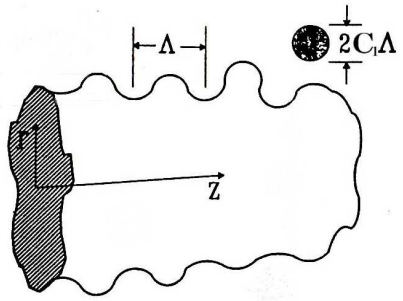

Figure 3. The Wave model relates breakup to Kelvin-Helmholtz instability and product droplet size is proportional to surface wave length [6]

$$T = Oh\sqrt{We_g} \tag{5}$$

The breakup time is calculated with a number of factors as defined in equation (6)

$$\tau = C_2 \frac{3.726r}{\Lambda\Omega} \tag{6}$$

where Ω represents the growth rate of fastest growing surface wave, and is defined in equation (7),

$$\Omega = \left(\frac{\rho_l r^3}{\sigma}\right)^{-0.5} \frac{0.34 + 0.38We_g^{1.5}}{(1+Oh)\,(1+1.4T^{0.6})} \tag{7}$$

and C_1 and C_2 are model constants.

When exposed to certain conditions (e.g. high relative ambient gas velocities), and the actual radius is larger than the stable radius under the circumstances considered, the droplets of a parcel start "losing" diameter as prescribed by equation (2). In basic case, the mass shed from these droplets in each subcycle is used to update the diameter of drops. This is done by calculating the new drop diameter from the rate of equation (2) according to the local conditions for stable diameter a and breakup time τ. Based on the updated radius the total mass is converted into an increased number of droplets of identical diameter (within the same parcel). Hence, the mass in a parcel is always conserved (not considering evaporation, or child droplet production as described later), only the number of droplets contained is changing according to droplet diameter.

Since the droplets lose diameter always only in proportion to the time passed since the last spray time step, the model does not deliver enough small droplets near the nozzle. Therefore, a so called child production mechanism was inserted into Wave [6].

The basic idea of child production mechanism is that a certain proportion of the shed mass immediately receives the stable diameter, i.e. they do not "approach" it incrementally according to the rate approach of equation (2). Since the basic idea of the *DDM* method is that a parcel contains droplets of identical properties, the droplets created in the framework of the child droplet mechanism, referred to as child droplets, are placed in a newly created parcel. The diameter of these child droplets is in most cases much lower than the value reached by the parent droplets (the droplets from which the child droplets were created) in the same timeframe, which provides the necessary additional droplet surface for evaporation already in the vicinity of the injection nozzle.

The above mentioned models have been used – and are still widely used – to predict the entire spray breakup process. However, a disadvantage of all these models if used alone is that certain initial properties of the spray have to be provided by the user, or have to be assumed by the model based on practical or theoretical considerations. Such initial circumstances include the spray angle and droplet diameter at the nozzle orifice and the transition from a continuum liquid column to droplets that can subsequently be handled by secondary breakup models discussed above.

The use of an appropriate separate primary breakup model enables the prediction of these initial quantities. The basic prerequisite necessary for this is to have information about the injector flow properties, which are regarded to play a key role in early spray properties, such as spray angle. *Diesel Breakup model*, the primary breakup model used throughout this research uses a so called *nozzle file* for this purpose [1].

The nozzle file is created in advance in a separate, 3 dimensional, time dependent multi-phase simulation of the flow in the injector nozzle, so at the beginning of the spray calculation all relevant data on the nozzle flow is available time and spatially resolved into the nozzle file. The subsequent, separate spray calculation uses this data source as an input for the breakup mechanism. Hence, all droplets initialized by the primary breakup model consider the properties of injected liquid, as calculated in the previous simulation. The use of an independent simulation and a separate nozzle file enables e.g. various combustion chamber geometries to be simulated using the same nozzle file without the need for repeating the injector nozzle calculation for each case.

According to this approach the injected liquid is already tracked in the injector nozzle (this information is contained in the nozzle file). After leaving the injector nozzle it is treated by the primary breakup model, and after reaching certain predefined conditions (e.g. a predefined Weber number) the droplets are handed over to the secondary breakup model. All these droplets are treated by the secondary breakup model, until a final stable diameter is reached, and no more breakups occur.

In the vicinity of the nozzle – where primary breakup occurs and hence the primary breakup model should be used – two different mechanisms result in breakup. One of them is a consequence of turbulence of the flow of liquid, while the other one is related to the aerodynamic forces acting on the droplet, as in case of secondary breakup. There is no general agreement in literature which of these mechanisms dominates primary breakup, and it also depends on the topical circumstances of spray formation

considered. Therefore, a basic idea of Diesel Breakup model is to let these mechanisms compete in case of every breakup. Hence, for each parcel equation (2) is calculated by means of both mechanisms, and the mechanism giving a higher breakup rate will govern breakup.

The aerodynamic mechanism is accounted for by the $Wave$ model, just as in case of secondary breakup throughout this research. Turbulent breakup is calculated from turbulence values of injected liquid (contained in the nozzle file), according to equations (8) and (9).

$$a = C_3 C_\mu^{0.75} \frac{k^{1.5}}{\varepsilon} \tag{8}$$

$$\tau = C_4 C_\mu \frac{k}{\varepsilon} \tag{9}$$

4. **Background of calculation**

The investigations reported have been accomplished using the $FIRE$ software ($v8.3-8.4$), a CFD code developed by AVL List[1], specialized on internal combustion engine related numerical simulation [1]. The parameters of the spray formation process to be simulated were chosen based on the data available for validation. The measurement data used throughout this research were received from Toyota Central Research and Development Laboratories and Doshisha Universtiy, and they were widely used in the wider context of the works presented here. The basic settings of all calculations are as displayed in Table 1.

Table 2. Characteristics of calculation

Injection time	$2ms$
Total simulated time	$8ms$
Length of time step	$0.01ms$
Maximum number of iterations per time step	100
Nozzle bore diameter	$0.14mm$
Nozzle bore length	$0.8mm$
Injected liquid	$Hexadecane$
Injection pressure	$87.5MPa$
Total volume injected	$1.01316e-8m^3$
Ambient gas	CO_2
Ambient gas pressure	$2.1e+6Pa$
Ambient gas temperature	$293K$

The computational domain models a simple, box shaped environment, but the general order of magnitude of cell sizes takes into consideration the usual characteristics

[1] AVL List is world's largest privately owned engine developer, located in Graz, Austria.

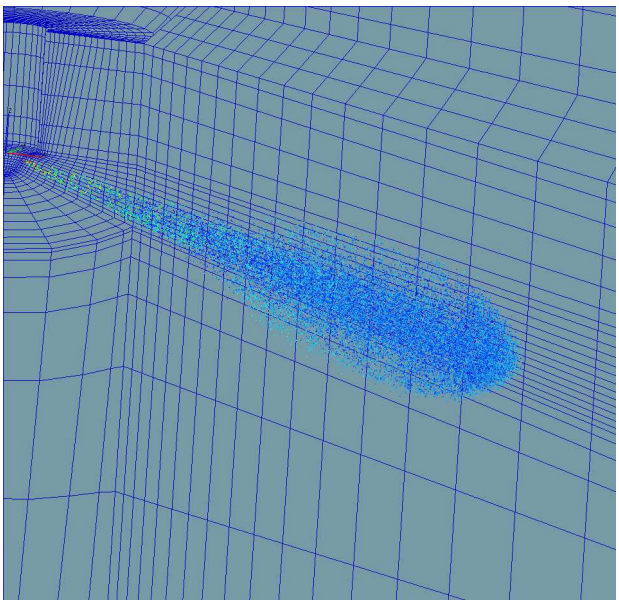

Figure 4. The cell structure in the vertical cut through the injection axis

of numerical grids for the purpose of internal combustion engine calculations. However, the structure of grid considers the expected pattern of flow field, determined mainly by the evolving spray cone. The injector nozzle is placed symmetrically in the middle of the box modeled.

The numerical model consists entirely of hexahedron cells, and it has total dimensions of $0.4 \times 0.2 \times 0.12m$. The structure is considerably compressed towards the injector orifice, and has long cells further away from the nozzle. These cells are, however, directed in the expected main flow direction, as depicted in Figure 4. (The spray displayed along with the cut through view of the grid represents a status of $2ms$ after start of injection, and the color data corresponds to the diameter of droplets, while the size of displayed droplets is chosen to be constant for better visibility.) The total number of cells is $45,144$.

There is a wall type boundary condition on all boundaries of the model applied, with a prescribed temperature of $300K$, however, the droplets are not expected to reach any of these boundaries in the time window of the calculation.

5. **The new model applied**

The aim of the child mechanism introduced by Reitz [6] for the *Wave* model was to provide sufficiently small droplets in the vicinity of injector nozzle to meet evaporation behavior characteristic to real life spray processes. An average of these child

droplets and the significantly larger parent droplets can deliver a reasonable agreement with measured SMD values. However, this procedure delivers by nature a markedly bimodal spectrum in droplet size distribution.

Since Diesel Breakup model is responsible for breakup of liquid in the vicinity of nozzle, it also includes child production mechanism. In case of this model, an attempt has already been made to reduce the shortcoming of the child production procedure used in secondary breakup. A Chi-square distribution of probable child droplet sizes was assumed, and a random number is used on the ordinate of the cumulative distribution diagram to get the appropriate diameter of child droplets via the inverse function on the diameter coordinate axis. However, the size distribution still tends to show bimodality.

A main aim of the current research is to develop an altered approach for child production both in secondary and primary breakup to reduce bimodality of size distribution. Calculations have been performed to optimize model parameters based on measurement data. As a result of these investigations good agreement in spray penetration and average SMD value could be obtained. However, size distributions of these calculations were characterized by significant bimodality. Since the available measurement data showed that bimodality of droplet size spectrum is fully absent, effort has been made to decrease this undesired effect of child droplet production mechanism.

To reduce bimodality, a linear distribution of child droplet sizes is assumed between the lower limit of stable droplet radius a respectively the upper limit taken as parent droplet radius r of the considered parcel. This approach assumes a constant value of the probability density function for the child droplet size between the lower and an upper limiting value. For the mathematical formulation a non-dimensional radius z is introduced, as displayed in equation (10).

$$z = \frac{r_c}{a} \tag{10}$$

According to earlier investigations, child production mechanism plays a more pronounced role in case of primary breakup, therefore the new idea for child production was first implemented in Diesel Breakup model. To avoid confusing effects, child production for secondary breakup was switched off in all calculations.

The cumulative probability density function using this value is defined in equation (11).

$$F(z) = \begin{cases} 0 & for \;\; z \leq 1 \\ \dfrac{a\,(z-1)}{(r-a)} & for \;\; 1 < z < \dfrac{r}{a} \\ 1 & for \;\; \dfrac{r}{a} \leq z \end{cases} \tag{11}$$

The implementation in the $FIRE$ code uses a random number chosen on the ordinate of the cumulative distribution diagram to get the appropriate diameter via the

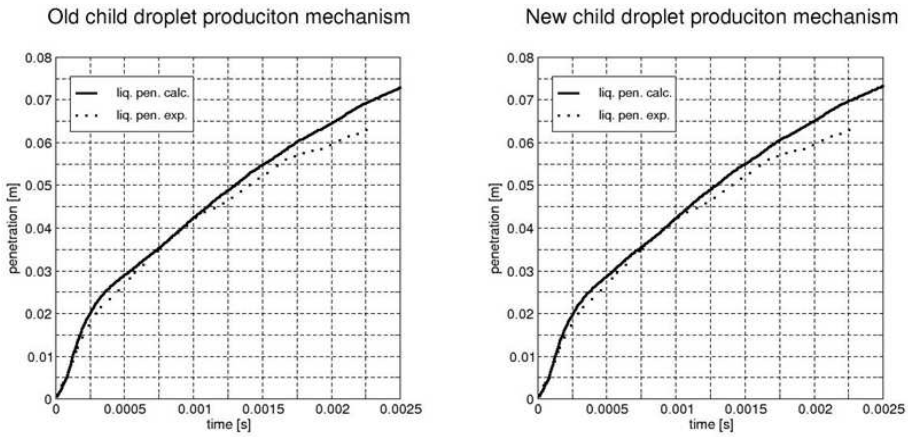

Figure 5. Penetration curves without and with use of the new primary breakup child production mechanism

inverse function on the non-dimensional diameter coordinate axis. This value is assigned to the child parcel under consideration. The use of random numbers provides a representation of the entire size distribution applied.

6. **Results**

A pair of sample calculations is presented here to introduce the effect of the new child production mechanism implemented. In these calculations the proportion of mass put into child parcels from the entire shed mass and the frequency of child parcel introduction was set high, in order to see the effects of the model change more pronounced. Due to the same considerations the C_4 program parameter belonging to the characteristic breakup time τ of Diesel Breakup model was set high to cause slow parent droplet breakup, and hence set stable diameter to a low value (if parent breakup is slow parent drops retain their size and hence their speed in a greater extent).

In one of the calculations the standard (Chi-square type of) child production mechanism, in the other calculation the new child production mechanism was used.

The penetration curves were barely affected by this change, and both gave a good agreement with measurement data, as depicted in Figure 5.

The changes were expected to be perceived in case of size distributions. This property is very rarely investigated in similar simulations, therefore comparison with literature data is not possible, however results are good interpretable without comparison as well.

For visualization of this a set of three curves was introduced. The first curve is the number weighted distribution, which is the covering curve of the bars representing the

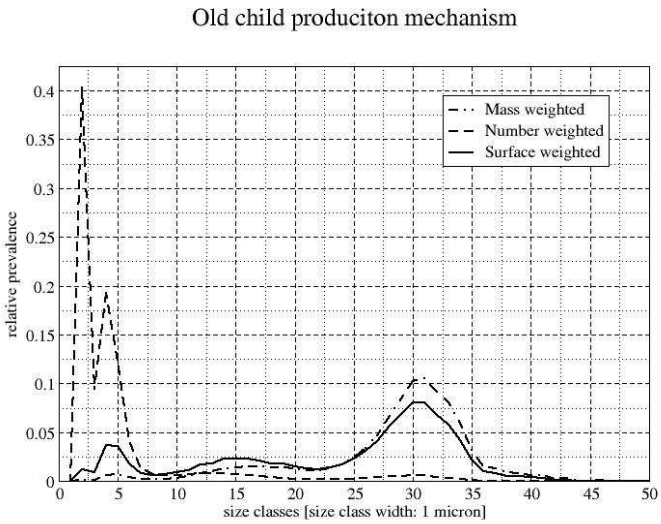

Figure 6. Size distributions with use of the conventional child production mechanism

relative prevalence of size classes, each 1 *micron* wide (e.g. representing the proportion of droplets with diameter between 3 and 4 *microns* related to the entire droplet population). The second curve is the surface area weighted distribution. It covers the bars representing the contribution of each of these 1 *micron* size classes to the cumulative surface of the entire droplet population. The third curve (mass weighted distribution) covers the bars representing the contribution of these size classes to the cumulative mass of the entire droplet population.

The most important indicator with respect to mixture formation is the surface weighted size distribution, since this is in closest relation to the expected evaporation behavior. On the other hand, bimodality appears on this curve most pronounced, since a large number of small droplets can "elevate" the left part of the curve. The size distribution without using the new child production model looks as depicted in Figure 6.

A pronounced bimodality is observable in this case with two peaks of surface weighted size distributions at $4-5$ *micron* and 30 *micron* respectively. It means that although the targeted average sauter mean diameter of 23.2 *micron* of measurements is reached in good agreement (calculation results showed 23.9 *micron*), this is obtained through an artificial duality of a large number of very small droplets, and a group of droplets representing large mass with higher than the target diameter.

If the new child production model is switched on, the size distribution changes significantly, as depicted in Figure 7.

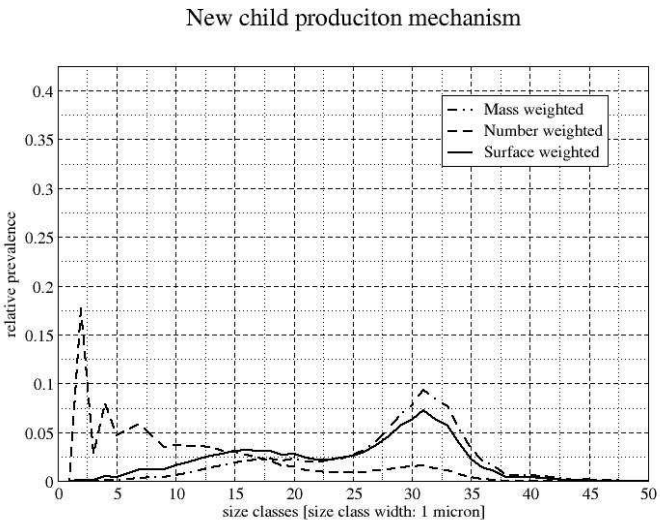

Figure 7. Size distributions with use of the new primary breakup child production mechanism

It is clearly observable that the artificial peak at the beginning of the surface weighted curve disappears, and the curve representing the contribution of each 1 *micron* size class to the cumulative surface of the entire droplet population becomes more even. The good agreement of average sauter mean diameter value to measurement could be retained (calculation result showed an average of 24.3 *micron*), and the relatively high proportion of smaller droplets aiming at providing a satisfactory extent of surface is also preserved as can be seen in case of the number weighted distribution curve.

7. **Conclusion**

A new approach implemented in a specialized commercial engine simulation code for predicting diesel spray formation was investigated and areas for improvement were identified. Bimodality of droplet size spectrum is by definition a consequence of the models used, but this is proved not to match reality according to measurements. Hence, a new approach is proposed to decrease bimodality of droplet size spectrum, while a sufficient number of relatively small droplets remaining in the vicinity of injector nozzle in agreement with reality.

Through introduction of a new child production mechanism the bimodality characteristic to the calculations using child production mechanisms could significantly be reduced. The analysis conducted drew attention to the fact that calculations

seemingly providing excellent agreement with detailed measurement data might also contain discrepancies related to reality in terms of size distribution. Through implementation of a homogenous distribution function for child production these discrepancies could be reduced considerably, and in the model a new tool is provided to further change the shape of size distribution according to measurement data concerning this quantity.

Acknowledgement. The authors would like to express their gratitude towards Dr. Sakata of CityTOYOTA Motor Corporation, Professor Senda of placePlaceNameDoshisha PlaceTypeUniversity and Dr. Nagaoka of TCRDL for providing the experimental data for this paper. This work has been supported by the Hungarian National Fund for Science and Research under contract No. OTKA T 037651.

References

1. AVL List GmbH: User manual of FIRE code version 8.4. (2005).
2. Blessing, M.: Untersuchung und Charakterisierung von Zerstäubung, Strahlausbreitung und Gemischbildung aktueller Dieseldirekteinspritzsysteme, Ph.D. Dissertation, Universität Stuttgart, (2004).
3. Faeth, G.M., Hsiang, L.P. and Wu, P.K.: Structure and break-up properties of sprays. *International Journal of Multiphase Flow*, **21**(1), (1995), 99-127.
4. Mayer, W.O.H.: Zur koaxialen Flüssigkeitszerstäubung im Hinblick auf die Treibstoffaufbereitung in Raketentriebwerken. Ph.D. Dissertation, DLR Institut für Chemische Antriebe und Verfahrenstechnik, Lampoldshausen, (1993).
5. Lefebvre, G.: Atomization and Sprays, Hemisphere Publishing Corporation, New York, (1989), ISBN 0-89116-603-3.
6. Reitz, R.D.: Modeling atomization processes in high-pressure vaporizing sprays. *Atomization and Spray Technology*, **3**, (1987), 309-337.
7. Schneider, B.M.: Experimentelle Untersuchung zur Spraystruktur in transparenten, verdampfenden und nicht verdampfenden Brennstoffstrahlen unter Hochdruck, Ph.D. Dissertation, Eidgenössische Technische Hochschule Zürich, (2003).
8. Reitz, R.D.: Atomization and other breakup regimes of a liquid jet, Ph.D. Thesis, Mechanical and Aerospace Department, Princeton University, Princeton, StateNJ, countryregionUSA, (1978).
9. Bayvel, L. and Orzechowski, Z.: Liquid atomization, Taylor & Francis, London, (1993), ISBN 0-89116-959-8.
10. Hohmann, S.: Strahlausbreitung und Tropfenverdunstung bei der dieselmotorischen Direkteinspritzung, Ph.D. Dissertation, Rheinisch-Westfälischen Technischen Hochschule Aachen, (1999).
11. Pilch, M. and Erdmann C.A.: Use of breakup time data and velocity history data to predict the maximum size of stable fragments. *International Journal of Multiphase Flow*, **13**(6), (1987), 741-757.
12. Smallwood, G.J. and Guilder, Ö.L.: View on the structure of transient diesel sprays. *Proceedings of Atomization and Sprays*, **10**, (2000), 355-386.
13. Hiroyasu, H. and Arai, M.: Structures of fuel sprays in diesel engines, SAE Technical Papers Series, (1990), 900475.

14. El-Hannouny, E.M. and Farrell, P.V.: Effect of injection parameters and injection system on spray characteristics for HSDI diesel engines, In Proceedings of ICLASS Conference, Sorrento, Italy, (2003).

15. Han, J.S., Lu, P.H., Xie, X.B., Lai, M.C. and Henein, N.A.: Investigation of diesel spray primary break-up and development of different nozzle geometries, SAE Technical Papers Series, (2002), 2002-01-2775.

16. Brodkey, R.S.: The phenomena of fluid motions, Addison-Wesley, Reading, MA, USA, (1967), ISBN 0-486-68605-1.

17. Yule, A.J. and Salters, D.G.: The breakup zone of a diesel spray: part 1, length of zone and volume of unatomized liquid. *Atomization and Sprays*, **5**, (1995), 157-174.

18. Faeth, G.M., and Hsiang, L.P.: Drop deformation and breakup due to shock-wave and steady disturbances. *International Journal of Multiphase Flow*, **21**(4), (1995), 545–560.

19. Hiroyasu, H. and Miao, H.: Measurement and calculation of diesel spray penetration, In Proceedings of ICLASS Conference, Sorrento, Italy, (2003).

20. Dukowicz, J.K.: A particle fluid model for liquid sprays. *Journal of Computational Physics*, **35**, (1980), 229-253.

21. O^Rourke, P.J. and Amsden, A.A.: The TAB method for numerical calculations of spray droplet breakup., SAE Technical Papers Series, (1987), 872089.

22. Ibrahim, E.A., Yang, H.Q. and Przekwas, A.J.: Modelling of spray droplets deformation and breakup. *Journal of Propulsion and Power*, **9**, (1993), 651-654.

23. Schmehl, R.: Advanced modeling of droplet deformation and breakup for CFD analysis of mixture preparation, In Proceedings of ILASS-Europe Conference, Zaragoza, Spain, (2002).

Journal of Computational and Applied Mechanics, Vol. 8., No. 1., (2007), pp. 85–100

ANALYSIS OF SPRAY EVOLUTION IN INTERNAL COMBUSTION ENGINES USING NUMERICAL SIMULATION

András Kadocsa, Reinhard Tatschl, Gergely Kristóf
Department of Fluid Mechanics Faculty of Mechanical Engineering, Budapest University of Technology and Economics
H-1111 Budapest, Bertalan L. u. 4-6, Hungary
kadocsa@ara.bme.hu

[Received: January 29, 2007]

Abstract. Numerical simulation is a widely used research tool in internal combustion related research. This paper summarizes results of research on a new approach of spray formation calculations. Using a primary breakup model for separately describing the initial liquid disintegration of injected liquid based on the flow properties stemming from a previous calculation of injector nozzle flow gives a better predicting capability and is able to suit the new needs of advanced combustion systems such as HCCI engines or various forms of split injection. The child breakup mechanism provides the necessary droplet surface for evaporation in the vicinity of nozzle, but it causes bimodality in the size spectrum, hence there is an unrealistic factor behind seemingly good agreement of calculation results and measurement data. The new homogenous distribution child production model proposed here is aimed at reducing this effect, and providing a more even size distribution while retaining good agreement with measurement data in other aspects of examination.

Keywords: Diesel injection, numerical simulation, primary breakup, child droplet size distribution

Nomenclature

C_i	[-]	breakup model constants
C_μ	[-]	standard $k-\varepsilon$ turbulence model constant ($C_\mu = 0.09$)
D	$[m]$	droplet diameter
SMD	$[m]$	Sauter Mean Diameter
$\mathrm{Re} = \dfrac{u\rho_l D}{\mu_l}$	[-]	Reynolds number
T	[-]	Taylor parameter
$We_g = \dfrac{u^2\rho_g D}{\sigma}$	[-]	Weber number defined with ambient gas density
$We_l = \dfrac{u^2\rho_l D}{\sigma}$	[-]	Weber number defined with injected liquid density
a	$[m]$	stable droplet radius
k	$[m^2/s^2]$	turbulent kinetic energy
r	$[m]$	actual droplet radius

r_c	$[m]$	child droplet radius
t	$[s]$	time
u	$[m/s]$	relative velocity
z	[-]	non-dimensional radius
ε	$[m^2/s^3]$	turbulent dissipation rate
τ	$[s]$	characteristic breakup time
Λ	$[m]$	wavelength of fastest growing surface wave
Ω	$[1/s]$	growth rate of fastest growing surface wave
μ_l	$[kg/ms]$	dynamic viscosity of injected liquid
ρ_g	$[kg/m^3]$	gas density at ambient pressure
ρ_l	$[kg/m^3]$	density of injected liquid
σ	$[N/m]$	characteristic breakup time

1. **Introduction**

Numerical simulation has played an important role in engine development for two decades. As the models applied developed, and the increase in computational performance created the opportunity to include larger domains and more detailed modeling approaches, it became an acknowledged research tool as well. Numerical simulation has played an important role in engine development for two decades. As the models applied developed, and the increase in computational performance created the opportunity to include larger domains and more detailed modeling approaches, it became an acknowledged research tool as well.

The accuracy of prediction of mixture formation is of great importance concerning the subsequent combustion processes, and thus it influences the ability of numerical simulation to predict e.g. pollutant emission. With the increased attention on environmental aspects of internal combustion engines, the simulation of spray formation gained on increased importance, and became an area of intensive development. The changing requirements represented by advanced injection systems – e.g. spilt injection or $HCCI$ engines – resulted in a need for rethinking the conception of spray formation simulation, and providing a new approach to fulfill these requirements.

Since measurement technology provides due to its limitation concerning time and length scales and because of its outstandingly high cost demand only a limited opportunity to investigate the very small time and length scales characteristic to direct fuel injection, numerical simulation plays an important role in engine related research as well.

The new approach of using a separate primary breakup model to better simulate the initial phase of liquid breakup represents an answer to the newly arising needs of internal combustion engine research and development. The new model used throughout the simulations of this paper is implemented in a specialized commercial CFD code [1], and is used for diesel engine injection simulations. The calculations presented here and the new method for predicting child droplet production were realized in the framework of a research project aiming at gaining experience about the combination

and interaction of models, to identify areas for improvement and to propose or realize new ideas aiming at better prediction capability.

2. **Breakup of fluids**

Fluid columns break up into ligaments or droplets, and these latter break up into further droplets according to different, simultaneously acting mechanisms, depending on a number of physical characteristics. The first process is generally referred to as *primary breakup* and the latter process is called *secondary breakup* [2, 3, 4]. Based on their characteristic physical processes, these basic breakup regimes can be differentiated, and they are treated in literature usually separately.

In both basic breakup regimes a number of different breakup types appear. These breakup types can be characterized by various properties of spray. The most important quantity summarizing the influential factors concerning the intensity and type of breakup is the Weber number, calculated with droplet (or nozzle orifice) diameter, and either with ambient gas or injected liquid density, and is referred to as We_g and We_l respectively. The type of Weber number to be used depends on the aim of investigation, but both dimensionless parameters describe the same phenomenon, only from another perspective.

Another important quantity is the Reynolds number, defined in spray literature in general [5, 6] with density and viscosity values referring to injected liquid.

The third important quantity representing the effect of viscosity and surface tension in the context of spray breakup is the Ohnesorge number as defined in equation (1)

$$Oh = \frac{\sqrt{We_l}}{\mathrm{Re}} = \frac{\mu_l}{\sqrt{\sigma D \rho_l}} \tag{1}$$

Based on these quantities, there are a number of classification methods for describing the regimes of initial liquid disintegration, i.e. primary breakup. A classification is given by Schneider [7] based on the works of Lefebvre [5] and Reitz [8], as depicted in Fig. 1.

In general it can be stated that the higher the Weber number, the more intensive the breakup is, thus ranging from Rayleigh type of breakup (*Zone A*) through first (*Zone B*) and second (*Zone C*) wind-induced breakup to atomization (*Zone D*). In case of our investigations the general Weber number far exceeds the highest limit of regime switch, therefore the breakup process is characterized by properties of the regime "atomization" [9].

The subsequent breakup of ligaments and droplets, i.e. secondary breakup can also be classified according to Weber number, as depicted in Fig. 2. It ranges from bag breakup through bag and stamen type of breakup to boundary layer stripping and catastrophic breakup, with increasing Weber number. For diesel conditions boundary layer stripping, capillary wave detachment (Kelvin-Helmholtz instability) and catastrophic breakup by Rayleigh-Taylor waves are typical [10].

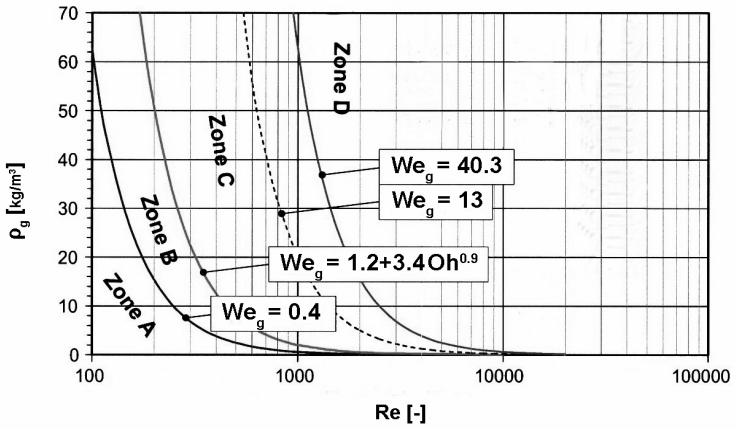

Figure 1. Primary breakup zones as a function of Reynolds number and ambient gas density [7]

The most important factor influencing primary breakup – as agreed by most of recent literature – is the character of the fluid flow leaving the injector orifice [12, 13], being injection pressure [14], L/D ration [13] and shape of injection nozzle bore [15] the most decisive aspects. Secondary breakup is most influenced by properties of injected liquid – mostly viscosity [16, 17] – and by ration of liquid and gas density [18, 19].

3. **Modeling spray formation**

To appropriately model spray formation, a number of physical processes must be taken into consideration. For most of these processes a separate sub-model accounts for. Besides breakup such processes are evaporation, droplet drag and collision and coalescence of droplets [1]. All these processes are covered in the calculations presented here by separate, generally accepted models, however the emphasis of this research is put on primary and secondary breakup, therefore other mechanisms are not discussed here in detail.

Modeling of liquid breakup has been developed significantly in the past two decades, however most of these models adapted the approaches generally used in simulations. A good example on this is that droplets are generally tracked in a Lagrangian way in a gas flow field, which latter is treated by conservation equations for mass, momentum and energy as well as turbulence in an Eulerian frame of reference.

Another general framework is represented by the *Discrete Droplet Model* (DDM) [20]. Since the typical number of droplets arising during a high pressure diesel injection is in the order of magnitude of 10^6-10^8, the registration and tracking of each and every individual droplet is not practical and not even necessary. Therefore, in the DDM

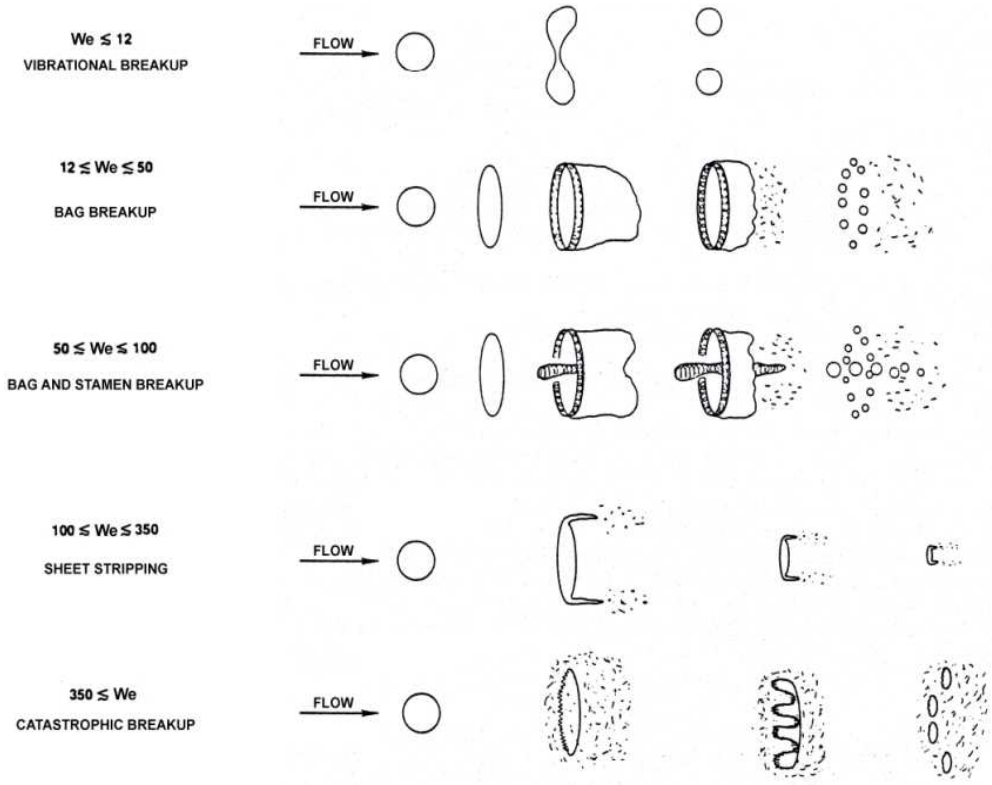

Figure 2. Secondary breakup zones as a functionof Weber number [11]

approach the droplets are collected into parcels, and they have uniform properties (diameter, velocity, temperature etc.) within one parcel. A parcel behaves like one drop with the additional information on the number of identical droplets represented. Hence, the calculation is not necessary to be performed for every single droplet, however, the diversity of droplets is still well represented by choosing an appropriate number of parcels (typically in the order of 10^4).

The calculation of the parcel movement is done with a subcycling procedure between the gas phase time steps taking into account the forces exerted on droplets in the parcels by the gas phase as well as the related heat and mass transfer. In an analogous way the gas phase receives the forces resulted from spray movement as source terms in the next gas time step.

A further approach that is used by most of the prevalent models is the *rate approach* [6]. As it is described by equation (2), it grabs the phenomenon of breakup through

the velocity of loss of droplet radius, providing a widely used approach of breakup.

$$\frac{dr}{dt} = -\frac{r-a}{\tau} \tag{2}$$

The submodels for breakup used in most of CFD codes all aim at determining the value of stable radius a and characteristic breakup time τ determining the breakup rate, and they mostly use all the above mentioned approaches as framework for operation. The advancement is thus usually achieved through creating new models for determining the stable radius a and characteristic breakup time τ.

One of the earliest attempts for this was the *Taylor Analogy Breakup* (TAB) model [21], which is based on the analogy between an oscillating and distorting droplet and a spring-mass system. The external force is represented by the aerodynamic forces acting on the droplet, the spring force is related to the surface tension, and the damping force corresponds to the force due to liquid viscosity. Hence, as a reaction on the aerodynamic forces, the droplet starts to oscillate. As soon as the amplitude of this oscillation reached a predefined level, the droplet disintegrates, i.e. breakup occurs.

A similar idea, based also on the elliptic deformation of the droplet is reflected in the *Dynamic Droplet Breakup* (DDB) model, which tracks the motion of the mass centers of the half droplets [22]. It is essentially a nonlinear formulation of the TAB model equations, and the time consuming numerical integration seems not to have been offset by the increase in accuracy, since the model has not found wide acceptance [23].

The most commonly used single secondary breakup model was developed by Reitz [6] and is called $Wave$. This model is used for simulation of secondary breakup in calculations of this paper, therefore its working principles are described here in more detail.

This model relates breakup to the Kelvin-Helmholtz instability, as depicted in Figure 3.

The growth of an initial perturbation of a liquid surface is linked to liquid Reynolds number as well as gas Weber number and other physical and dynamic parameters (e.g. viscosity) of the injected fuel and the domain fluid. The stable radius is linked to the wavelength of the fastest growing surface wave according to equation (3) [6].

$$a = C_1 \Lambda \tag{3}$$

where Λ represents the wavelength of fastest growing surface wave, and is defined in equation (4).

$$\Lambda = 9.02r\frac{(1+0.45Oh^{0.5})(1+0.4T^{0.7})}{(1+0.87We_g^{1.67})^{0.6}} \tag{4}$$

whereas

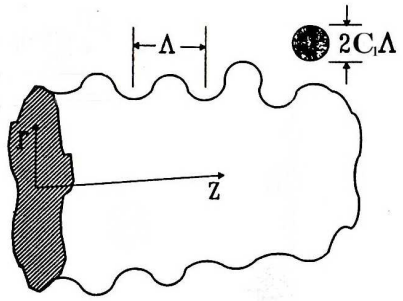

Figure 3. The Wave model relates breakup to Kelvin-Helmholtz instability and product droplet size is proportional to surface wave length [6]

$$T = Oh\sqrt{We_g} \tag{5}$$

The breakup time is calculated with a number of factors as defined in equation (6)

$$\tau = C_2 \frac{3.726r}{\Lambda\Omega} \tag{6}$$

where Ω represents the growth rate of fastest growing surface wave, and is defined in equation (7),

$$\Omega = \left(\frac{\rho_l r^3}{\sigma}\right)^{-0.5} \frac{0.34 + 0.38We_g^{1.5}}{(1+Oh)\,(1+1.4T^{0.6})} \tag{7}$$

and C_1 and C_2 are model constants.

When exposed to certain conditions (e.g. high relative ambient gas velocities), and the actual radius is larger than the stable radius under the circumstances considered, the droplets of a parcel start "losing" diameter as prescribed by equation (2). In basic case, the mass shed from these droplets in each subcycle is used to update the diameter of drops. This is done by calculating the new drop diameter from the rate of equation (2) according to the local conditions for stable diameter a and breakup time τ. Based on the updated radius the total mass is converted into an increased number of droplets of identical diameter (within the same parcel). Hence, the mass in a parcel is always conserved (not considering evaporation, or child droplet production as described later), only the number of droplets contained is changing according to droplet diameter.

Since the droplets lose diameter always only in proportion to the time passed since the last spray time step, the model does not deliver enough small droplets near the nozzle. Therefore, a so called child production mechanism was inserted into Wave [6].

The basic idea of child production mechanism is that a certain proportion of the shed mass immediately receives the stable diameter, i.e. they do not "approach" it incrementally according to the rate approach of equation (2). Since the basic idea of the *DDM* method is that a parcel contains droplets of identical properties, the droplets created in the framework of the child droplet mechanism, referred to as child droplets, are placed in a newly created parcel. The diameter of these child droplets is in most cases much lower than the value reached by the parent droplets (the droplets from which the child droplets were created) in the same timeframe, which provides the necessary additional droplet surface for evaporation already in the vicinity of the injection nozzle.

The above mentioned models have been used – and are still widely used – to predict the entire spray breakup process. However, a disadvantage of all these models if used alone is that certain initial properties of the spray have to be provided by the user, or have to be assumed by the model based on practical or theoretical considerations. Such initial circumstances include the spray angle and droplet diameter at the nozzle orifice and the transition from a continuum liquid column to droplets that can subsequently be handled by secondary breakup models discussed above.

The use of an appropriate separate primary breakup model enables the prediction of these initial quantities. The basic prerequisite necessary for this is to have information about the injector flow properties, which are regarded to play a key role in early spray properties, such as spray angle. *Diesel Breakup model*, the primary breakup model used throughout this research uses a so called *nozzle file* for this purpose [1].

The nozzle file is created in advance in a separate, 3 dimensional, time dependent multi-phase simulation of the flow in the injector nozzle, so at the beginning of the spray calculation all relevant data on the nozzle flow is available time and spatially resolved into the nozzle file. The subsequent, separate spray calculation uses this data source as an input for the breakup mechanism. Hence, all droplets initialized by the primary breakup model consider the properties of injected liquid, as calculated in the previous simulation. The use of an independent simulation and a separate nozzle file enables e.g. various combustion chamber geometries to be simulated using the same nozzle file without the need for repeating the injector nozzle calculation for each case.

According to this approach the injected liquid is already tracked in the injector nozzle (this information is contained in the nozzle file). After leaving the injector nozzle it is treated by the primary breakup model, and after reaching certain predefined conditions (e.g. a predefined Weber number) the droplets are handed over to the secondary breakup model. All these droplets are treated by the secondary breakup model, until a final stable diameter is reached, and no more breakups occur.

In the vicinity of the nozzle – where primary breakup occurs and hence the primary breakup model should be used – two different mechanisms result in breakup. One of them is a consequence of turbulence of the flow of liquid, while the other one is related to the aerodynamic forces acting on the droplet, as in case of secondary breakup. There is no general agreement in literature which of these mechanisms dominates primary breakup, and it also depends on the topical circumstances of spray formation

considered. Therefore, a basic idea of Diesel Breakup model is to let these mechanisms compete in case of every breakup. Hence, for each parcel equation (2) is calculated by means of both mechanisms, and the mechanism giving a higher breakup rate will govern breakup.

The aerodynamic mechanism is accounted for by the $Wave$ model, just as in case of secondary breakup throughout this research. Turbulent breakup is calculated from turbulence values of injected liquid (contained in the nozzle file), according to equations (8) and (9).

$$a = C_3 C_\mu^{0.75} \frac{k^{1.5}}{\varepsilon} \tag{8}$$

$$\tau = C_4 C_\mu \frac{k}{\varepsilon} \tag{9}$$

4. **Background of calculation**

The investigations reported have been accomplished using the $FIRE$ software ($v8.3-8.4$), a CFD code developed by AVL List[1], specialized on internal combustion engine related numerical simulation [1]. The parameters of the spray formation process to be simulated were chosen based on the data available for validation. The measurement data used throughout this research were received from Toyota Central Research and Development Laboratories and Doshisha Universtiy, and they were widely used in the wider context of the works presented here. The basic settings of all calculations are as displayed in Table 1.

Table 2. Characteristics of calculation

Injection time	$2ms$
Total simulated time	$8ms$
Length of time step	$0.01ms$
Maximum number of iterations per time step	100
Nozzle bore diameter	$0.14mm$
Nozzle bore length	$0.8mm$
Injected liquid	$Hexadecane$
Injection pressure	$87.5MPa$
Total volume injected	$1.01316e-8m^3$
Ambient gas	CO_2
Ambient gas pressure	$2.1e+6Pa$
Ambient gas temperature	$293K$

The computational domain models a simple, box shaped environment, but the general order of magnitude of cell sizes takes into consideration the usual characteristics

[1] AVL List is world's largest privately owned engine developer, located in Graz, Austria.

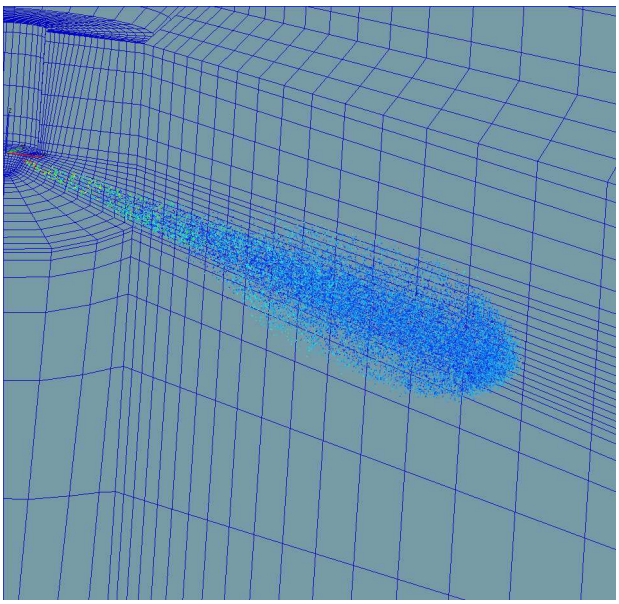

Figure 4. The cell structure in the vertical cut through the injection axis

of numerical grids for the purpose of internal combustion engine calculations. However, the structure of grid considers the expected pattern of flow field, determined mainly by the evolving spray cone. The injector nozzle is placed symmetrically in the middle of the box modeled.

The numerical model consists entirely of hexahedron cells, and it has total dimensions of $0.4 \times 0.2 \times 0.12m$. The structure is considerably compressed towards the injector orifice, and has long cells further away from the nozzle. These cells are, however, directed in the expected main flow direction, as depicted in Figure 4. (The spray displayed along with the cut through view of the grid represents a status of $2ms$ after start of injection, and the color data corresponds to the diameter of droplets, while the size of displayed droplets is chosen to be constant for better visibility.) The total number of cells is $45,144$.

There is a wall type boundary condition on all boundaries of the model applied, with a prescribed temperature of $300K$, however, the droplets are not expected to reach any of these boundaries in the time window of the calculation.

5. **The new model applied**

The aim of the child mechanism introduced by Reitz [6] for the *Wave* model was to provide sufficiently small droplets in the vicinity of injector nozzle to meet evaporation behavior characteristic to real life spray processes. An average of these child

droplets and the significantly larger parent droplets can deliver a reasonable agreement with measured SMD values. However, this procedure delivers by nature a markedly bimodal spectrum in droplet size distribution.

Since Diesel Breakup model is responsible for breakup of liquid in the vicinity of nozzle, it also includes child production mechanism. In case of this model, an attempt has already been made to reduce the shortcoming of the child production procedure used in secondary breakup. A Chi-square distribution of probable child droplet sizes was assumed, and a random number is used on the ordinate of the cumulative distribution diagram to get the appropriate diameter of child droplets via the inverse function on the diameter coordinate axis. However, the size distribution still tends to show bimodality.

A main aim of the current research is to develop an altered approach for child production both in secondary and primary breakup to reduce bimodality of size distribution. Calculations have been performed to optimize model parameters based on measurement data. As a result of these investigations good agreement in spray penetration and average SMD value could be obtained. However, size distributions of these calculations were characterized by significant bimodality. Since the available measurement data showed that bimodality of droplet size spectrum is fully absent, effort has been made to decrease this undesired effect of child droplet production mechanism.

To reduce bimodality, a linear distribution of child droplet sizes is assumed between the lower limit of stable droplet radius a respectively the upper limit taken as parent droplet radius r of the considered parcel. This approach assumes a constant value of the probability density function for the child droplet size between the lower and an upper limiting value. For the mathematical formulation a non-dimensional radius z is introduced, as displayed in equation (10).

$$z = \frac{r_c}{a} \tag{10}$$

According to earlier investigations, child production mechanism plays a more pronounced role in case of primary breakup, therefore the new idea for child production was first implemented in Diesel Breakup model. To avoid confusing effects, child production for secondary breakup was switched off in all calculations.

The cumulative probability density function using this value is defined in equation (11).

$$F(z) = \begin{cases} 0 & for \;\; z \leq 1 \\ \dfrac{a\,(z-1)}{(r-a)} & for \;\; 1 < z < \dfrac{r}{a} \\ 1 & for \;\; \dfrac{r}{a} \leq z \end{cases} \tag{11}$$

The implementation in the $FIRE$ code uses a random number chosen on the ordinate of the cumulative distribution diagram to get the appropriate diameter via the

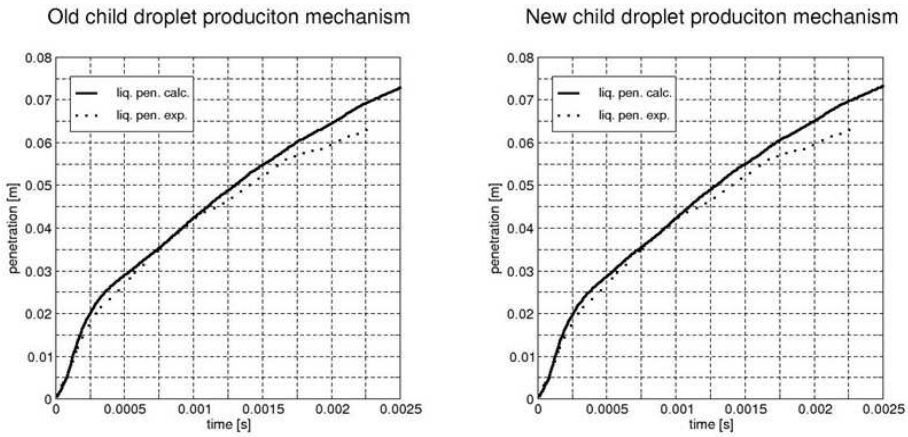

Figure 5. Penetration curves without and with use of the new primary breakup child production mechanism

inverse function on the non-dimensional diameter coordinate axis. This value is assigned to the child parcel under consideration. The use of random numbers provides a representation of the entire size distribution applied.

6. **Results**

A pair of sample calculations is presented here to introduce the effect of the new child production mechanism implemented. In these calculations the proportion of mass put into child parcels from the entire shed mass and the frequency of child parcel introduction was set high, in order to see the effects of the model change more pronounced. Due to the same considerations the C_4 program parameter belonging to the characteristic breakup time τ of Diesel Breakup model was set high to cause slow parent droplet breakup, and hence set stable diameter to a low value (if parent breakup is slow parent drops retain their size and hence their speed in a greater extent).

In one of the calculations the standard (Chi-square type of) child production mechanism, in the other calculation the new child production mechanism was used.

The penetration curves were barely affected by this change, and both gave a good agreement with measurement data, as depicted in Figure 5.

The changes were expected to be perceived in case of size distributions. This property is very rarely investigated in similar simulations, therefore comparison with literature data is not possible, however results are good interpretable without comparison as well.

For visualization of this a set of three curves was introduced. The first curve is the number weighted distribution, which is the covering curve of the bars representing the

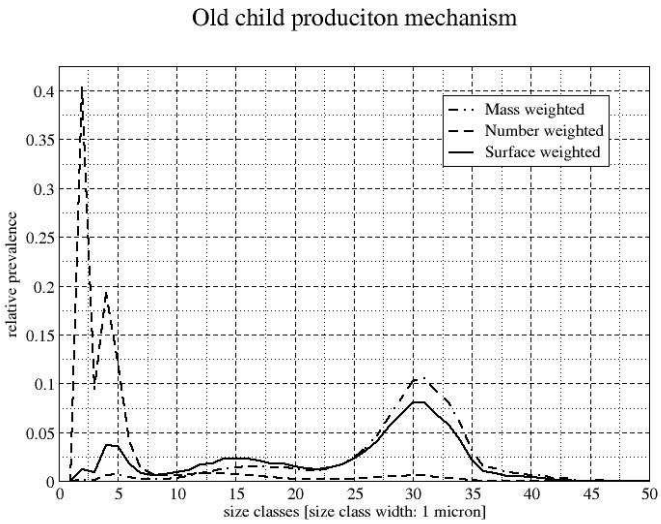

Figure 6. Size distributions with use of the conventional child production mechanism

relative prevalence of size classes, each 1 *micron* wide (e.g. representing the proportion of droplets with diameter between 3 and 4 *microns* related to the entire droplet population). The second curve is the surface area weighted distribution. It covers the bars representing the contribution of each of these 1 *micron* size classes to the cumulative surface of the entire droplet population. The third curve (mass weighted distribution) covers the bars representing the contribution of these size classes to the cumulative mass of the entire droplet population.

The most important indicator with respect to mixture formation is the surface weighted size distribution, since this is in closest relation to the expected evaporation behavior. On the other hand, bimodality appears on this curve most pronounced, since a large number of small droplets can "elevate" the left part of the curve. The size distribution without using the new child production model looks as depicted in Figure 6.

A pronounced bimodality is observable in this case with two peaks of surface weighted size distributions at $4-5$ *micron* and 30 *micron* respectively. It means that although the targeted average sauter mean diameter of 23.2 *micron* of measurements is reached in good agreement (calculation results showed 23.9 *micron*), this is obtained through an artificial duality of a large number of very small droplets, and a group of droplets representing large mass with higher than the target diameter.

If the new child production model is switched on, the size distribution changes significantly, as depicted in Figure 7.

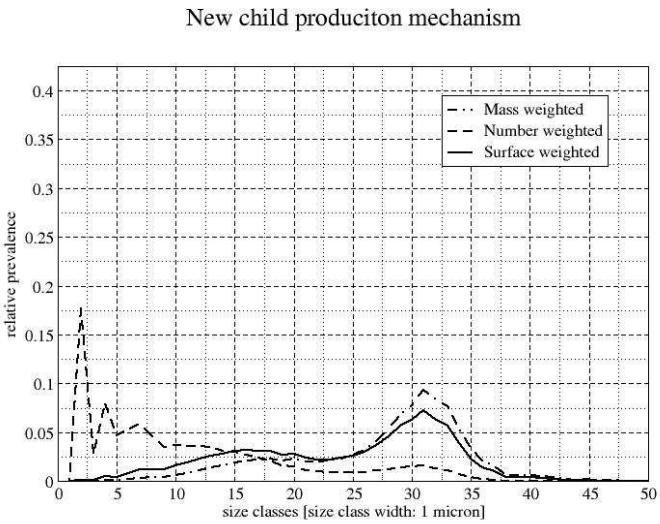

Figure 7. Size distributions with use of the new primary breakup child production mechanism

It is clearly observable that the artificial peak at the beginning of the surface weighted curve disappears, and the curve representing the contribution of each 1 *micron* size class to the cumulative surface of the entire droplet population becomes more even. The good agreement of average sauter mean diameter value to measurement could be retained (calculation result showed an average of 24.3 *micron*), and the relatively high proportion of smaller droplets aiming at providing a satisfactory extent of surface is also preserved as can be seen in case of the number weighted distribution curve.

7. **Conclusion**

A new approach implemented in a specialized commercial engine simulation code for predicting diesel spray formation was investigated and areas for improvement were identified. Bimodality of droplet size spectrum is by definition a consequence of the models used, but this is proved not to match reality according to measurements. Hence, a new approach is proposed to decrease bimodality of droplet size spectrum, while a sufficient number of relatively small droplets remaining in the vicinity of injector nozzle in agreement with reality.

Through introduction of a new child production mechanism the bimodality characteristic to the calculations using child production mechanisms could significantly be reduced. The analysis conducted drew attention to the fact that calculations

seemingly providing excellent agreement with detailed measurement data might also contain discrepancies related to reality in terms of size distribution. Through implementation of a homogenous distribution function for child production these discrepancies could be reduced considerably, and in the model a new tool is provided to further change the shape of size distribution according to measurement data concerning this quantity.

Acknowledgement. The authors would like to express their gratitude towards Dr. Sakata of CityTOYOTA Motor Corporation, Professor Senda of placePlaceNameDoshisha PlaceTypeUniversity and Dr. Nagaoka of TCRDL for providing the experimental data for this paper. This work has been supported by the Hungarian National Fund for Science and Research under contract No. OTKA T 037651.

References

1. AVL List GmbH: User manual of FIRE code version 8.4. (2005).
2. Blessing, M.: Untersuchung und Charakterisierung von Zerstäubung, Strahlausbreitung und Gemischbildung aktueller Dieseldirekteinspritzsysteme, Ph.D. Dissertation, Universität Stuttgart, (2004).
3. Faeth, G.M., Hsiang, L.P. and Wu, P.K.: Structure and break-up properties of sprays. *International Journal of Multiphase Flow*, **21**(1), (1995), 99-127.
4. Mayer, W.O.H.: Zur koaxialen Flüssigkeitszerstäubung im Hinblick auf die Treibstoffaufbereitung in Raketentriebwerken. Ph.D. Dissertation, DLR Institut für Chemische Antriebe und Verfahrenstechnik, Lampoldshausen, (1993).
5. Lefebvre, G.: Atomization and Sprays, Hemisphere Publishing Corporation, New York, (1989), ISBN 0-89116-603-3.
6. Reitz, R.D.: Modeling atomization processes in high-pressure vaporizing sprays. *Atomization and Spray Technology*, **3**, (1987), 309-337.
7. Schneider, B.M.: Experimentelle Untersuchung zur Spraystruktur in transparenten, verdampfenden und nicht verdampfenden Brennstoffstrahlen unter Hochdruck, Ph.D. Dissertation, Eidgenössische Technische Hochschule Zürich, (2003).
8. Reitz, R.D.: Atomization and other breakup regimes of a liquid jet, Ph.D. Thesis, Mechanical and Aerospace Department, Princeton University, Princeton, StateNJ, countryregionUSA, (1978).
9. Bayvel, L. and Orzechowski, Z.: Liquid atomization, Taylor & Francis, London, (1993), ISBN 0-89116-959-8.
10. Hohmann, S.: Strahlausbreitung und Tropfenverdunstung bei der dieselmotorischen Direkteinspritzung, Ph.D. Dissertation, Rheinisch-Westfälischen Technischen Hochschule Aachen, (1999).
11. Pilch, M. and Erdmann C.A.: Use of breakup time data and velocity history data to predict the maximum size of stable fragments. *International Journal of Multiphase Flow*, **13**(6), (1987), 741-757.
12. Smallwood, G.J. and Guilder, Ö.L.: View on the structure of transient diesel sprays. *Proceedings of Atomization and Sprays*, **10**, (2000), 355-386.
13. Hiroyasu, H. and Arai, M.: Structures of fuel sprays in diesel engines, SAE Technical Papers Series, (1990), 900475.

14. El-Hannouny, E.M. and Farrell, P.V.: Effect of injection parameters and injection system on spray characteristics for HSDI diesel engines, In Proceedings of ICLASS Conference, Sorrento, Italy, (2003).

15. Han, J.S., Lu, P.H., Xie, X.B., Lai, M.C. and Henein, N.A.: Investigation of diesel spray primary break-up and development of different nozzle geometries, SAE Technical Papers Series, (2002), 2002-01-2775.

16. Brodkey, R.S.: The phenomena of fluid motions, Addison-Wesley, Reading, MA, USA, (1967), ISBN 0-486-68605-1.

17. Yule, A.J. and Salters, D.G.: The breakup zone of a diesel spray: part 1, length of zone and volume of unatomized liquid. *Atomization and Sprays*, **5**, (1995), 157-174.

18. Faeth, G.M., and Hsiang, L.P.: Drop deformation and breakup due to shock-wave and steady disturbances. *International Journal of Multiphase Flow*, **21**(4), (1995), 545–560.

19. Hiroyasu, H. and Miao, H.: Measurement and calculation of diesel spray penetration, In Proceedings of ICLASS Conference, Sorrento, Italy, (2003).

20. Dukowicz, J.K.: A particle fluid model for liquid sprays. *Journal of Computational Physics*, **35**, (1980), 229-253.

21. O^Rourke, P.J. and Amsden, A.A.: The TAB method for numerical calculations of spray droplet breakup., SAE Technical Papers Series, (1987), 872089.

22. Ibrahim, E.A., Yang, H.Q. and Przekwas, A.J.: Modelling of spray droplets deformation and breakup. *Journal of Propulsion and Power*, **9**, (1993), 651-654.

23. Schmehl, R.: Advanced modeling of droplet deformation and breakup for CFD analysis of mixture preparation, In Proceedings of ILASS-Europe Conference, Zaragoza, Spain, (2002).

Notes for Contributors

to the Journal of Computational and Applied Mechanics

Aims and scope. The aim of the journal is to publish research papers on theoretical and applied mechanics. Special emphasis is given to articles on computational mechanics, continuum mechanics (mechanics of solid bodies, fluid mechanics, heat and mass transfer) and dynamics. Review papers on a research field and materials effective for teaching can also be accepted and are published as review papers or classroom notes. Papers devoted to mathematical problems relevant to mechanics will also be considered.

Frequency of the journal. Two issues a year (approximately 80 pages per issue).

Submission of Manuscripts. Submission of a manuscript implies that the paper has not been published, nor is being considered for publication elsewhere. Papers should be written in standard grammatical English. Two copies of the manuscript should be submitted on pages of A4 size. The text is to be 130 mm wide and 190 mm long and the main text should be typeset in 10pt CMR fonts. Though the length of a paper is not prescribed, authors are encouraged to write concisely. However, short communications or discussions on papers published in the journal must not be longer than 2 pages. Each manuscript should be provided with an English Abstract of about 50–70 words, reporting concisely on the objective and results of the paper. The Abstract is followed by the Mathematical Subject Classification – in case the author (or authors) give the classification codes – then the keywords (no more than five). References should be grouped at the end of the paper in numerical order of appearance. Author's name(s) and initials, paper titles, journal name, volume, issue, year and page numbers should be given for all journals referenced.

The journal prefers the submission of manuscripts in LaTeX. Authors should prefer the $\mathcal{AMS}$-LaTeX article class and are not recommended to define their own LaTeX commands. Visit our home page for further details concerning the issue how to edit your paper.

For the purpose of refereeing, two copies of the manuscripts should initially be submitted in hardcopy to an editor of the journal. The eventual supply of an accepted-for-publication paper in its final camera-ready form (together with the corresponding files on an MS–DOS diskette) will ensure more rapid publication. Format requirements are provided by the home page of the journal from which sample LaTeX files can be downloaded:

`http://www.uni-miskolc.hu/home/web/pumns/mechanics`

These sample files can also be obtained directly (via e-mail) from a member of the Editorial Board, Gy. Szeidl (Gyorgy.SZEIDL@uni–miskolc.hu), upon request.

Twenty offprints of each paper will be provided free of charge and mailed to the correspondent author.

The Journal of Computational and Applied Mechanics is abstracted in Zentralblatt für Mathematik and in the Russian Referativnij Zhurnal.

Responsible for publication: Rector of the Miskolc University
Published by the Miskolc University Press under the leadership of Dr. József PÉTER
Responsible for duplication: works manager Mária KOVÁCS
Number of copies printed: 200
Put to the Press on April 12, 2008
Number of permission: TU 2008-???-ME **HU ISSN 1586–2070**

A Short History of the Publications of the University of Miskolc

The University of Miskolc (Hungary) is an important center of research in Central Europe. Its parent university was founded by the Empress Maria Teresia in Selmecbánya (today Banska Štiavnica, Slovakia) in 1735. After the first World War the legal predecessor of the University of Miskolc moved to Sopron (Hungary) where, in 1929, it started the series of university publications with the title *Publications of the Mining and Metallurgical Division of the Hungarian Academy of Mining and Forestry Engineering* (Volumes I.-VI.). From 1934 to 1947 the Institution had the name Faculty of Mining, Metallurgical and Forestry Engineering of the József Nádor University of Technology and Economic Sciences at Sopron. Accordingly, the publications were given the title *Publications of the Mining and Metallurgical Engineering Division* (Volumes VII.-XVI.). For the last volume before 1950 – due to a further change in the name of the Institution – *Technical University, Faculties of Mining, Metallurgical and Forestry Engineering, Publications of the Mining and Metallurgical Divisions* was the title.

For some years after 1950 the Publications were temporarily suspended.

After the foundation of the Mechanical Engineering Faculty in Miskolc in 1949 and the movement of the Sopron Mining and Metallurgical Faculties to Miskolc, the Publications restarted with the general title *Publications of the Technical University of Heavy Industry* in 1955. Four new series - Series A (Mining), Series B (Metallurgy), Series C (Machinery) and Series D (Natural Sciences) - were founded in 1976. These came out both in foreign languages (English, German and Russian) and in Hungarian.

In 1990, right after the foundation of some new faculties, the university was renamed to University of Miskolc. At the same time the structure of the Publications was reorganized so that it could follow the faculty structure. Accordingly three new series were established: Series E (Legal Sciences), Series F (Economic Sciences) and Series G (Humanities and Social Sciences). The latest series, i.e., the series H (European Integration Studies) was founded in 2001. The eight series are formed by some periodicals and such publications which come out with various frequencies.

Papers on computational and applied mechanics were published in the

Publications of the University of Miskolc, Series D, Natural Sciences.

This series was given the name Natural Sciences, Mathematics in 1995. The name change reflects the fact that most of the papers published in the journal are of mathematical nature though papers on mechanics also come out.

The series

Publications of the University of Miskolc, Series C, Fundamental Engineering Sciences

founded in 1995 also published papers on mechanical issues. The present journal, which is published with the support of the Faculty of Mechanical Engineering as a member of the Series C (Machinery), is the legal successor of the above journal.

Journal of Computational and Applied Mechanics

Volume 8, Number 1 (2007)

Contents

Contributed Papers

László BARANYI and János VAD: Preface 3–4

Said ABBOUDI, Jing DENG, Michel IMBERT: Thermal wall influence on the behavior of axisymmetric laminar compressible flow in nozzle 5–19

Alessandro CORSINI and Anthony G. SHEARD: A reciprocal theorem for steady-state heat conduction problems 21–37

Eric DIDIER, António R. J. BORGES: Numerical predictions of low Reynolds number flow over an oscillating circular cylinder flow past an oscillating cylinder 39–55

Csaba HŐS, László KULLMANN: A numerical study on the free-surface channel flow over a bottom obstacle 57–70

Huixia JIA, Konrad VOGELER, Lutz MÜLLER, Ronald MAILACH: Numerical investigation of rotor-stator interactions in a 1.5-stage low-speed axial compressor 71–83

András Kadocsa, Reinhard Tatschl and Gergely Kristóf: Analysis of spray evolution in internal combustion engines using numerical simulation 85–100

Stavros J. KARABELAS, Nikolaos-Christos G. MARKATOS: Mathematical modeling of subsonic two-phase condensation flow around an aircraft under various flight conditions 101-116